

TECHNISCHE UNIVERSITÄT MÜNCHEN  
TUM School of Engineering and Design

# Modelling Strategies for Acoustic Metamaterials with Porous Components and Numerical Studies on Exemplary Structures

Franziska Weber M.Sc.

Vollständiger Abdruck der von der TUM School of Engineering and Design der Technischen Universität München zur Erlangung des akademischen Grades einer

Doktorin der Ingenieurwissenschaften (Dr.-Ing.)

genehmigten Dissertation.

Vorsitz: Prof. Dr.-Ing. Fabian Duddeck

Prüfer der Dissertation:

1. Prof. Dr.-Ing. Gerhard Müller
2. Assoc. Prof. Romain Rumpler, Ph.D.

Die Dissertation wurde am 30.01.2023 bei der Technischen Universität München eingereicht und durch die TUM School of Engineering and Design am 18.07.2023 angenommen.





# Abstract

This thesis explains how vibroacoustic systems made out of a combination of acoustic cavities, linear elastic solids and porous absorbers along with the relevant boundary and coupling conditions can be mapped using the Finite Element Method (FEM). This includes acoustic metamaterials, which are characterized as structures that exhibit physical behaviour not observed in natural structures. Details are given on how to account for porous absorbers in the model. Different formulations of the so-called Johnson–Champoux–Allard model (JCAM) are presented and compared on exemplary systems. In addition to the existing formulations, a simplified version of the JCAM is introduced, which provides sufficiently accurate results for many applications, but generates significantly less computational effort than a full model. Building on a FEM model of one repetitive segment, this thesis describes how the wave propagation along a periodic structure and the sound transmission through a periodic structure can be computed using the Wave Finite Element Method (WFEM). Thereby the structures' periodicity is introduced by periodic boundary conditions. Besides the description of existing strategies, a novel approach to compute the sound transmission through and absorption of periodic structures with elastic frame porous boundary layers modelled by the JCAM is introduced. Compared to approaches in the literature, the proposed methodology simultaneously fulfils the following criteria: the elastic deformations of the pore framework are taken into account, the system can not only be excited by normal incident but also by inclined plane waves, the reflected part of the exciting wave is imaged and complex inclusion geometries within the porous layer can be taken into account. Using the modelling approaches presented, this thesis investigates the impact of inclusions and secondary vibrational systems on the dispersion characteristics of periodic metamaterials.

**Keywords:**

Finite Element Method, Johnson–Champoux–Allard model, Metamaterials, Porous media, Periodic structures, Sound transmission and absorption, Wave Finite Element Method, Wave propagation

# Acknowledgments

First of all, I would like to thank Prof. Müller for the opportunity to work on this thesis at his chair. In addition to the excellent professional support for my work, I always appreciated the pleasant interaction. I also want to express my appreciation to Romain for acting as second examiner for this thesis. Moreover I want to thank him for the inspiring exchange and the opportunity to visit him for a research stay in Stockholm. The time at KTH was very valuable for me. On the one hand because of the professional input, but also because of the personal impressions and experiences. I also thank Prof. Duddeck for chairing the audit committee.

My thanks go to all my colleagues at the chair of structural mechanics for the great working atmosphere and the pleasant time together. In particular, I would like to mention my long-time office mates Quirin and Matthias. The many technical discussions in our office have contributed significantly to this work. In addition, we quickly discovered that, besides our research topics, we are among other things united by our enjoyment of bad music and our passion for Schafkopf. I would also like to mention Felix, who made our quartet complete. I hope that the contact between us will continue in the future and that we will remain such good friends for a long time, preferably forever. Furthermore I thank Francesca for being my mentor for this work. Thank you for always having an open ear in all life situations, in addition to professional advice. I also liked going through probably the biggest change in my life at the same time as you did and enjoy that we can now get together with our sons to play.

I am very grateful to my family in the Allgäu for always being there for me during my studies and my doctorate. Thanks that you are always behind me, even if you, and also I, are not always completely clear about the content, meaning and benefit of this work. My biggest thanks go to my two boys. Dear Jojo, I am so glad to have you by my side. Without your motivation I would probably never have completed this work. Thank you for giving me the push and the space to continue working on my research. Dear Jakob, I am sorry that as a result of this work I have not had as much time for you as you would have thought proper. We will make up for it! And I think you had a great and valuable time with your dad instead.

# Contents

<b>Abstract</b>	<b>III</b>
<b>Acknowledgments</b>	<b>IV</b>
<b>List of Figures</b>	<b>VIII</b>
<b>List of Tables</b>	<b>XII</b>
<b>List of Symbols</b>	<b>XIII</b>
<b>1 Introduction</b>	<b>1</b>
1.1 Characterization of the term metamaterial . . . . .	1
1.2 Motivation . . . . .	1
1.3 Outline of the thesis . . . . .	5
1.4 Main contributions . . . . .	6
<b>2 Finite Element modelling of vibroacoustic systems</b>	<b>8</b>
2.1 Introduction . . . . .	8
2.2 General approach . . . . .	9
2.2.1 Overview . . . . .	10
2.2.2 Discretisation . . . . .	12
2.3 Problem description . . . . .	15
2.4 Acoustic fluid . . . . .	16
2.4.1 Finite Element model for the acoustic domain . . . . .	17
2.4.2 Boundary conditions of the acoustic domain . . . . .	18
2.5 Linear elastic solid . . . . .	20
2.5.1 Finite Element model for the structural domain . . . . .	22
2.5.2 Boundary conditions of the structural domain . . . . .	23
2.6 Coupling between solid and fluid domain . . . . .	24
2.7 Conclusion . . . . .	26
<b>3 Characterization of porous materials</b>	<b>27</b>
3.1 Introduction . . . . .	27
3.2 Johnson-Champoux-Allard Model for porous materials . . . . .	29
3.3 Finite Element model for porous materials . . . . .	32
3.3.1 Classical displacement based formulation . . . . .	32
3.3.2 Mixed displacement-pressure formulation . . . . .	36
3.3.3 New mixed formulation . . . . .	39

3.3.4	Equivalent fluid model . . . . .	40
3.3.5	Total displacement formulation . . . . .	41
3.3.6	Overview over different formulations . . . . .	42
3.3.7	Application of the JCAM for modelling single-phase materials . . . . .	42
3.4	Coupling and boundary conditions for porous media . . . . .	42
3.4.1	Excitations . . . . .	44
3.4.2	Supports . . . . .	45
3.4.3	Poroelastic-elastic coupling . . . . .	46
3.4.4	Poroelastic-acoustic coupling . . . . .	47
3.4.5	Poroelastic-poroelastic coupling . . . . .	47
3.4.6	Poroelastic-membrane coupling . . . . .	48
3.4.7	Numerical implementation . . . . .	48
3.5	Comparison of the formulations on test configurations . . . . .	58
3.5.1	Definition of the test configurations . . . . .	58
3.5.2	Analysis of the test cavity without absorber . . . . .	60
3.5.3	Comparison with reference solution . . . . .	61
3.5.4	Comparison of the different formulations . . . . .	62
3.5.5	Evaluation of the approximation error introduced by the reduced classical formulation . . . . .	67
3.5.6	Summary . . . . .	68
3.6	Conclusion . . . . .	69
<b>4</b>	<b>Modelling strategies for periodic structures</b>	<b>70</b>
4.1	Introduction . . . . .	70
4.2	Basic theory . . . . .	70
4.2.1	Selection of the unit cell . . . . .	71
4.2.2	Characterization of the unit cell . . . . .	71
4.2.3	Introduction of the periodicity . . . . .	72
4.3	Wave propagation along the structure . . . . .	73
4.3.1	Problem description . . . . .	73
4.3.2	Inverse approach . . . . .	74
4.3.3	Direct approach . . . . .	75
4.4	Sound transmission through the structure . . . . .	76
4.4.1	Problem description . . . . .	77
4.4.2	General pre-processing . . . . .	78
4.4.3	Linear elastic boundary layers . . . . .	80
4.4.4	Porous boundary layers . . . . .	82
4.5	Conclusion . . . . .	85
<b>5</b>	<b>Numerical studies</b>	<b>86</b>
5.1	Introduction . . . . .	86
5.2	Stop band behaviour of periodic metamaterials . . . . .	86
5.2.1	Preliminary study . . . . .	87
5.2.2	Impact of the inclusion shape . . . . .	89
5.2.3	Impact of subsystems within the inclusions . . . . .	97

---

5.3	Sound transmission characteristics of periodic metamaterials . . . . .	101
5.3.1	Preliminary study . . . . .	101
5.3.2	Impact of inclusions on the sound transmission loss through linear elastic structures . . . . .	105
5.3.3	Dispersion characteristics of periodically structured porous metamaterials . . . . .	109
5.4	Conclusion . . . . .	117
<b>6</b>	<b>Conclusion</b>	<b>118</b>
6.1	Summary of the presented modelling strategies for acoustic metamaterials . .	118
6.2	Main findings of the numerical studies on exemplary structures . . . . .	119
6.3	Outlook . . . . .	120
	<b>Bibliography</b>	<b>122</b>

# List of Figures

2.1	Deformation pattern of one-dimensional structure (- - -) and approximation of it using linear shape functions with different numbers of equidistant nodes per wavelength: three nodes per wavelength (—), five nodes per wavelength (—) and nine nodes per wavelength (—). . . . .	11
2.2	Element in original (left) and elemental (right) coordinates. . . . .	13
2.3	Vibroacoustic domain and its boundaries. . . . .	16
3.1	Porous domain modelled as statistical multiphase continuum. . . . .	27
3.2	Coupled vibroacoustic system consisting of linear elastic, acoustic and porous domain. . . . .	44
3.3	Test configurations for comparison of different JCAM formulations. . . . .	59
3.4	Mean quadratic pressure in cavity without porous absorber (—); (—) mark eigen-tones of acoustic cavity. . . . .	60
3.5	Pressure distribution within acoustic cavity for eigen-tones in frequency range from 0 to 2000 Hz. . . . .	61
3.6	Mean quadratic pressure in cavity with porous absorber at one edge (—) and reference solution given in [Rumpler et al 2013] (- - -); absorber is modelled using classical formulation. . . . .	62
3.7	Mean quadratic pressure in cavity without porous absorber (—), with porous absorber at one edge (- - -) and with porous absorber at two edges (—); absorbers are modelled using classical formulation. . . . .	63
3.8	Mean quadratic pressure in cavity with porous absorber at one edge for classical formulation (—), reduced classical formulation (· · ·), mixed formulation (—), new mixed formulation (· · ·), rigid equivalent fluid (—) and limp equivalent fluid (—). . . . .	63
3.9	For acoustic cavity with porous layer at one edge: deviation between $L_p$ corresponding to classical formulation and reduced classical formulation (· · ·), mixed formulation (—), new mixed formulation (· · ·), rigid equivalent fluid (—), limp equivalent fluid (—). . . . .	64
3.10	Deformation of absorber at 1700 Hz; left: displacement of solid phase of porous absorber; right: displacement of fluid phase of porous absorber. . . . .	65
3.11	Deformation of absorber at 1530 Hz; left: displacement of solid phase of porous absorber; right: displacement of fluid phase of porous absorber. . . . .	65
3.12	Mean quadratic pressure in cavity with porous absorbers at two edges for classical formulation (—), reduced classical formulation (· · ·), mixed formulation (—), new mixed formulation (· · ·), rigid equivalent fluid (—) and limp equivalent fluid (—). . . . .	66

3.13	For acoustic cavity with porous layers at two edges: deviation between $L_p$ corresponding to classical formulation and reduced classical formulation ( $\cdots$ ), mixed formulation ( $-$ ), new mixed formulation ( $\cdot\cdot\cdot$ ), rigid equivalent fluid ( $\dashv$ ), limp equivalent fluid ( $\dashv$ ). . . . .	66
3.14	Deviation of linearised equivalent bulk modulus from exact solution: real part ( $-$ ), imaginary part ( $- - -$ ) and absolute value ( $\dashv$ ); ( $\dashv$ ) marks dimensionless frequency ratio for $f = 500$ Hz. . . . .	67
3.15	Deviation of linearised viscous drag from exact solution: real part ( $-$ ), imaginary part ( $- - -$ ) and absolute value ( $\dashv$ ); ( $\dashv$ ) marks dimensionless frequency ratio for $f = 500$ Hz. . . . .	67
4.1	Selection of optimal unit cell. . . . .	71
4.2	Distinction of waves regarding to their propagation characteristics. . . . .	73
4.3	Periodic metamaterial. . . . .	73
4.4	Periodic metamaterial with incident inclined plane wave. . . . .	77
5.1	Dispersion curves for homogeneous unit cell ( $-$ ); auxiliary line ( $- - -$ ) and markers for certain combinations of phase and frequency $\square$ , for which deformation pattern is plotted in figure 5.2. . . . .	87
5.2	Deformed shape of homogeneous periodic structure for a) ( $\frac{\pi}{2}$ rad, 5.33 kHz), b) ( $\frac{\pi}{2}$ rad, 20.68 kHz) and c) ( $\frac{\pi}{2}$ rad, 30.09 kHz). . . . .	88
5.3	First set of inclusion shapes: a) circle, b) rectangle, c) rhombus. . . . .	89
5.4	Dispersion curves for unit cell with circular inclusion. . . . .	90
5.5	Dispersion curves for unit cell with rectangular inclusion. . . . .	90
5.6	Dispersion curves for unit cell with rhombic inclusion. . . . .	90
5.7	Comparison of stop band width for different inclusion types: circle ( $-$ ), rectangle ( $\dashv$ ) and rhombus ( $\dashv$ ). . . . .	91
5.8	Distribution of mass with respect to $x$ : circle ( $-$ ), rectangle ( $\dashv$ ) and rhombus ( $\dashv$ ); ( $- - -$ ) marks average mass density. . . . .	91
5.9	Second set of cell geometries; left: inclusions; right: notches. . . . .	92
5.10	Correlation between variance in mass distribution and stop band width for unit cell with rectangular inclusion. . . . .	93
5.11	Correlation between variance in mass distribution and stop band width for unit cell with rectangular notch. . . . .	93
5.12	Dispersion curves for unit cell with circular inclusion ( $-$ ) and circular notch ( $- - -$ ); for combinations of phase and frequency marked by $\square$ , deformation pattern is plotted in figure 5.15. . . . .	94
5.13	Dispersion curves for unit cell with rectangular inclusion ( $-$ ) and rectangular notch ( $- - -$ ); for combinations of phase and frequency marked by $\square$ , deformation pattern is plotted in figure 5.16. . . . .	95
5.14	Stop band location and width of unit cells with differently shaped inclusions but equal variance in mass distribution. . . . .	95
5.15	Deformed shape of periodic structure with circular inclusion for a) ( $\pi$ rad, 26.63 kHz) and circular notch for b) (0 rad, 34.54 kHz), c) (1.31 rad, 26.63 kHz), d) (2.28 rad, 26.63 kHz). . . . .	96

5.16	Deformed shape of periodic structure with rectangular inclusion for a) ( $\pi$ rad, 27.79 kHz) and rectangular notch for b) (0.89 rad, 27.79 kHz), c) (2.41 rad, 27.79 kHz), d) ( $\pi$ rad, 32.30 kHz). . . . .	97
5.17	Spring alignments to be considered: a) single-spring inclined by angle $\varphi$ , b) double-spring. . . . .	97
5.18	Dispersion curves for unit cell with circular inclusion without TMD (- - -) and with single-spring TMD inclined by $\frac{\pi}{4}$ rad (—); (- · -) marks eigenfrequency of TMD. . . . .	98
5.19	Dispersion curves for unit cell with circular inclusion without TMD (- - -) and with single-spring TMD inclined by 0 rad (—); (- · -) marks eigenfrequency of TMD. . . . .	99
5.20	Dispersion curves for unit cell with circular inclusion without TMD (- - -) and with single-spring TMD inclined by $\frac{\pi}{2}$ rad (—); (- · -) marks eigenfrequency of TMD. . . . .	99
5.21	Dispersion curves for unit cell with circular inclusion and single-spring TMD inclined by 0 rad (—), $\frac{\pi}{8}$ rad (- - -), $\frac{\pi}{4}$ rad (- · -), $\frac{3\pi}{8}$ rad (- - -) and $\frac{\pi}{2}$ rad (—); (- · -) marks eigenfrequency of TMD. . . . .	99
5.22	Dispersion curves for unit cell with circular inclusion and single-spring TMD inclined by $\frac{\pi}{4}$ rad (- - -) and $-\frac{\pi}{4}$ rad (- - -); (- · -) marks eigenfrequency of TMD. . . . .	100
5.23	Dispersion curves for unit cell with circular inclusion with single-spring TMD inclined by 0 rad (- - -) and $\frac{\pi}{2}$ rad (- · -) and with double-spring TMD (· · ·). . . . .	100
5.24	Dispersion curves for unit cell with circular inclusion and regular double-spring TMD (—) and double-spring TMD inclined by $-\frac{\pi}{4}$ rad (- - -); (- · -) marks eigenfrequency of TMD. . . . .	100
5.25	Transmission loss through plate for excitation with plane wave inclined by $50^\circ$ : analytical solution (—), WFEM (***) . . . . .	102
5.26	Porous layer excited by normal incident plane wave. . . . .	103
5.27	Real part of surface impedance of porous layer according to [Atalla et al 1998] (***), WFEM with classical formulation (—), WFEM with reduced classical formulation (· · ·) and unit cell model with fixed lateral displacements and $p_t = 0$ (—). . . . .	104
5.28	Imaginary part of surface impedance of porous layer according to [Atalla et al 1998] (***), WFEM with classical formulation (—), WFEM with reduced classical formulation (· · ·) and unit cell model with fixed lateral displacements and $p_t = 0$ (—). . . . .	104
5.29	Deviation of linearised equivalent bulk modulus from exact solution: real part (—), imaginary part (- - -) and absolute value (—); (—) marks dimensionless frequency ratio for $f = 500$ Hz. . . . .	105
5.30	Deviation of linearised viscous drag from exact solution: real part (—), imaginary part (- - -) and absolute value (—); (—) marks dimensionless frequency ratio for $f = 500$ Hz. . . . .	105
5.31	Transmission loss for excitation with plane wave inclined by $\frac{\pi}{4}$ rad and structure with circular inclusions (—), rectangular inclusions (—), rhombic inclusions (—) and without inclusions (—); frequency range between 100 and 1000 Hz. . . . .	106



5.32	Transmission loss for excitation with plane wave inclined by $\frac{\pi}{4}$ rad for homogeneous structure with full density (—) and reduced equivalent density (- - -); black curve corresponds to WFEM results, green curve to analytical solution given in [Fahy and Gardonio 2007]. . . . .	108
5.33	Transmission loss for excitation with plane wave inclined by $\frac{\pi}{4}$ rad and structure with circular inclusions (—), rectangular inclusions (—), rhombic inclusions (—) and without inclusions (—); upper and lower limits of stop bands computed for different inclusion shapes in section 5.2.2 are marked by dashed vertical lines. . . . .	109
5.34	Porous metamaterial with concentrated mass inclusions. . . . .	110
5.35	Absorption coefficient of porous layer without inclusions for $\Theta = \frac{\pi}{4}$ rad (- - -) and $\Theta = 0$ rad (—). . . . .	111
5.36	Absorption coefficient of porous metamaterial with concentrated mass inclusions at different heights: $h_m = 0.015$ m (—), $h_m = 0.010$ m (—), $h_m = 0.005$ m (—) and without inclusions (- - -); (—) marks frequency for which thickness of porous layer equals one quarter of vertical component of wavelength of excitation. . . . .	112
5.37	Two-shell wall with inclusions. . . . .	113
5.38	Transmission loss of two-shell wall: with aluminium inclusions (- - -), with gypsum board inclusions (—) and without inclusions (—); $\square$ marks frequencies for which deformation pattern is plotted in figures 5.39-5.41. . . . .	114
5.39	Deformation pattern of two-shell wall without inclusions for different frequencies: a) 684 Hz, b) 2618 Hz and c) 2093 Hz; for porous domain solid phase displacements are depicted. . . . .	115
5.40	Deformation pattern of two-shell wall with aluminium inclusions for different frequencies: a) 780 Hz, b) 1568 Hz and c) 2737 Hz; for porous domain solid phase displacements are depicted. . . . .	116
5.41	Deformation pattern of two-shell wall with gypsum board inclusions for different frequencies: a) 756 Hz, b) 2451 Hz and c) 3024 Hz; for porous domain solid phase displacements are depicted. . . . .	117

## List of Tables

2.1	Wave speeds and propagation patterns corresponding to wave types emerging in elastic solids; blue arrows mark propagation direction, orange arrows mark respective direction of oscillation. . . . .	21
3.1	Material parameters corresponding to porous domain. . . . .	30
3.2	Overview over different formulations of the JCAM used within this thesis. . .	43
3.3	Overview over implementation of coupling and boundary conditions. . . . .	57
3.4	Material parameters of porous absorber. . . . .	59
5.1	Material parameters of aluminium. . . . .	87
5.2	Variance of mass distribution corresponding to first set of unit cells. . . . .	91
5.3	Material parameters of studied plate. . . . .	101
5.4	Material parameters of porous absorber. . . . .	103
5.5	Dimensions of two-shell wall with inclusions. . . . .	112
5.6	Material parameters of gypsum board. . . . .	113

# List of Symbols

## Operators and Supplements

$i = \sqrt{-1}$	Imaginary unit
$\tilde{\square}$	Marks frequency dependent quantities
$\Delta$	Laplace operator
$\nabla$	Nabla operator
$\nabla a$	Gradient of a scalar-valued function $a$
$\text{div } \mathbf{a}$	Divergence of a vector field $\mathbf{a}$
$d\square$	Infinitesimal quantity
$\int a dx$	Indefinite integral of a function $a$ with respect to $x$
$\frac{da}{dx}$	Derivative of a function $a$ with respect to $x$
$\frac{\partial a}{\partial \mathbf{x}} = \nabla a \cdot \mathbf{x}$	Partial derivative of a function $a$ with respect to a vector $\mathbf{x}$
$\delta a$	First variation of a function $a$
$\mathbf{A}^\top$	Transpose of a matrix $\mathbf{A}$
$\mathbf{A}^H$	Complex conjugate transpose of a matrix $\mathbf{A}$
$\mathbf{a} \cdot \mathbf{b}$	Scalar product of two vectors $\mathbf{a}$ and $\mathbf{b}$
$\mathbf{a} \times \mathbf{b} = \mathbf{c}; c_i = a_i b_i$	Component-wise multiplication of two vectors $\mathbf{a}$ and $\mathbf{b}$
$\mathbf{A} : \mathbf{B} = \sum_{ij} A_{ij} B_{ij}$	Tensor scalar product of two tensors $\mathbf{A}$ and $\mathbf{B}$
$\text{diag}(\mathbf{a}) = \mathbf{A}$	Maps a vector $\mathbf{a}$ on diagonal of a matrix $\mathbf{A}$ , whereby off-diagonal entries of $\mathbf{A}$ are zero

## Greek Symbols

$\alpha$	–	Absorption coefficient
$\tilde{\alpha}$		Auxiliary variable in new mixed formulation of JCAM
$\alpha_\infty$	–	Tortuosity of porous domain
$\gamma$	–	Heat capacity of fluid phase of porous domain
$\tilde{\gamma}$		Auxiliary variable in mixed formulation of JCAM
$\Gamma$		Boundary of two-dimensional domain
$\Gamma_{\square D}$		Dirichlet boundary
$\Gamma_{\square N}$		Neumann boundary
$\Gamma_{\text{aR}}$		Robin boundary of acoustic fluid
$\varepsilon$	–	Strain tensor
$\eta$	$\frac{\text{Ns}}{\text{m}^2}$	Viscosity of fluid phase of porous domain
$\eta_e, \eta_s$	–	Damping ratio of linear elastic solid resp. solid phase of porous domain
$\Theta$	rad	Angle of inclination for excitation of periodic metamaterial
$\kappa = \kappa_r + \mathbf{i}\kappa_i$		Complex wavenumber
$\kappa_i$		Imaginary part of wavenumber $\kappa$
$\kappa_r$		Real part of wavenumber $\kappa$
$\lambda_e, \lambda_s$	Pa	First Lamé parameter of linear elastic solid resp. solid phase of porous domain
$\lambda_{\eta, \square}$	Pa	Complex first Lamé coefficient considering structural damping
$\Lambda$	m	Viscous length of porous domain
$\Lambda'$	m	Thermal length of porous domain
$\mathbf{\Lambda}_L, \mathbf{\Lambda}_R$		Left and right Bloch matrix
$\mu$		Wave propagation constant
$\mu_e, \mu_s$	Pa	Second Lamé parameter of linear elastic solid resp. solid phase of porous domain
$\mu_{\eta, \square}$	Pa	Complex second Lamé coefficient considering structural damping
$\nu$	–	Poisson's ratio
$(\xi, \eta)$		Elemental coordinates
$\rho$	$\frac{\text{kg}}{\text{m}^3}$	Density
$\tilde{\rho}$	$\frac{\text{kg}}{\text{m}^3}$	Auxiliary density in mixed formulation of JCAM
$\tilde{\rho}_f$	$\frac{\text{kg}}{\text{m}^3}$	Equivalent fluid density of porous domain
$\tilde{\rho}_s$	$\frac{\text{kg}}{\text{m}^3}$	Equivalent solid density of porous domain
$\tilde{\rho}_{\text{sf}}$	$\frac{\text{kg}}{\text{m}^3}$	Equivalent coupling density of porous domain
$\sigma$	$\frac{\text{Ns}}{\text{m}^4}$	Flow resistivity of porous domain

$\boldsymbol{\sigma}$	$\frac{\text{N}}{\text{m}^2}$	Stress tensor
$\hat{\boldsymbol{\sigma}}_s$	$\frac{\text{N}}{\text{m}^2}$	In vacuo stress tensor of solid phase of porous domain
$\boldsymbol{\sigma}_t$	$\frac{\text{N}}{\text{m}^2}$	Total stress tensor of porous domain
$\tau$	–	Transmission coefficient
$\Phi = \frac{V_f}{V_t}$	–	Porosity of porous domain
$\omega = 2\pi f$	$\frac{\text{rad}}{\text{s}}$	Circular frequency
$\Omega$		Interior of two-dimensional domain

## Latin Symbols

$\tilde{A}$		Auxiliary variable for description of porous media
$\tilde{b}$		Viscous drag of porous domain
$\mathbf{B}$		Strain-displacement matrix
$c_{\text{air}}$	$\frac{\text{m}}{\text{s}}$	Wave speed in air
$c_B$	$\frac{\text{m}}{\text{s}}$	Wave speed of bending wave
$c_L$	$\frac{\text{m}}{\text{s}}$	Wave speed of longitudinal wave
$c_P$	$\frac{\text{m}}{\text{s}}$	Wave speed of compressional wave
$c_Q$	$\frac{\text{m}}{\text{s}}$	Wave speed of quasi-longitudinal wave
$c_S$	$\frac{\text{m}}{\text{s}}$	Wave speed of shear wave
$\mathbf{C}$		Damping matrix
$D_a$	$\frac{\text{kg rad}}{\text{m}^2 \text{s}^2}$	Equivalent fluid density
$\mathbf{D}$		Dynamic stiffness matrix
$\mathbf{e}$		Vector of excitations
$E$	Pa	Young's modulus
$E_{\eta, \square}$	Pa	Complex young's modulus considering structural damping
$E(X)$	$\frac{\text{kg}}{\text{m}^2}$	Average mass density
$\mathbf{E}$		Elasticity matrix
$f$	Hz	Circular frequency
$f_c$	Hz	Coincidence frequency for $\Theta = \frac{\pi}{2}$ rad
$f_{c, \Theta}$	Hz	Coincidence frequency at oblique incidence
$f_{\text{room}}$	Hz	Eigen-tone of rectangular acoustic cavity
$\mathbf{f}$		Vector of right hand side contributions (resp. internal reactions in section 4.4)
$h$	m	Height or thickness of a structural element
$H_1, H_2$		Auxiliary variables in linearised classical formulation of JCAM

$I$	$\text{m}^4$	Second moment of inertia corresponding to a beam's cross section
$\mathbf{I}$		Identity matrix
$k$	$\frac{\text{rad}}{\text{m}}$	Wavenumber
$\tilde{K}_f$		Bulk modulus of fluid phase of porous domain
$\mathbf{K}$		Stiffness matrix
$l_x, l_y, l_z$	$\text{m}$	Dimensions of rectangular acoustic cavity
$L_p$	$\text{dB}$	Mean quadratic pressure in an acoustic cavity
$L_x$	$\text{m}$	Length of a unit cell
$m$	$\frac{\text{kg}}{\text{m}^2}$ resp. $\text{kg}$	Surface density of a membrane resp. mass of an inclusion
$\mathbf{M}$		Mass matrix
$\mathbf{n}$		Normal vector
$n_x, n_y, n_z$		Counting variables
$N$		Shape function
$\mathbf{N}_{p\Omega}$		Matrix of shape functions for two-dimensional element with four nodes and scalar state variable $q_p$
$\mathbf{N}_{p\Gamma}$		Matrix of shape functions for one-dimensional element with two nodes and scalar state variable $q_p$
$\mathbf{N}_{u\Omega}$		Matrix of shape functions for two-dimensional element with four nodes and vectorial state variable $\mathbf{q}_u$
$\mathbf{N}_{u\Gamma}$		Matrix of shape functions for one-dimensional element with two nodes and vectorial state variable $\mathbf{q}_u$
$p_a$	$\text{Pa}$	Acoustic pressure
$p_f$	$\text{Pa}$	Pore pressure
$p_i, p_r, p_t$	$\text{Pa}$	Incident, reflected and transmitted pressure field
$p_{\text{ref}} = 20 \cdot 10^{-6}$	$\text{Pa}$	Reference sound pressure in air
$\tilde{P}$		Auxiliary variable for description of porous media
$P_0$	$\text{Pa}$	Standard pressure of fluid phase of porous domain
$Pr$	–	Prandtl number of fluid phase of porous domain
$q$		State variable
$q_p$		Scalar state variable
$\mathbf{q}_u$		Vectorial state variable
$\mathbf{q}$		Vector of state variables
$\tilde{Q}$		Auxiliary variable for description of porous media
$r$		Reflection coefficient
$\tilde{R}$		Auxiliary variable for description of porous media

<b>R</b>		Reduction matrix
$\mathbf{t}_m$		Traction forces corresponding to membrane
$T$	dB	Transmission loss
<b>T</b>		Transfer matrix
<b>u</b>	m	Displacement vector
$u_{\square,n}$	m	Normal displacement
$\mathbf{u}_t$	m	Total displacement vector of porous domain
$v_{\square,n}$	$\frac{m}{s}$	Normal velocity
$\text{Var}(X)$	$\frac{kg^2}{m^3}$	Variance of mass distribution
$V_f$	$m^3$	Volume fraction of porous domain occupied by fluid phase
$V_t$	$m^3$	Total volume corresponding to porous domain
$\delta W_I$	Nm	Virtual work of internal forces
$\delta W_T$	Nm	Virtual work corresponding to inertia effects
$\delta W_E$	Nm	Virtual work of external forces
$(x,y)$		Cartesian coordinates
$\Delta x$	m	Nodal intake surface
$X$	$\frac{kg}{m^2}$	Mass density
$Z_a$	$\frac{m}{s Pa}$	Normal impedance
$Z_n$	$\frac{s}{m rad}$	Surface impedance of porous domain

## Indices and superscripts

$\square_a$	Indicates affiliation to acoustic fluid
$\square_e$	Indicates affiliation to linear elastic solid
$\square_f$	Indicates affiliation to fluid phase of porous domain
$\square_m$	Indicates affiliation to limp, impermeable membrane
$\square_p$	Indicates affiliation to porous domain
$\square_s$	Indicates affiliation to solid phase of porous domain
$\square_{\square_e}$	Denotes representation on element level
$\square^c$	Indicates affiliation to classical formulation of JCAM
$\square^{c*}$	Indicates affiliation to linearised/reduced classical formulation of JCAM
$\square^m$	Indicates affiliation to mixed formulation of JCAM
$\square^{m*}$	Indicates affiliation to new mixed formulation of JCAM

- <sub>B</sub>      Marks correspondence to upper and lower boundary nodes of a unit cell
- <sub>I</sub>      Marks correspondence to internal nodes of a unit cell
- <sub>L</sub>      Marks correspondence to nodes at left coupling interface of a unit cell
- <sub>R</sub>      Marks correspondence to nodes at right coupling interface of a unit cell



# 1 Introduction

## 1.1 Characterization of the term metamaterial

To begin this work, the term metamaterial shall be specified. In general the term metamaterial describes a structure having either specifically designed geometric characteristics or a material composition leading to physical behaviour that cannot be observed among usual systems. Examples are systems that expand under compression or suppress signal propagation for certain excitation frequencies. Often, the mode of action of acoustic metamaterials is based on the concept of negative effective density and/or negative effective stiffness. [Lee and Wright 2016] discusses these phenomena using simple examples.

In the context of this thesis the term metamaterial is used in conjunction with infinite periodic structures consisting of repetitive unit cells, whereby the unit cell is the smallest segment whose sequencing results in the periodic structure. By appropriately shaping the unit cell, so called stop bands, being frequency ranges where no free wave propagation occurs, can be observed. According to [Claeys et al 2013; Sheng and Chan 2005] the occurrence of these stop bands can be explained by two different approaches: First, destructive interference between transmitted and reflected waves can impede wave propagation in certain frequency ranges. Second, stop bands can be caused by local resonances which, for example, are induced by adding tuned mass dampers to the structure of the unit cell.

## 1.2 Motivation

Current issues such as climate change and scarcity of raw materials present us with new stakes. In order to meet these challenges, the industry is striving for slender designs. These require fewer raw materials for production compared to bulkier components. In addition, lighter vehicles and aircraft also mean lower energy consumption and thus lower carbon emissions, which is an important goal in view of global warming.

Unfortunately, light weight designs can often be easily set in vibration and thus can suffer from unfavourable vibroacoustic properties due to the high stiffness-to-mass ratio. To improve the vibrational performance without increasing the mass, slender and adjustable vibration reduction measures are required. Current research shows that acoustic metamaterials provide possibilities to tackle those requirements.

Various studies show that modifications of the unit cell lead to a manipulation of the wave propagation along a periodic structure. The following is a brief overview of relevant literature that has contributed to the motivation of this thesis.

[Claeys et al 2013] shows that a periodic assembly of tuned mass dampers (TMDs) on a plate can cause stop bands. The numerical simulations are performed using the Wave Finite Element Method (WFEM). The TMDs are modelled as discrete mass spring systems. [Claeys et al 2017] confirms this outcome employing a more realistic continuous model for the resonator both numerically using the WFEM and experimentally. The frequency range of the observed stop bands depends on the characteristics of the TMD, i.e. mass, spring stiffness and damping. [Miksch et al 2019] uses the WFEM to take a closer look at this behaviour and describes how TMDs affect the decay characteristics of waves that propagate in periodic structures. [Chronopoulos et al 2015] employs analytical approaches and the WFEM to model periodic structures equipped with negative stiffness oscillators. Care is taken to ensure that the structures under investigation are capable of bearing static loads. It is shown that the negative stiffness oscillators can be tuned to maximise the damping within the system for a targeted frequency range.

There are already many publications investigating how, for certain frequency ranges, the absorption of porous layers can be improved by embedding inclusions. While the thickness of a porous layer without inclusions has to equal at least one quarter of the wavelength of the excitation in order to attenuate it effectively [Deckers et al 2016], various authors observe absorption peaks below the quarter-wavelength frequency for porous layers with periodic inclusions. Most often the pore framework is assumed to be rigid. Except [Boutin and Becot 2015] who uses a special homogenization approach and [Kidner et al 2006] who performs only experimental studies, all publications cited below model the porous domain numerically using the Johnson–Champoux–Allard model (JCAM). [Kidner et al 2006] proves experimentally that the insertion loss of a porous layer can be enhanced at low frequencies by embedding mass inclusions. It is shown that the inclusions act as local resonators increasing the structures' impedance. By adapting the position of the inclusion within the porous layer, the resonance frequency can be tuned. [Groby et al 2008] studies the acoustic behaviour of a rigid frame porous layer with periodically distributed macroscopic circular

aluminium and acrylic inclusions. In the implementation the multipole method is used in combination with the transfer matrix method. Stop bands in the audible frequency range are observed. [Groby et al 2011] analyses the absorption characteristics of a rigidly backed porous layer with circular inclusions employing the mode-matching method. The pore framework and the inclusions are assumed to be motionless. With one inclusion per period a nearly complete absorption peak below the quarter-wavelength resonance is observed. Additional absorption peaks occur with multiple inclusions per period. The results are interpreted via the occurrence of trapped modes between inclusions and rigid backing. [Nennig et al 2012] investigates a rigidly backed multilayer rigid frame porous structure with periodic inclusions using the mode-matching method. Here, as well, an improvement of the absorption behaviour due to the inclusions is found. Further, it is observed that open geometries behave more favourably compared to closed geometries. In addition to a validation with other numerical models, the calculation results are confirmed experimentally on an example structure. [Lagarrigue et al 2013] analyses the absorption potential of a porous metamaterial with slotted ring shaped inclusions. The solid phase of the porous domain and the inclusion are assumed to be motionless and the structure is backed by a rigid wall. The energy dissipation within the porous layer is enhanced by low frequency resonances of the inclusion and the excitation of a trapped mode between inclusion and rigid backing. Thereby the frequency range for which almost complete absorption is observed is wider, if the position of the slit of adjacent inclusions varies. The investigations are carried out numerically employing the Finite Element Method (FEM) and the Bloch Theorem. The results are confirmed experimentally on reference configurations. [Groby et al 2014] studies the adsorption potential of rigidly backed rigid frame porous media with rigid inclusions of different shape. The numerical investigations are carried out using the FEM. The periodicity is mapped by periodic boundary conditions according to the Bloch Theorem. For all studied inclusion shapes a low frequency absorption peak due to the excitation of a trapped mode between rigid backing and inclusion is observed. The absorption enhancement thereby mainly depends on the filling fraction of the inclusion and the flow resistivity and thickness of the porous layer. For convex inclusions, the low frequency absorption characteristics are not affected by the inclusion shape itself, but only by the filling fraction and the position of the inclusion within the porous layer. For non-convex ring torus inclusions a lower filling fraction is necessary to achieve a nearly total absorption peak than for the studied convex inclusion shapes. [Boutin and Becot 2015] shows that embedding Helmholtz resonators in rigid frame porous media (i.e. creating double porosity porous media) leads to favourable absorption characteristics in the lower frequency range. The numeric computations are carried out using a special homogenization method. The results are confirmed experimentally. [Deckers et al 2016] studies the impact of rigid circular inclusions as well as rigid C-shaped inclusions, whose aperture angle is chosen

to minimize the transmission coefficient, on the absorption capacity of a rigid frame porous layer. To map the studied geometries, the Wave Based Method is used in combination with a multi-level approach. For the investigated geometries a frequency dependent improvement of the absorption behaviour is found in comparison to a porous layer of the same thickness without inclusions. [Magliacano et al 2020] studies the wave propagation along rigid frame porous metamaterials with rigid cylindrical inclusions using the shift cell technique. For the analysed configuration the inclusions induce an increased transmission loss over the whole frequency range considered.

Up to now only few authors consider the deformations of the pore framework of porous metamaterials. [Zielinski 2007] studies the impact of mass inclusions on the acoustic absorption within a rigidly backed porous layer. The porous domain is mapped by the mixed displacement-pressure formulation of the JCAM. The studied metamaterial is modelled numerically using the FEM. The structure is excited by a normal incident plane wave. Thus, it is sufficient to model only one unit cell. The mass inclusions enhance the absorption of the porous layer in the mid frequency range. For a low-frequency range, however, a deterioration of the absorption is observed as a result of the inclusions. It is also found that the results are hardly affected by whether the inclusions are modelled as elastic continua or point masses. [Weisser et al 2016] analyses the absorption potential of rigidly backed elastic frame porous absorbers with elastic inclusions. Both filled and empty cylindrical inclusions are considered. For the numerical simulation the mode matching approach together with the Bloch wave representation and the multiple scattering theory is employed. The porous domain is modelled using the displacement based formulation of the JCAM. For the empty cylindrical inclusion a wide absorption band in the mid frequency range and an absorption peak at very low frequencies are observed. [Ahsani et al 2020] excites a rigidly backed elastic frame porous metamaterial with discrete mass inclusions by a normal incident plane wave. The porous domain is modelled employing the mixed displacement pressure formulation of the JCAM. It is shown that the observed absorption peaks are induced by the mass-spring effect. As a result of an optimization, a super-cell with multiple inclusions leading to a broad band absorption is found. The FEM is used as numerical solution approach.

The above-mentioned literature leaves space for the following main points of investigation for the present work:

- Is it possible to induce stop bands in linear elastic plates by embedding inclusions? If yes, do the stop bands resulting from the inclusions mainly result from the irregular mass distribution along the structure? Can an influence of the shape of the inclusion be detected and quantified?

- Will embedding inclusions containing TMDs in a material layer increase the noise reduction potential of the structure? Has the orientation of the TMDs an impact on the dispersion characteristic? Can waves inside the structure be deflected purposefully by adapting the orientation of the TMDs?
- When studying porous metamaterials: What happens when both the pore framework and the inclusions, up to now almost exclusively assumed to be rigid, are modelled elastically? Can previous observations be reproduced or do further phenomena occur?

Studying those points of investigation requires an efficient numerical method for mapping the dispersion properties of periodic metamaterials. This thesis employs the Wave Finite Element Method as it allows to study metamaterials with complex unit cell geometries and material compositions with reasonable computational effort. Elastic frame porous materials are represented using the Johnson-Champoux-Allard Model (JCAM).

## 1.3 Outline of the thesis

In this thesis vibroacoustic systems consisting of acoustic cavities, linear elastic structures and porous absorbers are modelled in the frequency domain using the FEM. An efficient approach to compute the wave propagation along periodic structures is described and a concept to compute the sound transmission through and absorption of periodic metamaterials with porous components is introduced. The potential of the modelling strategies is demonstrated on different numerical examples. The examples prove that periodic metamaterials with specific dispersion properties can be designed via a proper choice of unit cell geometry and material composition.

Chapter 2 starts with explaining why the FEM depicts an appropriate method to model the dynamic behaviour of vibroacoustic systems in the frequency domain. The general approach of the FEM is introduced. The method is specified on the example of a two dimensional system that is structured into quadrilateral elements. FEM formulations for acoustic and linear elastic elements along with the respective coupling and boundary conditions are given.

Chapter 3 deals with the numeric representation of porous domains. An overview of different mapping concepts is given. Among them, the JCAM is described in more detail. FEM representations for different formulations of the JCAM are given. A simplified formulation of the JCAM is introduced, which captures the dispersion characteristics in the low-frequency range, but involves a significantly lower calculation effort. It is explained how supports and

excitations of the porous domain can be introduced into a FEM model. Furthermore, the coupling conditions between porous media and other domains are treated in detail. Finally, the different formulations of the JCAM are compared on two numerical examples.

Chapter 4 introduces the WFEM as efficient concept to analyse the dispersion characteristics of periodic structures. Two approaches for evaluating the wave propagation along the structure are given. Subsequently it is described how the sound transmission through and absorption of periodic structures can be computed using the WFEM. The existing approach is extended for the case of periodic structures with porous boundary layers.

Chapter 5 applies the solution strategies presented in Chapter 4 on numerical examples. The focus of the numerical studies lies in evaluating the impact of inclusions and secondary vibrational systems on the wave propagation in periodic metamaterials.

Chapter 6 concludes this thesis summing up the research objectives achieved. In addition, an overview is given of which promising research topics could be developed on the basis of the present work.

## 1.4 Main contributions

This work differentiates itself from previous research done in the field with respect to the following aspects:

- Using a two-dimensional domain as an example, this thesis summarizes all the necessary elemental, boundary and coupling contributions needed to model vibroacoustic systems consisting of acoustic cavities, linear elastic structures, and porous absorbers using FEM in one document.
- This thesis discusses how porous absorbers can be integrated into a FEM model. The JCAM serves as a mathematical model for the description of porous media. The different formulations of the JCAM are compared in more detail than in the existing literature in this area. In addition, a simplified version of the JCAM is introduced, which provides sufficiently accurate results for many applications, but generates significantly less computational effort than the full model.
- A novel approach to compute the sound transmission through and absorption of periodic structures with elastic frame porous boundary layers modelled by the classical formulation of the JCAM is introduced. The approach is verified taking reference to

examples from the literature and its performance is demonstrated on numerical examples. In contrast to the existing approaches in the literature, the proposed approach fulfils all of the following criteria simultaneously: the deformation of the pore framework is considered, the system can not only be excited by normal incident but also by inclined plane waves, the reflected part of the exciting wave is imaged and complex inclusion geometries within the porous layer can be taken into account.

- Building on existing literature, this thesis examines how inclusions and secondary vibrational systems can be used as a measure to manipulate the dispersion characteristics and the vibroacoustic behaviour of periodic metamaterials in general.

## 2 Finite Element modelling of vibroacoustic systems

### 2.1 Introduction

For analysing the characteristics of vibroacoustic systems an efficient numerical solution scheme is needed. In the literature different procedures are proposed for this. The individual methods differ, among other things, with respect to the frequency range in which they can be usefully applied and with respect to the complexity of the geometries that can be mapped efficiently. The preferred variant depends on the respective application case. An overview over different methods is for example given in [Ochmann et al 2017]. A selection of solution schemes is summarized below.

One option is to model the system or parts of it using the Integral Transform Method as done in [Buchschnid 2011]. Here the system of coupled partial differential equations underlying the structure under consideration is first transformed into a system of decoupled partial differential equations using the Helmholtz theorem, which states that a continuous vector field can be represented as a superposition of a rotation-free and a source-free field. Performing a Fourier Transform from the original to the image space, a system of decoupled ordinary differential equations is obtained, which can be solved by using the corresponding boundary conditions in the image space. For simple geometries, the analytical solution of the system of differential equations in the original space can be determined by an inverse Fourier Transform. However, the Integral Transform Method is only usefully applicable for structures with limited geometrical complexity and accordingly only suitable for the analysis of acoustic metamaterials with simple geometries.

Another possibility to describe the dynamic behaviour of vibroacoustic systems is the Wave Based Method. As described in [Deckers et al 2014] the domain is structured into a limited number of convex subdomains. The number of subdomains thereby does not depend on the considered excitation frequency. The dynamic response variables are represented by



a frequency dependent number of wave functions, which represent an exact solution of the underlying differential equations and whose contribution factors are determined by a residual consideration at the boundaries of the domain. The degrees of freedom (DOFs) in the Wave Based Method are those contribution factors. As the domain discretisation is frequency independent, the method represents an efficient solution procedure for large frequency ranges, but is usually not able to map areas of high geometric complexity with reasonable effort. To cope with this issue, multi-level approaches [Atak 2014; Deckers et al 2016] or hybrid methods coupling p.e. Wave Based Method and FEM can be used [Jonckheere et al 2013; Deckers et al 2017]. [Deckers et al 2012; Lee et al 2016] show that the Wave Based Method can be employed to model porous materials.

In addition, there are a number of other methods such as the Boundary Element Method used for example in [Tanneau et al 2006]. It has the advantage that only a discretisation of the edges of the domain is required, but solving the resulting densely populated systems of equations is often associated with a higher computational effort compared to other methods.

In frequency ranges with a high mode density, which is typically the case in the high-frequency range, the Statistical Energy Analysis [Lyon and DeJong 1995] and the Transfer Matrix Method [Allard and Atalla 2009] have been applied to determine average quantities. However, the potential to determine quantities with high spatial resolution is limited.

In the context of this thesis the characteristics of vibroacoustic systems with complex geometries shall be evaluated over a large frequency range. The FEM, being one of the most common methods for modelling dynamic systems, meets these requirements. With it, structures of almost any geometrical complexity can be investigated with reasonable effort. In order to efficiently analyse their dynamic behaviour over larger frequency ranges, approaches to reduce the computational effort can be embedded. In the case of periodic structures, this can be done p.e. by applying the Bloch Theorem. The corresponding method will be discussed later in this thesis. In this chapter, the general principle of the FEM is summarized, followed by explaining how acoustic and structural domains are modelled using the FEM and how those domains are bounded and coupled.

## 2.2 General approach

At this point it should be emphasized that all analyses in this work are carried out in the frequency domain. A steady state harmonic excitation of the structures is assumed.

Using a FEM approach, a system's dynamic behaviour can be expressed by its equation of motion under steady state harmonic loading:

$$(\mathbf{K} + i\omega\mathbf{C} - \omega^2\mathbf{M})\mathbf{q} = \mathbf{f}, \quad (2.1)$$

with the system's stiffness, damping and mass matrices  $\mathbf{K}$ ,  $\mathbf{C}$  and  $\mathbf{M}$ .  $\mathbf{q}$  contains the state variables at the nodes and  $\mathbf{f}$  corresponds to the right hand side contributions. The system is formulated in the frequency domain with  $\omega$  being the angular frequency and  $i = \sqrt{-1}$  is the imaginary unit. Viscous damping is assumed. The individual entries in equation (2.1) are composed of elemental, boundary and interface contributions.

This section summarizes the steps necessary to investigate a system numerically using the FEM. While problem-specific steps will be taken up later in the thesis, this section will go into more detail on how the initially continuous system is transformed into a discrete one. The corresponding step is referred to as discretisation.

## 2.2.1 Overview

- **Definition of the system**

Here the structure to be analysed, in our case the vibroacoustic system, is specified concerning its geometry, material composition and boundary conditions.

- **Meshing**

Next, the geometry is divided into a finite number of elements. Depending on the element type, a specific number of nodes is created. The density of the mesh must be chosen in such a way that the relevant properties of the system can be represented appropriately by the FEM model. While too coarsely meshed models will not resolve the dynamic characteristics correctly, a too high number of elements corresponds to an oversized computation effort. Using an appropriate meshing one can model almost arbitrarily shaped finite structures using the FEM.

Figure 2.1 shows how the mesh density affects the results of the computation. One wavelength of the continuous deformation pattern of a one-dimensional structure shall be mapped by nodal values. Linear shape functions are used, meaning that the course of the deformation pattern between the nodes is assumed to be linear. One can see that when using three equidistant nodes per wavelength (blue dots), the deformation pattern can not be reproduced (blue curve). Doubling the mesh density by adding the green nodes (now using five nodes per wavelength), the deformation pattern (green curve)

can be reproduced. Using nine nodes per wavelength (adding the orange nodes), the approximation further improves (orange curve). For an equal mesh density replacing the linear shape functions by higher order shape functions would lead to a better approximation of the deformation pattern.

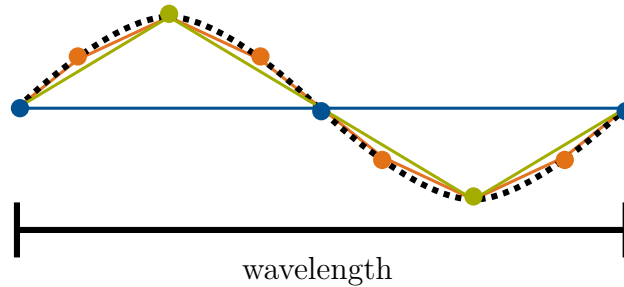


**Figure 2.1:** Deformation pattern of one-dimensional structure ( - - - ) and approximation of it using linear shape functions with different numbers of equidistant nodes per wavelength: three nodes per wavelength (—), five nodes per wavelength (—) and nine nodes per wavelength (—).

- **Computation of elemental, boundary and interface contributions**

At the element level, the contributions of the individual elements to the overall system are determined. This step can be broken down into the following substeps:

- Definition of the differential equation characterizing the respective system part, its boundaries and interfaces with other domains.
- Derivation of the weak integral form of the differential equation using e.g. the method of weighted residuals or the principle of virtual work.
- Discretisation: Transformation of the continuous system into a discrete one by approximating the primary variables using shape functions.
- Introduction of the shape functions into the weak integral form.
- Derivation of elemental, boundary and interface representations.

- **Assembling**

The matrix representation of the complete structure is computed by assembling the contributions corresponding to the individual elements, boundaries and interfaces. In the case of a conformal mesh the assembling process is done in such a way that the continuity of the state variables and the equilibrium of forces are fulfilled at the common nodes of adjacent elements. In the context of this work, conformal meshes are assumed.

If individual substructures are discretised differently, they can be coupled using so-called mortar approaches [Wohlmuth 2000].

- **Solving for unknowns**

Finally, the matrix representation of the complete structure (e.g. equation (2.1)) can be solved for the application dependent unknowns.

- **Convergence study**

After the solving step it is important to check whether the result has converged. If a reference solution is available (e.g. from the literature or from an analytical calculation), it is checked whether the simulation result and the reference solution match. If this is not the case, either the meshing or the choice of the shape functions has to be adjusted. If no reference solution is available, the mesh is refined step by step (or alternatively the degree of the shape functions is increased) until the solution does not change beyond a certain measure. If this is the case, it is assumed that the solution has converged. If the wavelengths of the oscillations in which the system is set under a given load can be estimated in advance, this can be used to predict the required mesh density.

- **Derivation of secondary variables**

Secondary variables can be post-processed from the converged solution. It should be noted that the convergence of secondary variables is usually poorer than that of the primary variables and that further convergence studies may be necessary.

## 2.2.2 Discretisation

After summarizing the individual steps of a FEM analysis, this section describes how a continuous state variable  $q$  is transferred into discrete values at the element's nodes via approximating the course of  $q$  by shape functions. The procedure will be explained by the example of a two-dimensional domain that is meshed by quadrilateral elements with four nodes. Both, the case of  $q$  being a scalar as well as a vectorial quantity is treated. The content is based on [Zienkiewicz et al 2005]; corresponding formulations for other element types and shape functions of other order than considered here can be found there.

For the problem under consideration, two different element types must be addressed: While the interior of the structure is meshed by quadrilateral elements with four nodes, boundaries and interfaces with other domains are represented by one-dimensional line elements with two

nodes. Below the focus is put on two-dimensional quadrilateral elements; the procedure for one-dimensional line elements is analogous.

To treat all elements within a FEM model in a standardized way, the isoparametric concept is applied. Thereby a coordinate transformation from the original coordinate system  $(x,y)$  to elemental coordinates  $(\xi, \eta)$  is performed (see figure 2.2), with  $(\xi, \eta)$  being defined in the range  $[-1,1]$ . Mathematically, the base change is mapped via the Jacobian matrix of the element.

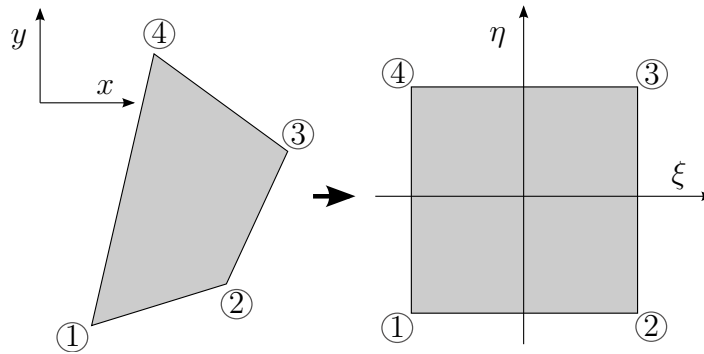


**Figure 2.2:** Element in original (left) and elemental (right) coordinates.

Mapping the geometry of the element on a new basis, also the state variable has to be transformed from original to elemental coordinates:  $q(x,y) \rightarrow q(\xi, \eta)$ . The elemental shape functions  $N_i$  used for approximating the course of  $q$  are directly defined in elemental coordinates and have to meet the following requirement:

$$N_i(\xi_j, \eta_j) = \begin{cases} 1 & i = j \\ 0 & i \neq j \end{cases}; \quad (2.2)$$

$(\xi_j, \eta_j)$  are the elemental coordinates of node  $j$ . Using bilinear shape functions for the considered two-dimensional element with four nodes results in:

$$\begin{aligned} N_1 &= (1 - \xi)(1 - \eta)/4, \\ N_2 &= (1 + \xi)(1 - \eta)/4, \\ N_3 &= (1 + \xi)(1 + \eta)/4, \\ N_4 &= (1 - \xi)(1 + \eta)/4. \end{aligned} \quad (2.3)$$

The state variable  $q(\xi, \eta)$  can be expressed using those shape functions:

$$q(\xi, \eta) \approx \sum_{i=1}^4 N_i(\xi, \eta) q_i. \quad (2.4)$$

Analogously the following set of linear shape functions for one-dimensional line elements delimited by two nodes A and B using  $\xi$  as boundary coordinate is introduced:

$$\begin{aligned} N_A &= (1 - \xi)/2 \\ N_B &= (1 + \xi)/2, \end{aligned} \quad (2.5)$$

resulting in

$$q(\xi) \approx \sum_{i=A,B} N_i(\xi) q_i. \quad (2.6)$$

The chosen set of shape functions has to be able to model the characteristics of the system appropriately. Also higher order shape functions can be used. Generally the mesh density and the order of the shape functions have to be adapted to each other to map the dynamic characteristics of the system of observation. As for an increasing frequency of observation the characteristic wavelength decreases, either the element size has to be reduced (h-refinement) or the polynomial order of the shape functions has to be increased (p-refinement) [Paolini et al 2018; Winter 2018]. While a p-refinement offers the advantage that no new mesh has to be created for higher frequencies, the element formulation has to be interfered with on a deeper level, since the shape functions are altered. Therefore, the h-refinement is basically the more user-friendly option. Independent of the refinement approach the calculation effort increases with an increasing frequency of observation. Performing a convergence study on the desired quantity gives conclusion on the appropriate discretisation for the problem of investigation.

Within this thesis both, scalar and vectorial state variables are dealt with. Therefore, it is specified in more detail how a scalar pressure field  $q_p$  and a vectorial displacement field  $\mathbf{q}_u$  are discretised using the shape functions introduced above. A further distinction is made between two-dimensional elements for the interior  $\Omega$  and one-dimensional elements for

boundaries and interfaces  $\Gamma$ . We get:

$$q_{p\Omega}(\xi, \eta) \approx \underbrace{\begin{bmatrix} N_1 & N_2 & N_3 & N_4 \end{bmatrix}}_{\mathbf{N}_{p\Omega}} \begin{bmatrix} p_1 & p_2 & p_3 & p_4 \end{bmatrix}^\top, \quad (2.7)$$

$$q_{p\Gamma}(\xi) \approx \underbrace{\begin{bmatrix} N_A & N_B \end{bmatrix}}_{\mathbf{N}_{p\Gamma}} \begin{bmatrix} p_A & p_B \end{bmatrix}^\top, \quad (2.8)$$

and

$$q_{u\Omega}(\xi, \eta) \approx \underbrace{\begin{bmatrix} N_1 & 0 & N_2 & 0 & N_3 & 0 & N_4 & 0 \\ 0 & N_1 & 0 & N_2 & 0 & N_3 & 0 & N_4 \end{bmatrix}}_{\mathbf{N}_{u\Omega}} \begin{bmatrix} \mathbf{u}_1 \\ \mathbf{u}_2 \\ \mathbf{u}_3 \\ \mathbf{u}_4 \end{bmatrix}, \quad (2.9)$$

$$q_{u\Gamma}(\xi) \approx \underbrace{\begin{bmatrix} N_A & 0 & N_B & 0 \\ 0 & N_A & 0 & N_B \end{bmatrix}}_{\mathbf{N}_{u\Gamma}} \begin{bmatrix} \mathbf{u}_A \\ \mathbf{u}_B \end{bmatrix}; \quad (2.10)$$

with

$$\mathbf{u}_i = \begin{bmatrix} u_{i,x} \\ u_{i,y} \end{bmatrix}. \quad (2.11)$$

## 2.3 Problem description

A vibroacoustic domain typically consists of a structural part and an acoustic fluid. In a numerical model, not only the individual subdomains, but also the interaction between them must be modelled. As FEM models are finite per definition, we need to specify the behaviour at the system boundaries. Figure 2.3 exemplarily shows the structure of a vibroacoustic system. The structural part  $\Omega_e$  corresponds to a linear elastic continuum; the acoustic domain is termed  $\Omega_a$ . The two subdomains are coupled at the interface  $\Gamma_{ae}$ . On the domain's boundaries either the primary variable (Dirichlet boundary condition,  $\Gamma_{eD}$ ,  $\Gamma_{aD}$ ) or a secondary variable (Neumann boundary condition,  $\Gamma_{eN}$ ,  $\Gamma_{aN}$ ) is prescribed. While the Dirichlet boundary condition defines entries of  $\mathbf{q}$ , a Neumann boundary condition results in a contribution to the right hand side vector  $\mathbf{f}$ . For the acoustic fluid a third type of boundary condition will be considered in this thesis: as described in more detail in section 2.4.2, for a simple radiation pattern, the Robin boundary condition  $\Gamma_{aR}$  can be used to model radiation towards infinity. Here, the normal impedance  $Z_a$ , expressed by the ratio of normal velocity

and pressure, is imposed at the boundary. To map partially unlimited fluid areas,  $Z_a$  at the Robin boundary is set equal to the impedance within the fluid domain.

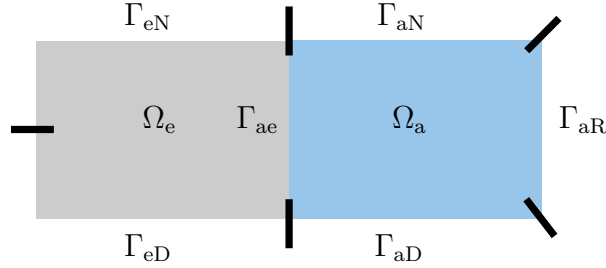


**Figure 2.3:** Vibroacoustic domain and its boundaries.

Following, the shape functions introduced in section 2.2.2 are used for deriving the elemental matrix representations and boundary and coupling contributions for the vibroacoustic system specified in figure 2.3.

## 2.4 Acoustic fluid

In the context of this thesis an acoustic fluid is defined as a medium that can only transmit normal stresses. The wave propagation takes place solely in the form of compressional waves being oscillations of the acoustic pressure  $p_a$ . The wave speed in the acoustic fluid is given as  $c_P = \sqrt{\frac{E_a}{\rho_a}}$ , with the fluid's bulk modulus  $E_a$  and density  $\rho_a$ . The Helmholtz equation is an ordinary differential equation and can be derived setting up the material law, the kinematics and the equilibrium at a reference fluid volume. A detailed derivation can be found in [Möser 2005]. It characterizes the wave propagation in acoustic fluids in the frequency domain:

$$\frac{1}{\rho_a} \Delta p_a + \omega^2 \frac{1}{E_a} p_a = 0. \quad (2.12)$$

$\Delta$  is the Laplace operator assigning the divergence of its gradient to the function it is applied on. The index  $\square_a$  expresses the affiliation of a variable to an acoustic fluid. It is assumed that only small oscillations occur and therefore nonlinear effects do not have to be considered. Furthermore, the acoustic fluid is supposed to be inviscid and adiabatic.



### 2.4.1 Finite Element model for the acoustic domain

To obtain the elemental matrices needed for a FE analysis, the weak form or variational formulation of equation (2.12) is needed. [Zienkiewicz et al 2005] states that the weak form can be derived from the differential equation using the method of weighted residuals by performing the following steps:

- Multiply the differential equation by a suitable weighting function.
- Integrate the resulting expression over the problem domain.
- Simplify the expression using integration by parts.
- Insert the boundary conditions.

While equation (2.12) shall be fulfilled at each point within the modelled domain, its weak form only requires fulfilment on average over the element to be described.

Applying the steps introduced above, the weak form of the Helmholtz equation is given as

$$\int_{\Omega_a} \left( \frac{1}{\rho_a} \nabla p_a \cdot \nabla \delta p_a - \frac{\omega^2}{E_a} p_a \delta p_a \right) d\Omega_a - \int_{\Gamma_a} \frac{1}{\rho_a} \frac{\partial p_a}{\partial \mathbf{n}_a} \delta p_a d\Gamma_a = 0, \quad (2.13)$$

with

$$\frac{\partial p_a}{\partial \mathbf{n}_a} = \nabla p_a \cdot \mathbf{n}_a. \quad (2.14)$$

$\mathbf{n}_a$  is the normal vector pointing outwards of the acoustic domain and the admissible variation  $\delta p_a$  is employed as weighting function. The scalar product of two vector fields  $\mathbf{a}$  and  $\mathbf{b}$  is denoted by  $\mathbf{a} \cdot \mathbf{b}$ . A detailed derivation of equation (2.13) can be found in [Franck 2009] or [Ochmann et al 2017].

In the following equation (2.13) is used for deriving the elemental matrices for a two-dimensional acoustic element with four nodes. The acoustic pressure  $p_a$  being the scalar state variable results in one degree of freedom (DOF) per node regardless of the dimensionality of the problem. Applying the Galerkin approach, both the state variable and the weighting function are approximated by the same shape functions (see [Zienkiewicz et al 2005]). When using the shape functions introduced in section 2.2.2, the reference frame has to be transformed from original to elemental respectively boundary coordinates. The base change results in an alteration of the integral's limits and is mathematically represented by

the Jacobian matrix. We can find the elemental mass and stiffness matrix corresponding to the acoustic fluid:

$$\mathbf{K}_{a_e} = \int_{\Omega_{a_e}} \frac{1}{\rho_a} (\nabla \mathbf{N}_{p\Omega})^\top \nabla \mathbf{N}_{p\Omega} \, d\Omega_{a_e}, \quad (2.15)$$

$$\mathbf{M}_{a_e} = \int_{\Omega_{a_e}} \frac{1}{E_a} \mathbf{N}_{p\Omega}^\top \mathbf{N}_{p\Omega} \, d\Omega_{a_e}. \quad (2.16)$$

$\Omega_{a_e}$  is the area occupied by a two-dimensional acoustic element. In a FE implementation the integrals above are usually evaluated using a numerical integration scheme like the Gaussian quadrature. Details on that can be found in [Bathe 2002].

## 2.4.2 Boundary conditions of the acoustic domain

Besides modelling the acoustic domain itself, we also need to specify its boundaries. In the context of this thesis we differ between three different boundary conditions being the Dirichlet, Neumann and Robin boundary condition.

### Dirichlet boundary condition

The Dirichlet boundary condition prescribes the value of the primary variable at the respective boundary. In the case of an acoustic fluid, the acoustic pressure  $p_a$  is preset to the value  $p_\Gamma$ :

$$p_a - p_\Gamma = 0 \quad \text{on } \Gamma_{aD}. \quad (2.17)$$

$p_\Gamma = 0$  models a fully reflecting boundary. One option to employ a Dirichlet boundary condition into a FEM implementation is to restructure equation (2.1) so that along the Dirichlet boundary  $\Gamma_{aD}$  the state variable is given and the right hand side is searched for.

### Neumann boundary condition

Prescribing a secondary variable, either the normal displacement  $u_{a,n}$  or the normal velocity  $v_{a,n}$  is given at a Neumann boundary  $\Gamma_{aN}$  of an acoustic fluid. In the case of harmonic oscillations, those variables can be transferred into each other via  $v_{a,n} = i\omega u_{a,n}$ . Setting

$u_{a,n}$  respectively  $v_{a,n}$  to zero corresponds to a fully reflecting boundary. We can express the Neumann boundary condition as

$$\frac{1}{\rho_a \omega^2} \frac{\partial p_a}{\partial \mathbf{n}_a} - u_{a,n} = 0 \quad \text{on } \Gamma_{aN}. \quad (2.18)$$

Introducing equation (2.18) in the boundary representation in equation (2.13) we can find the right hand side contribution mapping the Neumann boundary condition:

$$\mathbf{f}_{a_e} = \int_{\Gamma_{a_e}} \omega^2 \mathbf{N}_{p\Gamma}^\top u_{a,n} \, d\Gamma_{a_e}. \quad (2.19)$$

$\Gamma_{a_e}$  is the one-dimensional boundary of a two-dimensional acoustic element.

### Robin boundary condition

A simple way to model radiating boundaries is the Robin boundary condition. While being rather easy to implement, the Robin boundary condition has the drawback that it is only able to depict a very simple radiation pattern. The waves leaving the acoustic domain have to impinge normally on the Robin boundary. Otherwise, more complex reflection patterns will disturb the simulation outcome.

Along a Robin boundary, the normal impedance  $Z_a$  is set to the value  $Z_\Gamma$ :

$$Z_a - Z_\Gamma = 0 \quad \text{on } \Gamma_{aR}, \quad (2.20)$$

with

$$Z_a = -i\omega\rho_a p_a \left( \frac{\partial p_a}{\partial \mathbf{n}_a} \right)^{-1}. \quad (2.21)$$

Modelling a radiating boundary, the impedance at the Robin boundary condition is set equal to the impedance of the acoustic domain:  $Z_\Gamma = \sqrt{\rho_a E_a}$ . Inserting the relations above in the boundary representation in equation (2.13), we can model the Robin boundary condition via a contribution to the damping matrix:

$$\mathbf{C}_{a_e} = \int_{\Gamma_{a_e}} \frac{1}{\sqrt{\rho_a E_a}} \mathbf{N}_{p\Gamma}^\top \mathbf{N}_{p\Gamma} \, d\Gamma_{a_e}. \quad (2.22)$$

As the Robin boundary condition goes along with strong modelling limits and only provides a realistic representation of free radiation within these limits, other approaches are needed

cope with modelling more complex radiation patterns. Within the scope of this work, a suitable approach which also maps a possible change in the shape of the radiating boundary is proposed in section 4.4. [Ochmann et al 2017] gives an overview over existing methods for modelling (partially) unlimited acoustic fluid domains. One option are perfectly matched layers [Harari et al 2000; Shirron and Giddings 2006]. Here, a secondary domain adjoins the acoustic fluid. Within this secondary domain the incoming waves are absorbed without reflecting parts back into the primary fluid domain.

## 2.5 Linear elastic solid

When modelling structural elements within the framework of this thesis, linear elastic and isotropic material behaviour is assumed. Under this assumption the Lamé equation describes the dynamic characteristics of the solid in the frequency domain in form of a partial differential equation:

$$(\lambda_e + \mu_e) \nabla \operatorname{div} \mathbf{u}_e + \mu_e \nabla^2 \mathbf{u}_e + \omega^2 \rho_e \mathbf{u}_e = \mathbf{0}, \quad (2.23)$$

with the solid density  $\rho_e$  and displacement vector  $\mathbf{u}_e$ .  $\lambda_e$  and  $\mu_e$  are the first and second Lamé parameter corresponding to the solid and are related to the solid's Young's modulus  $E_e$  and Poisson's ratio  $\nu_e$  via

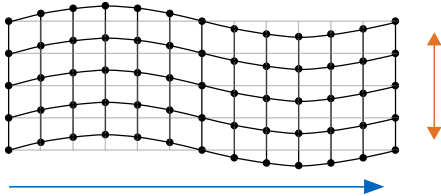
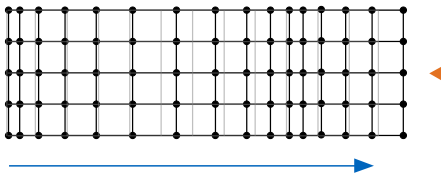
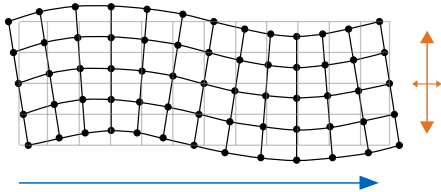
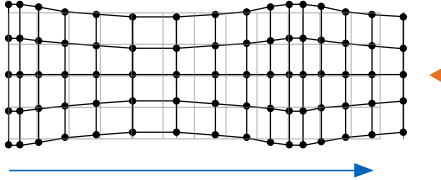
$$\lambda_e = \frac{E_e \nu_e}{(1 + \nu_e)(1 - 2\nu_e)}, \quad (2.24)$$

$$\mu_e = \frac{E_e}{2(1 + \nu_e)}. \quad (2.25)$$

The index  $\square_e$  expresses the affiliation of a variable to a linear elastic solid. A derivation of equation (2.23) can be found for example in [Hackenberg 2016].

Unlike acoustic fluids, solids can also transmit shear forces. As a consequence, besides longitudinal waves also shear waves emerge within unlimited solid domains. While for longitudinal waves the oscillation takes place in the propagation direction, for shear waves the oscillation is perpendicular to the direction in which the wave propagates. In the case of spatially limited structures like plates and beams, the relevant wave types are quasi-longitudinal waves and dispersive bending waves. Transverse contractions due to longitudinal strain differentiate quasi longitudinal waves from longitudinal waves. In bending waves the particles oscillate perpendicular to the propagation direction and undergo a rotation at the same time. In contrast to the other wave types, the wave speed of bending waves is frequency

dependent (dispersive). The partial differential equation used for the model defines the assumptions made for the propagation pattern of the bending waves. While the Kirchhoff and also the Euler-Bernoulli theory neglect shear deformation, shear deformation is mapped by the Reissner-Mindlin and the Timoshenko theory [Zienkiewicz et al 2005; Spura 2019]. Table 2.1 contains the wave speeds and propagation patterns corresponding to the different wave types in elastic solids. According to [Cremer and Heckl 2013] we need to differentiate between plates that are spatially limited in one direction and beams being spatially limited in two directions for bending and quasi-longitudinal waves.  $h$  is the height of the spatially limited structure and  $I_e$  is the second moment of inertia corresponding to a beam's cross section.

<b>Shear wave</b>	$c_S = \sqrt{\frac{\mu_e}{\rho_e}}$	
<b>Longitudinal wave</b>	$c_L = \sqrt{\frac{(\lambda_e + 2\mu_e)}{\rho_e}}$	
<b>Bending wave</b> <sup>1</sup>	$c_{B,plate} = \sqrt[4]{\omega^2 \frac{E_e h^3}{12 \rho_e h (1 - \nu_e^2)}}$ $c_{B,beam} = \sqrt[4]{\omega^2 \frac{E_e I_e}{\rho_e h}}$	
<b>Quasi-longitudinal wave</b>	$c_{Q,plate} = \sqrt{\frac{E_e}{\rho_e (1 - \nu_e^2)}}$ $c_{Q,beam} = \sqrt{\frac{E_e}{\rho_e}}$	

**Table 2.1:** Wave speeds and propagation patterns corresponding to wave types emerging in elastic solids; blue arrows mark propagation direction, orange arrows mark respective direction of oscillation.

<sup>1</sup>The given relations result from the Kirchhoff respectively the Euler-Bernoulli theory and is valid under consideration of the corresponding model limits.

### 2.5.1 Finite Element model for the structural domain

Same as for the acoustic fluid, we need the weak form of equation (2.23) to derive the elemental matrices corresponding to the solid. It can be easily obtained applying the principle of virtual work on a reference volume. The virtual work is composed of the virtual work corresponding to the internal forces ( $\delta W_I$ ), inertia effects ( $\delta W_T$ ) and external forces ( $\delta W_E$ ) and shall be zero for a structure that is in equilibrium. The virtual work formulated according to the coordinate directions considered in the model is given by

$$\underbrace{\int_{\Omega_e} \boldsymbol{\sigma}_e : \delta \boldsymbol{\varepsilon}_e \, d\Omega_e}_{\delta W_I} - \underbrace{\int_{\Omega_e} \omega^2 \rho_e \mathbf{u}_e \times \delta \mathbf{u}_e \, d\Omega_e}_{\delta W_T} - \underbrace{\int_{\Gamma_e} \boldsymbol{\sigma}_e \mathbf{n}_e \times \delta \mathbf{u}_e \, d\Gamma_e}_{\delta W_E} = \mathbf{0}. \quad (2.26)$$

For the two-dimensional problems considered in the context of this work, one equation results for a virtual displacement along the  $x$ -axis as well as a second equation for a virtual displacement along the  $y$ -axis, with

$$\boldsymbol{\sigma}_e : \delta \boldsymbol{\varepsilon}_e = \sum_{ij} \sigma_{e_{ij}} \delta \varepsilon_{e_{ij}}. \quad (2.27)$$

$\boldsymbol{\sigma}_e$  and  $\boldsymbol{\varepsilon}_e$  correspond to the stress and strain tensor within the structural domain;  $\mathbf{n}_e$  is defined as normal vector pointing outwards of the elastic domain. The state variable corresponding to the solid is the displacement vector  $\mathbf{u}_e$ , resulting in two DOFs per node for two-dimensional problems and three DOFs per node for three-dimensional problems. The component wise multiplication of two vector fields  $\mathbf{a}$  and  $\mathbf{b}$  is denoted by  $\mathbf{a} \times \mathbf{b}$  and defined by  $\mathbf{a} \times \mathbf{b} = \mathbf{c}$  with  $c_i = a_i b_i$ .

Based on equation (2.26), we can find the elemental matrices corresponding to a linear elastic solid according to [Zienkiewicz et al 2005]:

$$\mathbf{K}_{e_e} = \int_{\Omega_{e_e}} \mathbf{B}^\top \mathbf{E}_e \mathbf{B} \, d\Omega_{e_e}, \quad (2.28)$$

$$\mathbf{M}_{e_e} = \int_{\Omega_{e_e}} \rho_e \mathbf{N}_{u\Omega}^\top \mathbf{N}_{u\Omega} \, d\Omega_{e_e}. \quad (2.29)$$

$\Omega_{e_e}$  is the area occupied by a two-dimensional structural element. Using the bilinear shape functions defined in equation (2.3), we can deduce the strain-displacement matrix  $\mathbf{B}$  for a

two-dimensional element with four nodes:

$$\mathbf{B} = \begin{bmatrix} \frac{\partial N_1}{\partial x} & 0 & \frac{\partial N_2}{\partial x} & 0 & \frac{\partial N_3}{\partial x} & 0 & \frac{\partial N_4}{\partial x} & 0 \\ 0 & \frac{\partial N_1}{\partial y} & 0 & \frac{\partial N_2}{\partial y} & 0 & \frac{\partial N_3}{\partial y} & 0 & \frac{\partial N_4}{\partial y} \\ \frac{\partial N_1}{\partial y} & \frac{\partial N_1}{\partial x} & \frac{\partial N_2}{\partial y} & \frac{\partial N_2}{\partial x} & \frac{\partial N_3}{\partial y} & \frac{\partial N_3}{\partial x} & \frac{\partial N_4}{\partial y} & \frac{\partial N_4}{\partial x} \end{bmatrix}. \quad (2.30)$$

For two-dimensional problems, we need to make an assumption concerning the third dimension. Modelling thin structures like beams, the stresses perpendicular to the two-dimensional plane are set to zero. This assumption is called plane stress. If the extension of the structure perpendicular to the modelled plane is comparably large, we can assume plane strain meaning that the strains corresponding to this direction vanish. Depending on whether the structure is in plane stress or plane strain, we can define the elasticity matrix according to [Zienkiewicz et al 2005]:

$$\mathbf{E}_e = \frac{E_e}{(1 - \nu^2)} \begin{bmatrix} 1 & \nu & 0 \\ \nu & 1 & 0 \\ 0 & 0 & \frac{1-\nu}{2} \end{bmatrix} \quad (2.31)$$

for plane stress and

$$\mathbf{E}_e = \frac{E_e}{(1 + \nu)(1 - 2\nu)} \begin{bmatrix} 1 - \nu & \nu & 0 \\ \nu & 1 - \nu & 0 \\ 0 & 0 & \frac{1-2\nu}{2} \end{bmatrix} \quad (2.32)$$

for plane strain.

## 2.5.2 Boundary conditions of the structural domain

For solids, we differentiate between Dirichlet and Neumann boundary conditions. A Dirichlet boundary condition prescribes the displacement  $\mathbf{u}_e$  to a certain value  $\mathbf{u}_\Gamma$  on the solid boundary  $\Gamma_{eD}$ :

$$\mathbf{u}_e - \mathbf{u}_\Gamma = 0 \quad \text{on } \Gamma_{eD}. \quad (2.33)$$

Supports are mapped by setting the respective displacement DOF to zero ( $u_{\Gamma_i} = 0$ ). Similarly to the acoustic fluid, we can employ this boundary condition by restructuring equation (2.1).

The solids Neumann boundary condition can be expressed by

$$\boldsymbol{\sigma}_e - \boldsymbol{\sigma}_\Gamma = 0 \quad \text{on } \Gamma_{eN}, \quad (2.34)$$

where  $\boldsymbol{\sigma}_\Gamma$  is the prescribed value of the stresses  $\boldsymbol{\sigma}_e$  along  $\Gamma_{eN}$ . Substituting equation (2.34) into the surface integral in equation (2.26), we can compute the right hand side contributions at the Neumann boundary of the structural domain according to:

$$\mathbf{f}_{e_e} = \int_{\Gamma_{e_e}} \mathbf{N}_{u\Gamma}^\top \boldsymbol{\sigma}_\Gamma \mathbf{n}_e \, d\Gamma_{e_e} \quad (2.35)$$

$\Gamma_{e_e}$  is the one-dimensional boundary of a two-dimensional structural element.  $\mathbf{f}_{e_e}$  corresponds to the load vector on the element's boundary. The individual entries are the nodal loads in the direction of the two coordinate axes. Accordingly,  $\mathbf{f}_{e_e}$  can also be defined directly by prescribing the nodal loads instead of the stress value  $\boldsymbol{\sigma}_\Gamma$  along the Neumann boundary. A free edge corresponds to a Neumann boundary where the stress (respectively nodal load) value is set to zero.

## 2.6 Coupling between solid and fluid domain

In order to describe the dynamic behaviour of systems consisting of both fluid and solid domains in a FE model, the coupling of these components must be represented. The complexity of the coupling model depends on the respective application case. For example, if the wind effect on a building is to be modelled, it is often sufficient to model the wind as an external loading on the building. An influence of the building deflections on the wind effect can be neglected under given circumstances. For vibroacoustic problems, however, this consideration is insufficient. Here, both the effects of pressure fluctuations in the fluid on the dynamic processes of the structure and the influence of structural vibrations on the pressure distribution in the fluid must be taken into account.

Accounting for the mutual coupling of the two constituents results in coupling terms in the mass and stiffness matrix of the coupled system. Deriving those coupling terms, we need to ensure that the equilibrium of forces is fulfilled along the coupling interface  $\Gamma_{ae}$ :

$$\boldsymbol{\sigma}_e \mathbf{n}_a + p_a \mathbf{n}_a = \mathbf{0} \quad \text{on } \Gamma_{ae}. \quad (2.36)$$

Besides that, the continuity of displacements has to be enforced along  $\Gamma_{ae}$ . For steady state



harmonic oscillations the continuity equation is given by

$$\mathbf{u}_e \cdot \mathbf{n}_a - \frac{1}{\rho_a \omega^2} \frac{\partial p_a}{\partial \mathbf{n}_a} = 0 \quad \text{on } \Gamma_{ae}. \quad (2.37)$$

Next, we formulate the boundary integral along the coupling interface  $\Gamma_{ae}$ . As the coupling interface is a common boundary of the acoustic fluid and the solid, we need to consider the boundary integrals from equations (2.13) and (2.26). Inserting (2.36) and (2.37) leads to:

$$\begin{aligned} I_{\Gamma_{ae},1} &= - \int_{\Gamma_{ae}} \frac{1}{\rho_a} \frac{\partial p_a}{\partial \mathbf{n}_a} \delta p_a d\Gamma_{ae} = - \int_{\Gamma_{ae}} \omega^2 \mathbf{u}_e \cdot \mathbf{n}_a \delta p_a d\Gamma_{ae}, \\ I_{\Gamma_{ae},2} &= + \int_{\Gamma_{ae}} \boldsymbol{\sigma}_e \mathbf{n}_a \times \delta \mathbf{u}_e d\Gamma_{ae} = - \int_{\Gamma_{ae}} p_a \mathbf{n}_a \times \delta \mathbf{u}_e d\Gamma_{ae}. \end{aligned}$$

The sign change of the first boundary integral, which corresponds to the solid, results from the deviating definition of the direction of the normal vector.

Though mathematically inconsistent, as common in the reference literature, the individual boundary integrals are summarized in one term for the sake of brevity:

$$I_{\Gamma_{ae}} = - \underbrace{\int_{\Gamma_{ae}} \omega^2 \mathbf{u}_e \cdot \mathbf{n}_a \delta p_a d\Gamma_{ae}}_{\text{scalar contribution}} - \underbrace{\int_{\Gamma_{ae}} p_a \mathbf{n}_a \times \delta \mathbf{u}_e d\Gamma_{ae}}_{\text{vector contribution}}. \quad (2.38)$$

It should be noted that the boundary term shown above cannot be simplified further, since it is composed of a scalar and a vector contribution quantity.

Approximating the primary variables and their admissible variations by the shape functions introduced in equation (2.5), the coupling contributions to the mass and stiffness matrix can be derived:

$$\mathbf{K}_{ae_e} = - \int_{\Gamma_{ae_e}} \mathbf{N}_{u\Gamma}^\top \mathbf{n}_a \mathbf{N}_{p\Gamma} d\Gamma_{ae_e} \quad (2.39)$$

$$\mathbf{M}_{ae_e} = -\mathbf{K}_{ae_e}^\top. \quad (2.40)$$

With  $\Gamma_{ae_e}$  being the coupling interface on element level.

To conclude this section, we will take a closer look at equation (2.1). For a coupled system of acoustic fluid and solid, we can split equation (2.1) up into the following components:

$$\left( \begin{bmatrix} \mathbf{K}_a & \mathbf{0} \\ \mathbf{K}_{ae} & \mathbf{K}_e \end{bmatrix} + i\omega \begin{bmatrix} \mathbf{C}_a & \mathbf{0} \\ \mathbf{0} & \mathbf{0} \end{bmatrix} - \omega^2 \begin{bmatrix} \mathbf{M}_a & \mathbf{M}_{ae} \\ \mathbf{0} & \mathbf{M}_e \end{bmatrix} \right) \begin{bmatrix} \mathbf{p}_a \\ \mathbf{u}_e \end{bmatrix} = \begin{bmatrix} \mathbf{f}_a \\ \mathbf{f}_e \end{bmatrix} \quad (2.41)$$

With the indices  $\square_a$  and  $\square_e$  denoting terms related to the fluid, respectively the solid. The index  $\square_{ae}$  marks the components responsible for the coupling of the two constituents. The individual components in equation (2.41) are obtained by assembling the elemental, boundary and interface contributions introduced previously in this chapter. The assembling process is carried out in such a way that the continuity of the state variables at the transitions between the individual elements is fulfilled.

In the scope of this thesis undamped wave propagation in the acoustic fluid is assumed. Therefore, the only part in the damping matrix belonging to the acoustic fluid results from the Robin boundary condition. One way to represent damping within the structure is to use a hysteretic proportional damping model. It can be implemented via a complex Young's modulus:

$$E_{\eta,e} = E_e(1 + i\eta_e), \quad (2.42)$$

with  $\eta_e$  as damping coefficient for the structural domain. Thereby the introduction of the complex Young's modulus  $E_{\eta,e}$  has the consequence that also dependent quantities such as the two Lamé parameters become complex. Modelling the damping in the linear elastic solid via a complex Young's modulus, damping is included in the (thus complex valued) stiffness matrix and there are no corresponding entries in the damping matrix. [Adhikari 2001] gives an overview over other damping models employed for structural vibration in literature.

## 2.7 Conclusion

This chapter distinguishes the FEM from other numerical solution strategies and explains its basic principle using the example of two-dimensional elements with four nodes. The element matrices are derived for acoustic fluid and linear elastic structural elements. In addition, it is discussed how different boundary conditions can be considered in a FE implementation. Finally, it is described how the mutual coupling between acoustic fluid and linear elastic solid can be represented. Based on the content of this chapter, it is possible to map complex vibroacoustic systems consisting of fluid and structural components with a FEM model.

## 3 Characterization of porous materials

### 3.1 Introduction

The term porous material characterizes a heterogeneous structure consisting of at least two phases: p.e. a solid frame and an interstitial fluid. In the context of acoustics the fluid phase is the air and we assume that the pore framework is fully saturated and that the solid frame behaves linearly elastic. Figure 3.1 (left) shows the structure of a two-phase porous material.

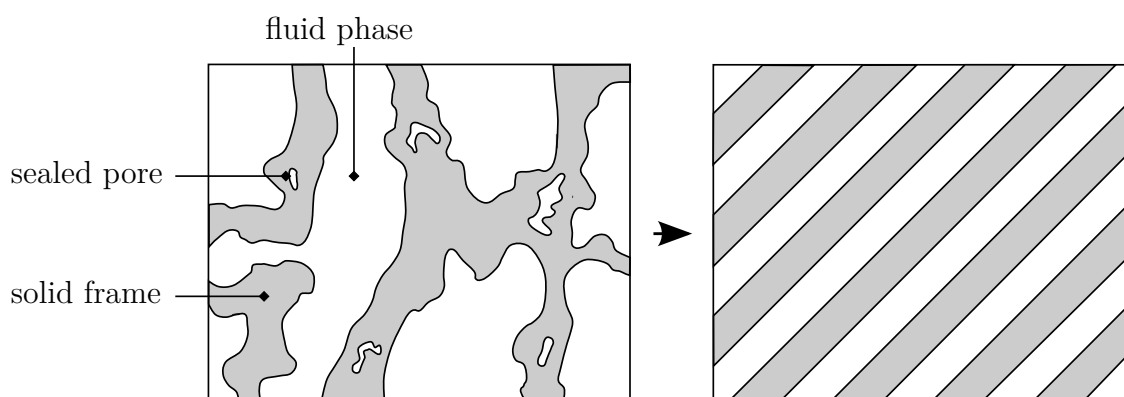


**Figure 3.1:** Porous domain modelled as statistical multiphase continuum.

Due to their favourable dissipation properties in the mid and high frequency range, porous materials are often used as noise reduction measures. The dissipation in porous media is mainly induced by frictional effects between the two phases and periodic temperature fluctuations in the fluid phase [Cremer and Müller 1982; Buchschmid 2011]. The efficiency of porous absorbers strongly depends on their dynamic properties and their geometry. For instance, the flow resistance should be large enough to introduce dissipation effects, but shouldn't be too large so that the acoustic sound waves enter the absorber rather than being reflected [Fuchs 2010]. Furthermore, the thickness of a rigidly supported porous absorber

has to be equal to or greater than about one quarter of the wavelength in the adjacent sound field in order to damp the excitation efficiently [Deckers et al 2016].

In order to analyse the dissipation mechanisms and dispersion characteristics of porous (meta-)materials, one has to describe the behaviour of the porous domain analytically. Thereby it is important to model the effects of the fluid-structure interaction and wave propagation in the porous medium properly. [Schanz 2001] identifies three key mechanisms characterizing the fluid-structure interaction in porous media: Increasing the pore pressure leads to a deflection of the solid phase; deforming the solid phase leads to a modification of the pore pressure if the fluid cannot escape the pore framework; energy dissipation is introduced by relative motion between solid and fluid phase. Due to the occurring fluid-structure interaction the wave propagation in porous media differs from the wave propagation in homogeneous domains. We can observe three different wave types, being one shear and two compressional waves, whose characteristics depend on the type of coupling between solid and fluid phase [Hörilin 2004]. Compared to that, one shear wave and one compressional wave exist in infinite homogeneous solids, and only one compressional waves emerges in acoustic fluids.

In theory the behaviour of porous materials could be mapped using the derivations in chapter 2 modelling the constituents separately on the area they occupy and coupling them via appropriate coupling conditions. This would require accurate modelling of the geometry of the pore framework coming up with the disadvantage that a very fine discretisation is needed in the case of a numerical implementation using the FEM. Moreover, in very few applications the exact geometry of the pore framework is known. Instead, the material distribution is usually expressed in terms of the proportion of pores in the total volume. Thus, in practice there are more efficient modelling approaches. The literature refers to two major approaches providing a mathematical description of porous media: the Theory of Porous Media (TPM) and the Biot Theory (BT) [de Boer 2000]. As visualized by figure 3.1, both theories model porous media as statistical multiphase continua [Schanz 2003; Ehlers 1996]. Each location within the porous domain is assumed to be simultaneously occupied by fluid and solid phase. The interaction between the constituents is considered as statistical volume interaction modelled by theory specific parameters [Hörilin 2004]. The ratio of the volume fractions of the two constituents is introduced by the porosity  $\phi$ . It is defined as  $\phi = \frac{V_f}{V_t}$ , where  $V_f$  is the volume fraction occupied by the fluid phase and  $V_t$  is the total volume corresponding to the porous domain. As illustrated in Fig. 3.1, one usually distinguishes between the fluid in the interconnected and the sealed pores. Since the fluid in the sealed pores is not able to move independently from the solid frame, it is assigned to the solid phase. Consequently, the fluid phase only includes the fluid in the interconnected or open

pores. The description as statistical multiphase continuum is evident for porous absorbers as those can hardly be produced with exact a priori defined shape of the solid frame. It is valid since the wavelengths in porous media are significantly larger than the pore dimensions [Jonckheere et al 2013]. Furthermore, at scales larger than the size of the pores, the material is assumed to be homogeneous and isotropic [Mechel 2008], meaning that the pores are distributed equally over the porous domain.

The TPM is based on concepts of continuum mechanics and thermodynamics and dates back to [Fillunger 1913]. The BT on the other hand is empirically based [Schanz 2003]. It dates back to [von Terzaghi 1923] and was enhanced in [Biot 1955, 1956b,a]. In case of incompressible constituents one can find a compliance of both theories [Schanz 2003]. During the last decades the original BT was adapted for vibroacoustic applications. In order to take into account frequency dependent thermal and viscous effects, the thermal characteristic length [Johnson et al 1986, 1987] and the viscous characteristic length [Champoux and Allard 1991] were introduced to the parameter set. The so called Johnson–Champoux–Allard model (JCAM) [Allard and Atalla 2009] is state of the art for vibroacoustic applications and will be used in the context of this thesis. [Deckers et al 2015] reviews the JCAM together with other commonly used models for porous domains and gives an overview over numerical modelling strategies applicable for mapping porous media.

Following the introduction, this chapter presents the JCAM. Different options of implementing the JCAM into a FEM analysis are presented and compared on simple numerical examples.

## 3.2 Johnson-Champoux-Allard Model for porous materials

The content of this section is based on [Allard and Atalla 2009], which can be considered as reference source for the JCAM. Using the JCAM, the porous domain is characterized by a certain set of parameters. Table 3.1 sums up those parameters and assigns them to the solid frame, the fluid phase and their interaction (labelled as porous domain). The model assumes a linear elastic pore framework, but can also be adapted to represent a rigid or limp solid phase.

In order to describe the complex behaviour of the porous multiphase continuum, the JCAM introduces the equivalent bulk modulus of the fluid phase  $\tilde{K}_f$  and the viscous drag  $\tilde{b}$ , which

<b>Solid frame</b>	$\rho_s$	$\left[\frac{kg}{m^3}\right]$	Density
	$\lambda_s, \mu_s$	$[Pa]$	Lamé coefficients
	$\eta_s$	$[-]$	Damping ratio
<b>Fluid phase</b>	$\rho_f$	$\left[\frac{kg}{m^3}\right]$	Density
	$\eta$	$\left[\frac{Ns}{m^2}\right]$	Viscosity
	$P_0$	$[Pa]$	Standard pressure
	$\gamma$	$[-]$	Heat capacity
	$Pr$	$[-]$	Prandtl number
<b>Porous domain</b>	$\Phi$	$[-]$	Porosity
	$\alpha_\infty$	$[-]$	Tortuosity
	$\sigma$	$\left[\frac{Ns}{m^4}\right]$	Flow resistivity
	$\Lambda$	$[m]$	Viscous length
	$\Lambda'$	$[m]$	Thermal length

**Table 3.1:** Material parameters corresponding to porous domain.

are both complex and frequency dependent:

$$\tilde{K}_f = \frac{\gamma P_0}{\gamma - (\gamma - 1) \left[ 1 + \frac{8\eta}{i\omega Pr \Lambda'^2 \rho_f} \left( 1 + \frac{i\omega Pr \Lambda'^2 \rho_f}{16\eta} \right)^{\frac{1}{2}} \right]^{-1}}, \quad (3.1)$$

$$\tilde{b} = \sigma \Phi^2 \left[ 1 + \frac{4i\omega \alpha_\infty^2 \eta \rho_f}{\sigma^2 \Lambda^2 \Phi^2} \right]^{\frac{1}{2}}. \quad (3.2)$$

In the context of this thesis  $\tilde{\square}$  marks frequency dependent quantities.

According to [Mechel 2008], the wave speeds  $c_{P_{1,2}}$  of the two compressional waves and  $c_S$  of the shear wave propagating in porous materials are given as

$$c_{P_{1,2}} = \left[ \frac{2\mathbf{a}}{\omega \left( \mathbf{b} \pm \sqrt{\mathbf{b}^2 - 4\mathbf{a}\mathbf{c}} \right)} \right]^{\frac{1}{2}}, \quad (3.3)$$

$$c_S = \sqrt{\frac{\tilde{\mu} \tilde{\rho}_f}{\omega \mathbf{c}}}, \quad (3.4)$$

with

$$\mathbf{a} = \tilde{P}\tilde{R} - \tilde{Q}^2, \quad (3.5)$$

$$\mathbf{b} = \tilde{\rho}_s\tilde{R} + \tilde{\rho}_f\tilde{P} - 2\tilde{\rho}_{sf}\tilde{Q}, \quad (3.6)$$

$$\mathbf{c} = \tilde{\rho}_s\tilde{\rho}_f - \tilde{\rho}_{sf}^2, \quad (3.7)$$

and

$$\tilde{A} = \lambda_{\eta,s} + \frac{(1-\phi)^2}{\phi}\tilde{K}_f, \quad (3.8)$$

$$\tilde{P} = \tilde{A} + 2\mu_{\eta,s}, \quad (3.9)$$

$$\tilde{Q} = (1-\phi)\tilde{K}_f, \quad (3.10)$$

$$\tilde{R} = \phi\tilde{K}_f. \quad (3.11)$$

The complex Lamé coefficients considering the damping of the solid frame are given as

$$\lambda_{\eta,s} = \lambda_s(1 + i\eta_s), \quad (3.12)$$

$$\mu_{\eta,s} = \mu_s(1 + i\eta_s). \quad (3.13)$$

The equivalent densities contained in the above equations map viscous and inertial effects within the porous domain and are defined as follows:

$$\tilde{\rho}_{sf} = \phi\rho_f(1 - \alpha_\infty) + i\frac{\tilde{b}}{\omega}, \quad (3.14)$$

$$\tilde{\rho}_s = (1 - \phi)\rho_s - \tilde{\rho}_{sf}, \quad (3.15)$$

$$\tilde{\rho}_f = \phi\rho_f - \tilde{\rho}_{sf}. \quad (3.16)$$

By computing the wavelengths in the porous medium, the discretisation required for a FEM model can be estimated. [Dauchez et al 2001] shows that for one-dimensional applications the same mesh criteria apply for porous media as for single-phase materials. It is found that, using linear shape functions, reliable results can be obtained with six elements per wavelength. For multidimensional problems, it is observed that porous elements generally converge more slowly than acoustic or elastic elements and require a higher number of nodes per wavelength. A general criterion of how many nodes per wavelength are required could not be found.

### 3.3 Finite Element model for porous materials

In addition to the theory for the description of the porous domain, one has to choose the set of unknowns for the underlying system of differential equations. Different options and their application dependent benefits and drawbacks are specified in the following. The respective systems of differential equations are presented in their weak form to be processed for a solution with the FEM. As in chapter 2, the elemental solutions and coupling terms are derived for a two-dimensional system that is meshed using quadrilateral elements with four nodes. Solutions for other element types and three-dimensional considerations can be set up analogously.

#### 3.3.1 Classical displacement based formulation

The most classical version of the JCAM is the displacement based formulation (or classical formulation). All expressions that refer exclusively to this formulation are marked by the superscript  $\square^c$ . The dynamic behaviour of the porous domain is displayed by the displacements of the solid phase  $\mathbf{u}_s$  and the fluid phase  $\mathbf{u}_f$ . The pore pressure in the fluid domain can be post-processed from these parameters. The displacement based formulation leads to four DOFs per node for two-dimensional and to six DOFs for three-dimensional FEM-applications.

Equations (3.17) display the equation system characterizing the porous domain in the classical formulation:

$$\operatorname{div} \boldsymbol{\sigma}_s + \omega^2 (\tilde{\rho}_s \mathbf{u}_s + \tilde{\rho}_{sf} \mathbf{u}_f) = \mathbf{0}, \quad (3.17a)$$

$$\operatorname{div} \boldsymbol{\sigma}_f + \omega^2 (\tilde{\rho}_{sf} \mathbf{u}_s + \tilde{\rho}_f \mathbf{u}_f) = \mathbf{0}. \quad (3.17b)$$

The equation system is formulated in the frequency domain with  $\omega$  as circular frequency.  $\boldsymbol{\sigma}_s$  and  $\boldsymbol{\sigma}_f$  are the stresses in the solid and fluid phase. The stresses in the fluid phase are related to the pore pressure  $p_f$  via

$$\boldsymbol{\sigma}_f = -\phi p_f \mathbf{I}. \quad (3.18)$$

$\mathbf{I}$  is the identity matrix corresponding to the dimensionality of the problem. Compared to the stresses in the solid, the fluid stresses do not have shear components and the normal stresses (in this case principal stresses) are equal.



A FE formulation based on the classical formulation of the BT was first introduced by [Kang and Bolton 1995]. Here, also the coupling conditions of a porous domain and an acoustic fluid were established. Corresponding formulations for the JCAM are given in [Allard and Atalla 2009] or [Rumpler 2012]. Equations (3.19) show the weak form of equations (3.17) from which the element matrices can be derived:

$$\int_{\Omega_p} \left( \boldsymbol{\sigma}_s : \delta \boldsymbol{\varepsilon}_s - \omega^2 \tilde{\rho}_s \mathbf{u}_s \times \delta \mathbf{u}_s - \omega^2 \tilde{\rho}_{sf} \mathbf{u}_f \times \delta \mathbf{u}_s \right) d\Omega_p - \int_{\Gamma_p} \boldsymbol{\sigma}_s \mathbf{n}_p \times \delta \mathbf{u}_s d\Gamma_p = \mathbf{0}, \quad (3.19a)$$

$$\int_{\Omega_p} \left( \boldsymbol{\sigma}_f : \delta \boldsymbol{\varepsilon}_f - \omega^2 \tilde{\rho}_f \mathbf{u}_f \times \delta \mathbf{u}_f - \omega^2 \tilde{\rho}_{sf} \mathbf{u}_s \times \delta \mathbf{u}_f \right) d\Omega_p - \int_{\Gamma_p} \boldsymbol{\sigma}_f \mathbf{n}_p \times \delta \mathbf{u}_f d\Gamma_p = \mathbf{0}. \quad (3.19b)$$

$\boldsymbol{\varepsilon}_s$  and  $\boldsymbol{\varepsilon}_f$  are the strains in the solid, respectively the fluid phase and  $\mathbf{n}_p$  is the normal vector pointing outwards of the porous domain.

Approximating both the solid and fluid displacements by the shape functions introduced in section 2.2.2, we can find the elemental stiffness and mass matrix corresponding to the displacement based formulation in the reference frame of elemental coordinates:

$$\tilde{\mathbf{K}}_{p_e}^c = \begin{bmatrix} \tilde{\mathbf{K}}_{s_e}^c & \tilde{\mathbf{K}}_{sf_e}^c \\ \tilde{\mathbf{K}}_{sf_e}^c & \tilde{\mathbf{K}}_{f_e}^c \end{bmatrix}, \quad (3.20)$$

$$\tilde{\mathbf{M}}_{p_e}^c = \begin{bmatrix} \tilde{\mathbf{M}}_{s_e}^c & \tilde{\mathbf{M}}_{sf_e}^c \\ \tilde{\mathbf{M}}_{sf_e}^c & \tilde{\mathbf{M}}_{f_e}^c \end{bmatrix}. \quad (3.21)$$

The individual submatrices are obtained as follows:

$$\tilde{\mathbf{K}}_{s_e}^c = \int_{\Omega_{p_e}} \mathbf{B}^\top \tilde{\mathbf{E}}_s \mathbf{B} d\Omega_{p_e}, \quad (3.22)$$

$$\tilde{\mathbf{K}}_{f_e}^c = \int_{\Omega_{p_e}} \mathbf{B}^\top \tilde{\mathbf{E}}_f \mathbf{B} d\Omega_{p_e}, \quad (3.23)$$

$$\tilde{\mathbf{K}}_{sf_e}^c = \int_{\Omega_{p_e}} \mathbf{B}^\top \tilde{\mathbf{E}}_{sf} \mathbf{B} d\Omega_{p_e}, \quad (3.24)$$

$$\tilde{\mathbf{M}}_{s_e}^c = \int_{\Omega_{p_e}} \tilde{\rho}_s \mathbf{N}_{u\Omega}^\top \mathbf{N}_{u\Omega} d\Omega_{p_e}, \quad (3.25)$$

$$\tilde{\mathbf{M}}_{f_e}^c = \int_{\Omega_{p_e}} \tilde{\rho}_f \mathbf{N}_{u\Omega}^\top \mathbf{N}_{u\Omega} d\Omega_{p_e}, \quad (3.26)$$

$$\tilde{\mathbf{M}}_{sf_e}^c = \int_{\Omega_{p_e}} \tilde{\rho}_{sf} \mathbf{N}_{u\Omega}^\top \mathbf{N}_{u\Omega} d\Omega_{p_e}, \quad (3.27)$$

with  $\Omega_{\text{pe}}$  corresponding to the area occupied by a two-dimensional porous element and

$$\tilde{\mathbf{E}}_s = 2\mu_{\eta,s} \mathbf{E}_1 + \tilde{A} \mathbf{E}_2, \quad (3.28)$$

$$\tilde{\mathbf{E}}_f = \tilde{R} \mathbf{E}_2, \quad (3.29)$$

$$\tilde{\mathbf{E}}_{\text{sf}} = \tilde{Q} \mathbf{E}_2, \quad (3.30)$$

where

$$\mathbf{E}_1 = \begin{bmatrix} 1 & 0 & 0 \\ 0 & 1 & 0 \\ 0 & 0 & \frac{1}{2} \end{bmatrix}, \quad (3.31)$$

$$\mathbf{E}_2 = \begin{bmatrix} 1 & 1 & 0 \\ 1 & 1 & 0 \\ 0 & 0 & 0 \end{bmatrix}. \quad (3.32)$$

The strain-displacement matrix  $\mathbf{B}$  is the same as in the case of the linear elastic solid and given in equation (2.30).

At this point it should be noted that the matrices defined in equations (3.22)-(3.27) are all complex and frequency dependent. If, as intended in this thesis, a vibroacoustic system with porous components is to be investigated over a larger frequency range, the elemental matrices must be re-calculated and re-assembled for each frequency considered. To avoid the computational effort involved, [Rumpler et al 2012] express the frequency dependence via prefactors of frequency independent matrices:

$$\tilde{\mathbf{K}}_{\text{pe}}^c - \omega^2 \tilde{\mathbf{M}}_{\text{pe}}^c = \mathbf{K}_{\text{pe}}^{c,(1)} + (\tilde{K}_f - P_0) \mathbf{K}_{\text{pe}}^{c,(2)} + i\omega \tilde{b} \mathbf{C}_{\text{pe}}^c - \omega^2 \mathbf{M}_{\text{pe}}^c. \quad (3.33)$$

The individual matrices are defined as follows:

$$\mathbf{K}_{\text{pe}}^{c,(1)} = \begin{bmatrix} \int_{\Omega_{\text{pe}}} \mathbf{B}^\top \mathbf{E}_s^{(1)} \mathbf{B} \, d\Omega_{\text{pe}} & \int_{\Omega_{\text{pe}}} \mathbf{B}^\top \mathbf{E}_{\text{sf}}^{(1)} \mathbf{B} \, d\Omega_{\text{pe}} \\ \int_{\Omega_{\text{pe}}} \mathbf{B}^\top \mathbf{E}_{\text{sf}}^{(1)} \mathbf{B} \, d\Omega_{\text{pe}} & \int_{\Omega_{\text{pe}}} \mathbf{B}^\top \mathbf{E}_f^{(1)} \mathbf{B} \, d\Omega_{\text{pe}} \end{bmatrix}, \quad (3.34)$$

$$\mathbf{K}_{\text{pe}}^{c,(2)} = \begin{bmatrix} \int_{\Omega_{\text{pe}}} \mathbf{B}^\top \mathbf{E}_s^{(2)} \mathbf{B} \, d\Omega_{\text{pe}} & \int_{\Omega_{\text{pe}}} \mathbf{B}^\top \mathbf{E}_{\text{sf}}^{(2)} \mathbf{B} \, d\Omega_{\text{pe}} \\ \int_{\Omega_{\text{pe}}} \mathbf{B}^\top \mathbf{E}_{\text{sf}}^{(2)} \mathbf{B} \, d\Omega_{\text{pe}} & \int_{\Omega_{\text{pe}}} \mathbf{B}^\top \mathbf{E}_f^{(2)} \mathbf{B} \, d\Omega_{\text{pe}} \end{bmatrix}, \quad (3.35)$$

$$\mathbf{C}_{\text{P}_e}^c = \begin{bmatrix} \int_{\Omega_{\text{P}_e}} \mathbf{N}_{\text{u}\Omega}^\top \mathbf{N}_{\text{u}\Omega} \, \text{d}\Omega_{\text{P}_e} & - \int_{\Omega_{\text{P}_e}} \mathbf{N}_{\text{u}\Omega}^\top \mathbf{N}_{\text{u}\Omega} \, \text{d}\Omega_{\text{P}_e} \\ - \int_{\Omega_{\text{P}_e}} \mathbf{N}_{\text{u}\Omega}^\top \mathbf{N}_{\text{u}\Omega} \, \text{d}\Omega_{\text{P}_e} & \int_{\Omega_{\text{P}_e}} \mathbf{N}_{\text{u}\Omega}^\top \mathbf{N}_{\text{u}\Omega} \, \text{d}\Omega_{\text{P}_e} \end{bmatrix}, \quad (3.36)$$

$$\mathbf{M}_{\text{P}_e}^c = \begin{bmatrix} \int_{\Omega_{\text{P}_e}} \left( (1 - \phi) \rho_s + \phi \rho_f \alpha_\infty \right) \mathbf{N}_{\text{u}\Omega}^\top \mathbf{N}_{\text{u}\Omega} \, \text{d}\Omega_{\text{P}_e} & - \int_{\Omega_{\text{P}_e}} \phi \rho_f (\alpha_\infty - 1) \mathbf{N}_{\text{u}\Omega}^\top \mathbf{N}_{\text{u}\Omega} \, \text{d}\Omega_{\text{P}_e} \\ - \int_{\Omega_{\text{P}_e}} \phi \rho_f (\alpha_\infty - 1) \mathbf{N}_{\text{u}\Omega}^\top \mathbf{N}_{\text{u}\Omega} \, \text{d}\Omega_{\text{P}_e} & \int_{\Omega_{\text{P}_e}} \phi \rho_f \alpha_\infty \mathbf{N}_{\text{u}\Omega}^\top \mathbf{N}_{\text{u}\Omega} \, \text{d}\Omega_{\text{P}_e} \end{bmatrix}, \quad (3.37)$$

with

$$\mathbf{E}_s^{(1)} = 2\mu_{\eta,s} \mathbf{E}_1 + \left( \lambda_{\eta,s} + \frac{(1 - \phi)^2}{\phi} P_0 \right) \mathbf{E}_2, \quad (3.38)$$

$$\mathbf{E}_f^{(1)} = \phi P_0 \mathbf{E}_2, \quad (3.39)$$

$$\mathbf{E}_{\text{sf}}^{(1)} = (1 - \phi) P_0 \mathbf{E}_2, \quad (3.40)$$

$$\mathbf{E}_s^{(2)} = \frac{(1 - \phi)^2}{\phi} \mathbf{E}_2, \quad (3.41)$$

$$\mathbf{E}_f^{(2)} = \phi \mathbf{E}_2, \quad (3.42)$$

$$\mathbf{E}_{\text{sf}}^{(2)} = (1 - \phi) \mathbf{E}_2. \quad (3.43)$$

Using this approach, the individual elemental matrices need to be evaluated and assembled only once. Solely the prefactors have to be re-evaluated for each frequency. The disadvantage of the method shown is that, compared to the standard approach, more individual matrices must be set up. Furthermore, the formulation cannot be integrated into a standard FEM code easily, since here only one stiffness, mass and possibly also a damping matrix is specified for each element type.

Another option to efficiently cope with the frequency dependent parameters of the JCAM is proposed by [Panneton and Atalla 1997]. Instead of working with the parameters  $\tilde{K}_f$  and  $\tilde{b}$ , [Panneton and Atalla 1997] employ their Taylor series expansion with respect to the evolution point  $\omega = 0$ . Only the constant and linear term are included in the solution. Contributions of higher order are neglected. This leads to:

$$\tilde{K}_f^{c*} = P_0 + i\omega \frac{2P_0(\gamma - 1)}{\gamma H_1}, \quad (3.44)$$

$$\tilde{b}^{c*} = \sigma\Phi^2 + i\omega\frac{\sigma\Phi^2}{2H_2} \quad (3.45)$$

with

$$H_1 = \frac{16\eta}{P_r\Lambda'^2\rho_f}, \quad (3.46)$$

$$H_2 = \frac{\sigma^2\Lambda^2\phi^2}{4\alpha_\infty^2\eta\rho_f}. \quad (3.47)$$

[Panneton and Atalla 1997] shows that using  $\tilde{K}_f^{c*}$  and  $\tilde{b}^{c*}$  instead of  $\tilde{K}_f$  and  $\tilde{b}$  approximates the reference formulation very well for  $\frac{\omega}{H_1} \ll 1 \cap \frac{\omega}{H_2} \ll 1$ .

Substituting the parameters  $\tilde{K}_f^{c*}$  and  $\tilde{b}^{c*}$  into the approach proposed by [Rumpler et al 2012], we obtain the following formulation, which will be referred to as reduced classical formulation:

$$\tilde{\mathbf{K}}_{p_e}^c - \omega^2\tilde{\mathbf{M}}_{p_e}^c \approx \mathbf{K}_{p_e}^{c,(1)} + i\omega\mathbf{C}_{p_e}^{c*} - \omega^2\mathbf{M}_{p_e}^{c*}, \quad (3.48)$$

with

$$\mathbf{C}_{p_e}^{c*} = \frac{2P_0(\gamma-1)}{\gamma H_1} \mathbf{K}_{p_e}^{c,(2)} + \sigma\Phi^2 \mathbf{C}_{p_e}^c, \quad (3.49)$$

$$\mathbf{M}_{p_e}^{c*} = \frac{\sigma\Phi^2}{2H_2} \mathbf{C}_{p_e}^c + \mathbf{M}_{p_e}^c. \quad (3.50)$$

All matrices included in the reduced classical formulation are frequency independent. Furthermore, the formulation can be easily implemented into a standard FE code.

The simplified procedure for dealing with the frequency dependent parameters proposed in equation (3.48) is compared with the full model in section 3.5 on two different numerical examples.

### 3.3.2 Mixed displacement-pressure formulation

The mixed displacement-pressure formulation (or simply mixed formulation) of the JCAM employs the solid displacements  $\mathbf{u}_s$  and the pore pressure  $p_f$  as DOFs. Compared to the

classical formulation, this leads to a reduced number of unknowns per node and accordingly to smaller system matrices for the same mesh resolution. While two-dimensional problems involve three DOFs per node, one needs to consider four DOFs per node for three-dimensional FEM-applications. All expressions that refer exclusively to the mixed formulation are marked by the superscript  $\square^m$ .

The governing differential equations for the mixed formulation were derived by [Atalla et al 1998] who introduces

$$\nabla p_f = \frac{\omega^2}{\phi} (\tilde{\rho}_f \mathbf{u}_f + \tilde{\rho}_{sf} \mathbf{u}_s) \quad (3.51)$$

into equations (3.17). As a result we get

$$\text{div } \hat{\boldsymbol{\sigma}}_s + \omega^2 \tilde{\rho} \mathbf{u}_s + \tilde{\gamma} \nabla p_f = \mathbf{0}, \quad (3.52a)$$

$$\Delta p_f + \omega^2 \frac{\tilde{\rho}_f}{\tilde{R}} p_f - \omega^2 \frac{\tilde{\rho}_f}{\phi^2} \tilde{\gamma} \text{div } \mathbf{u}_s = 0, \quad (3.52b)$$

which no longer contains the fluid displacements  $\mathbf{u}_f$  as DOF.  $\hat{\boldsymbol{\sigma}}_s$  is the in vacuo stress tensor of the solid phase and given as

$$\hat{\boldsymbol{\sigma}}_s = \boldsymbol{\sigma}_s + \phi \frac{\tilde{Q}}{\tilde{R}} p_f \mathbf{I}. \quad (3.53)$$

The auxiliary variables  $\tilde{\rho}$  and  $\tilde{\gamma}$  introduced in equations (3.52) are defined as follows:

$$\tilde{\rho} = \tilde{\rho}_s - \frac{\tilde{\rho}_{sf}^2}{\tilde{\rho}_f}, \quad (3.54)$$

$$\tilde{\gamma} = \phi \left( \frac{\tilde{\rho}_{sf}}{\tilde{\rho}_f} - \frac{\tilde{Q}}{\tilde{R}} \right). \quad (3.55)$$

Based on equations (3.52), [Atalla et al 1998] derives the weak integral representation of the

mixed formulation:

$$\int_{\Omega_p} \left( \hat{\boldsymbol{\sigma}}_s : \delta \boldsymbol{\varepsilon}_s - \omega^2 \tilde{\rho} \mathbf{u}_s \times \delta \mathbf{u}_s - \tilde{\gamma} \nabla p_f \times \delta \mathbf{u}_s \right) d\Omega_p - \int_{\Gamma_p} \hat{\boldsymbol{\sigma}}_s \mathbf{n}_p \times \delta \mathbf{u}_s d\Gamma_p = \mathbf{0}, \quad (3.56a)$$

$$\begin{aligned} & \int_{\Omega_p} \left( \frac{\phi^2}{\tilde{\rho}_f} \nabla p_f \cdot \nabla \delta p_f - \omega^2 \frac{\phi^2}{\tilde{R}} p_f \delta p_f - \omega^2 \tilde{\gamma} \mathbf{u}_s \cdot \nabla \delta p_f \right) d\Omega_p \\ & + \int_{\Gamma_p} \left( \omega^2 \tilde{\gamma} u_{s,n} - \frac{\phi^2}{\tilde{\rho}_f} \frac{\partial p_f}{\partial \mathbf{n}_p} \right) \delta p_f d\Gamma_p = 0. \end{aligned} \quad (3.56b)$$

Introducing the shape functions for scalar and vectorial state variables given in section 2.2.2, we can formulate the elemental matrices:

$$\tilde{\mathbf{K}}_{p_e}^m = \begin{bmatrix} \mathbf{K}_{s_e}^m & \tilde{\mathbf{K}}_{s_f_e}^m \\ \mathbf{0} & \tilde{\mathbf{K}}_{f_e}^m \end{bmatrix}, \quad (3.57)$$

$$\tilde{\mathbf{M}}_{p_e}^m = \begin{bmatrix} \tilde{\mathbf{M}}_{s_e}^m & \mathbf{0} \\ \tilde{\mathbf{M}}_{s_f_e}^m & \tilde{\mathbf{M}}_{f_e}^m \end{bmatrix}, \quad (3.58)$$

$$(3.59)$$

with

$$\mathbf{K}_{s_e}^m = \int_{\Omega_{p_e}} \mathbf{B}^\top (2\mu_{\eta,s} \mathbf{E}_1 + \lambda_{\eta,s} \mathbf{E}_2) \mathbf{B} d\Omega_{p_e}, \quad (3.60)$$

$$\tilde{\mathbf{K}}_{f_e}^m = \int_{\Omega_{p_e}} \frac{\phi^2}{\tilde{\rho}_f} (\nabla \mathbf{N}_{p\Omega})^\top \nabla \mathbf{N}_{p\Omega} d\Omega_{p_e}, \quad (3.61)$$

$$\tilde{\mathbf{K}}_{s_f_e}^m = -\tilde{\mathbf{M}}_{s_f_e}^{m\top} = - \int_{\Omega_{p_e}} \tilde{\gamma} \mathbf{N}_{u\Omega}^\top (\nabla \mathbf{N}_{p\Omega}) d\Omega_{p_e}, \quad (3.62)$$

$$\tilde{\mathbf{M}}_{s_e}^m = \int_{\Omega_{p_e}} \tilde{\rho} \mathbf{N}_{u\Omega}^\top \mathbf{N}_{u\Omega} d\Omega_{p_e}, \quad (3.63)$$

$$\tilde{\mathbf{M}}_{f_e}^m = \int_{\Omega_{p_e}} \frac{\phi^2}{\tilde{R}} \mathbf{N}_{p\Omega}^\top \mathbf{N}_{p\Omega} d\Omega_{p_e}. \quad (3.64)$$

Compared to the classical formulation, the mixed formulation introduces asymmetric elemental matrices, whose storage is associated with a higher effort compared to symmetric matrices. Moreover, certain efficient solution methods for vibroacoustic systems require symmetric elemental matrices and cannot be applied here [Rumpler 2012]. These disadvantages are opposed to the advantage of a smaller number of unknowns per node.

### 3.3.3 New mixed formulation

Restructuring equations (3.56), [Atalla et al 2001] introduces an altered weak integral form of the mixed formulation, which shall be referred to as new mixed formulation in the context of this thesis:

$$\begin{aligned} & \int_{\Omega_p} \left( \hat{\boldsymbol{\sigma}}_s : \delta \boldsymbol{\varepsilon}_s - \omega^2 \tilde{\rho} \mathbf{u}_s \times \delta \mathbf{u}_s - \frac{\phi}{\tilde{\alpha}} \nabla p_f \times \delta \mathbf{u}_s - \phi \left( 1 + \frac{\tilde{Q}}{\tilde{R}} \right) (p_f \nabla \times \delta \mathbf{u}_s) \right) d\Omega_p \\ & - \int_{\Gamma_p} \boldsymbol{\sigma}_t \mathbf{n}_p \times \delta \mathbf{u}_s d\Gamma_p = \mathbf{0}, \end{aligned} \quad (3.65a)$$

$$\begin{aligned} & \int_{\Omega_p} \left( \frac{\phi^2}{\omega^2 \tilde{\rho}_f} \nabla p_f \cdot \nabla \delta p_f - \frac{\phi^2}{\tilde{R}} p_f \delta p_f - \frac{\phi}{\tilde{\alpha}} \mathbf{u}_s \cdot \nabla \delta p_f - \phi \left( 1 + \frac{\tilde{Q}}{\tilde{R}} \right) \nabla \cdot \mathbf{u}_s \delta p_f \right) d\Omega_p \\ & - \int_{\Gamma_p} \phi (\mathbf{u}_f \cdot \mathbf{n}_p - \mathbf{u}_s \cdot \mathbf{n}_p) \delta p_f d\Gamma_p = 0, \end{aligned} \quad (3.65b)$$

with

$$\frac{\phi}{\tilde{\alpha}} = \tilde{\gamma} + \phi \left( 1 + \frac{\tilde{Q}}{\tilde{R}} \right). \quad (3.66)$$

The elemental matrices according to the new mixed formulation are given as

$$\tilde{\mathbf{K}}_{p_e}^{m*} = \begin{bmatrix} \tilde{\mathbf{K}}_{s_e}^m & \tilde{\mathbf{K}}_{s_{f_e}}^{m*} \\ \mathbf{0} & \tilde{\mathbf{K}}_{f_e}^m \end{bmatrix}, \quad (3.67)$$

$$\tilde{\mathbf{M}}_{p_e}^{m*} = \begin{bmatrix} \tilde{\mathbf{M}}_{s_e}^m & \mathbf{0} \\ \tilde{\mathbf{M}}_{s_{f_e}}^{m*} & \tilde{\mathbf{M}}_{f_e}^m \end{bmatrix}, \quad (3.68)$$

with

$$\tilde{\mathbf{K}}_{s_{f_e}}^{m*} = -\tilde{\mathbf{M}}_{s_{f_e}}^{m* \top} = - \int_{\Omega_{p_e}} \left( \frac{\phi}{\tilde{\alpha}} \mathbf{N}_{u\Omega}^\top (\nabla \mathbf{N}_{p\Omega}) + \phi \left( 1 + \frac{\tilde{Q}}{\tilde{R}} \right) (\nabla^\top \mathbf{N}_{u\Omega})^\top \mathbf{N}_{p\Omega} \right) d\Omega_{p_e}. \quad (3.69)$$

Compared to the original mixed formulation (equations (3.56)), the new mixed formulation (equations (3.65)) provides simplified coupling conditions between porous and linear elastic structural domains.

### 3.3.4 Equivalent fluid model

A possibility to represent the porous medium in a simplified way is the use of an equivalent fluid model. Here, the porous medium is treated like a fluid with modified material properties. Same as for the acoustic fluid, the pressure (in this case the pore pressure) is the only DOF per node, independent of the dimensionality of the problem under consideration. The wave propagation in the porous medium is mapped only by the compressional wave in the fluid. In the modelling process, a distinction is made between whether a rigid or a limp pore framework is assumed. In addition to reducing the computational effort due to the lower number of DOFs, the equivalent fluid models can prevent numerical problems in the limiting cases of a particularly stiff or soft pore framework. [Panneton 2007] provides an overview of when and if so, which equivalent fluid model should be used.

#### Rigid frame porous media

Assuming a rigid frame porous medium can be a valid choice for metal foams or in general porous media where the solid phase has a high stiffness. The equivalent fluid model can be derived from the mixed formulation (equations (3.52)) by setting the solid displacements to zero ( $\mathbf{u}_s = \mathbf{0}$ ). As a result we obtain the following differential equation for rigid frame porous media:

$$\frac{1}{\tilde{\rho}_f} \Delta p_f + \omega^2 \frac{1}{\tilde{R}} p_f = 0. \quad (3.70)$$

The structure of this equation is the same as of the differential equation for the acoustic fluid (equation (2.12)), with more complex material parameters being used for the equivalent fluid model. The weak formulation of equation (3.70) as well as the boundary conditions for the equivalent fluid model can therefore be derived according to section 2.4.

At this point it is important to note that the equivalent fluid model in equation (3.70) is not able to model rigid body modes. If, for example, the porous material can slide freely along an edge in the application scenario, this behaviour is not reproduced and can lead to unrealistic simulation results, especially in the low frequency range.

#### Limp frame porous media

Limp frame porous media have a very soft pore structure. An example are soft fibrous layers or soft sponges. According to [Panneton 2007], we can assume that counteract to excitations



the stress field falls to zero. Introducing  $\hat{\sigma}_s = 0$  into equation (3.52), we can eliminate the solid displacements, leading to the following differential equation for limp frame porous media:

$$\left( \frac{1}{\tilde{\rho}_f} + \frac{\tilde{\gamma}^2}{\phi^2 \tilde{\rho}} \right) \Delta p_f + \omega^2 \frac{1}{\tilde{R}} p_f = 0. \quad (3.71)$$

Unlike equation (3.70), rigid body motions are also represented here. A FEM model based on equation (3.71) can be found in analogy to section 2.4.

### 3.3.5 Total displacement formulation

In order to provide a comprehensive overview of common formulations, it is necessary to also refer to a formulation introduced by [Dazel et al 2007], which employs an alternative set of unknowns for the porous domain. In addition to the solid displacements  $\mathbf{u}_s$ , the so called total displacements  $\mathbf{u}_t$  are used as DOFs for the porous domain. Therefore, this formulation is also referred to as total displacement formulation. The total displacements thereby are given as linear combination of solid and fluid displacements:

$$\mathbf{u}_t = (1 - \phi)\mathbf{u}_s + \phi\mathbf{u}_f. \quad (3.72)$$

Likewise the classical formulation, the total displacement formulation introduces four DOFs per node for two-dimensional, and six DOFs per node for three-dimensional problems. The corresponding system of differential equations characterizing the porous domain is given in [Dazel et al 2007] and shall not be specified here. A weak formulation for the total displacement formulation can be found in [Dazel et al 2009].

According to [Dazel et al 2009], a significant advantage of the total displacement formulation results from the associated block-diagonal stiffness matrix, which in turn implies a decoupling of the elastic forces. [Dazel et al 2009] presents numerical solution strategies that exploit the decoupling of the elastic forces to reduce the computational cost for modelling porous media based on a FEM model. [Dazel et al 2007] shows that, compared to the formulations presented so far, the surface impedance and the transmission and reflection coefficient of the porous domain are easier to calculate when using the total displacement formulation, since the corresponding expressions can be rewritten in a simpler form.

Though the total displacement formulation was implemented as part of this work, it was not studied further.

### 3.3.6 Overview over different formulations

Table 3.2 gives an overview over the different formulations of the JCAM used within the scope of this thesis. In addition to the respective DOFs, it compares the underlying partial differential equation and its weak form, which forms the basis for the FEM model. The table makes no reference to the reduced classical formulation, as it is based on the same equations as the standard classical formulation. However, instead of the complex frequency dependent material parameters, only the first two terms of their Taylor expansion around the evolution point  $\omega = 0$  are used in the model, which in turn leads to frequency independent elemental matrices. Since it is not examined in greater detail in this work, no reference is made to the total displacement formulation at this point.

### 3.3.7 Application of the JCAM for modelling single-phase materials

The JCAM is an empirically based material model that has been specifically developed to represent the vibroacoustic properties of highly porous media. It is not suitable for modelling single-phase elastic structures and acoustic fluids, even if the porosity is chosen appropriately. For the following reasons, simply inserting  $\Phi \rightarrow 0$  (single-phase elastic structure) respectively  $\Phi \rightarrow 1$  (single-phase acoustic fluid) into the JCAM does not lead to convergence to the respective single-phase models: Since the coupling factors of fluid and solid DOFs do not disappear in the limit cases, an assumption would have to be made regarding the redundant DOF. In addition, the JCAM suffers from diverging material coefficients due to vanishing denominators for the limit case  $\Phi \rightarrow 0$ . For the classical formulation this problem could, however, be solved by applying L'Hôpital's rule.

## 3.4 Coupling and boundary conditions for porous media

To model complex vibroacoustic systems with porous components as shown in figure 3.2, one has to specify the depicted boundary and coupling conditions. Since in the case of porous media the primary variables are depending on the respective formulation, the boundary conditions of the porous domain along the boundary  $\Gamma_p$  are broken down into excitations and supports. An assignment to Neumann and Dirichlet boundary conditions can be made according to the considered formulation, taking into account the respective DOFs.

	Partial differential equation	Weak form
<b>Classical formulation</b> $\mathbf{u}_s, \mathbf{u}_f$	$\operatorname{div} \boldsymbol{\sigma}_s + \omega^2 (\tilde{\rho}_s \mathbf{u}_s + \tilde{\rho}_{sf} \mathbf{u}_f) = \mathbf{0}$ $\operatorname{div} \boldsymbol{\sigma}_f + \omega^2 (\tilde{\rho}_{sf} \mathbf{u}_s + \tilde{\rho}_f \mathbf{u}_f) = \mathbf{0}$	$\int_{\Omega_p} (\boldsymbol{\sigma}_s : \delta \boldsymbol{\varepsilon}_s - \omega^2 \tilde{\rho}_s \mathbf{u}_s \times \delta \mathbf{u}_s - \omega^2 \tilde{\rho}_{sf} \mathbf{u}_f \times \delta \mathbf{u}_s) \, d\Omega_p - \int_{\Gamma_p} \boldsymbol{\sigma}_s \mathbf{n}_p \times \delta \mathbf{u}_s \, d\Gamma_p = \mathbf{0}$ $\int_{\Omega_p} (\boldsymbol{\sigma}_f : \delta \boldsymbol{\varepsilon}_f - \omega^2 \tilde{\rho}_f \mathbf{u}_f \times \delta \mathbf{u}_f - \omega^2 \tilde{\rho}_{sf} \mathbf{u}_s \times \delta \mathbf{u}_f) \, d\Omega_p - \int_{\Gamma_p} \boldsymbol{\sigma}_f \mathbf{n}_p \times \delta \mathbf{u}_f \, d\Gamma_p = \mathbf{0}$
<b>Mixed formulation</b> $\mathbf{u}_s, p_f$	$\operatorname{div} \hat{\boldsymbol{\sigma}}_s + \omega^2 \tilde{\rho} \mathbf{u}_s + \tilde{\gamma} \nabla p_f = \mathbf{0}$ $\Delta p_f + \omega^2 \frac{\tilde{\rho}_f}{R} p_f - \omega^2 \frac{\tilde{\rho}_f}{\phi^2} \tilde{\gamma} \operatorname{div} \mathbf{u}_s = 0$ <p>with</p> $\boldsymbol{\sigma}_f = -\phi p_f \mathbf{I} \text{ and}$ $\hat{\boldsymbol{\sigma}}_s = \boldsymbol{\sigma}_s + \phi \frac{\tilde{Q}}{R} p_f \mathbf{I}$	$\int_{\Omega_p} (\hat{\boldsymbol{\sigma}}_s : \delta \boldsymbol{\varepsilon}_s - \omega^2 \tilde{\rho} \mathbf{u}_s \times \delta \mathbf{u}_s - \tilde{\gamma} \nabla p_f \times \delta \mathbf{u}_s) \, d\Omega_p - \int_{\Gamma_p} \hat{\boldsymbol{\sigma}}_s \mathbf{n}_p \times \delta \mathbf{u}_s \, d\Gamma_p = \mathbf{0}$ $\int_{\Omega_p} \left( \frac{\phi^2}{\tilde{\rho}_f} \nabla p_f \cdot \nabla \delta p_f - \omega^2 \frac{\phi^2}{R} p_f \delta p_f - \omega^2 \tilde{\gamma} \mathbf{u}_s \cdot \nabla \delta p_f \right) \, d\Omega_p$ $+ \int_{\Gamma_p} \left( \omega^2 \tilde{\gamma} u_{s,n} - \frac{\phi^2}{\tilde{\rho}_f} \frac{\partial p_f}{\partial \mathbf{n}_p} \right) \delta p_f \, d\Gamma_p = 0$
<b>New mixed formulation</b> $\mathbf{u}_s, p_f$	<p>equivalent to mixed formulation</p>	$\int_{\Omega_p} (\hat{\boldsymbol{\sigma}}_s : \delta \boldsymbol{\varepsilon}_s - \omega^2 \tilde{\rho} \mathbf{u}_s \times \delta \mathbf{u}_s - \frac{\phi}{\alpha} \nabla p_f \times \delta \mathbf{u}_s) - \phi \left( 1 + \frac{\tilde{Q}}{R} \right) (p_f \nabla \times \delta \mathbf{u}_s) \, d\Omega_p$ $- \int_{\Gamma_p} \boldsymbol{\sigma}_t \mathbf{n}_p \times \delta \mathbf{u}_s \, d\Gamma_p = \mathbf{0}$ $\int_{\Omega_p} \left( \frac{\phi^2}{\omega^2 \tilde{\rho}_f} \nabla p_f \cdot \nabla \delta p_f - \frac{\phi^2}{R} p_f \delta p_f - \frac{\phi}{\alpha} \mathbf{u}_s \cdot \nabla \delta p_f - \phi \left( 1 + \frac{\tilde{Q}}{R} \right) \nabla \cdot \mathbf{u}_s \delta p_f \right) \, d\Omega_p$ $- \int_{\Gamma_p} \phi (\mathbf{u}_f \cdot \mathbf{n}_p - \mathbf{u}_s \cdot \mathbf{n}_p) \delta p_f \, d\Gamma_p = 0$
<b>Equivalent fluid models</b> $p_f$	<p>Rigid frame model:</p> $\frac{1}{\tilde{\rho}_f} \Delta p_f + \omega^2 \frac{1}{R} p_f = 0$ <p>Limp frame model:</p> $\left( \frac{1}{\tilde{\rho}_f} + \frac{\tilde{\gamma}^2}{\phi^2 \tilde{\rho}} \right) \Delta p_f + \omega^2 \frac{1}{R} p_f = 0$	$\int_{\Omega_p} \left( \frac{1}{\tilde{\rho}_f} \nabla p_f \cdot \nabla \delta p_f - \omega^2 \frac{1}{R} p_f \delta p_f \right) \, d\Omega_p - \int_{\Gamma_p} \frac{1}{\tilde{\rho}_f} \frac{\partial p_f}{\partial \mathbf{n}_p} \delta p_f \, d\Gamma_p = 0$ $\int_{\Omega_p} \left( \frac{1}{\left( \frac{1}{\tilde{\rho}_f} + \frac{\tilde{\gamma}^2}{\phi^2 \tilde{\rho}} \right)} \nabla p_f \cdot \nabla \delta p_f - \omega^2 \frac{1}{R} p_f \delta p_f \right) \, d\Omega_p - \int_{\Gamma_p} \frac{1}{\left( \frac{1}{\tilde{\rho}_f} + \frac{\tilde{\gamma}^2}{\phi^2 \tilde{\rho}} \right)} \frac{\partial p_f}{\partial \mathbf{n}_p} \delta p_f \, d\Gamma_p = 0$

Table 3.2: Overview over different formulations of the JCAM used within this thesis.

Along the coupling edges between porous medium and other domains (acoustic domain, elastic domain, secondary porous domain and impermeable membrane) continuity and equilibrium must be fulfilled. Besides enforcing the continuity of the primary variable of the domain adjacent to the porous medium, the continuity of mass flow has to be ensured. Thus, for the coupling between porous medium and acoustic fluid, elastic structure or membrane, three coupling conditions result: One for the equilibrium, one for the continuity of the primary variable and one for a continuous mass flow. For the coupling between porous medium and secondary porous domain, four conditions are obtained, since the secondary porous domain has two primary variables.

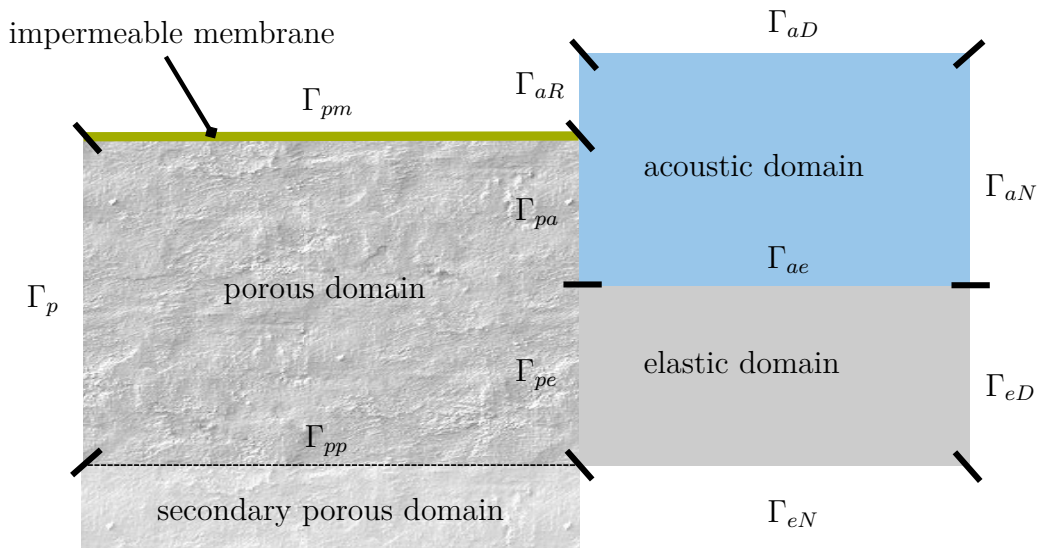


**Figure 3.2:** Coupled vibroacoustic system consisting of linear elastic, acoustic and porous domain.

First the conditions to be fulfilled at the boundary and coupling interfaces are specified. Afterwards it is described how these conditions are taken into account in a FEM model. The expressions below are based on [Debergue et al 1999] and [Allard and Atalla 2009].

### 3.4.1 Excitations

One option to excite the porous domain is to impose a certain pressure field  $p_\Gamma$  at the boundary  $\Gamma_p$ . The following set of equations has to be fulfilled along the respective boundary:

$$\left. \begin{aligned} \boldsymbol{\sigma}_t \mathbf{n}_p + p_\Gamma \mathbf{n}_p &= \mathbf{0} \\ p_f - p_\Gamma &= 0 \end{aligned} \right\} \quad \text{on } \Gamma_p, \quad (3.73)$$

with

$$\boldsymbol{\sigma}_t = \boldsymbol{\sigma}_s + \boldsymbol{\sigma}_f = \boldsymbol{\sigma}_s - \phi p_f \mathbf{I}. \quad (3.74)$$

The first condition in equation (3.73) ensures the equilibrium of the stresses, the second one the continuity of the pressure.

Imposing a pressure field corresponds to a Neumann boundary condition for the classical formulation, as in this case a secondary variable is prescribed along the boundary. Using the mixed formulation no clear assignment is possible. In fact, this kind of excitation results in a Dirichlet boundary condition for the fluid phase and a Neumann boundary condition for the solid phase when the mixed (or new mixed) formulation is used.

The second possibility to apply an excitation directly to the porous medium is to prescribe a displacement field  $\mathbf{u}_\Gamma$  along the boundary  $\Gamma_p$ , resulting in the following set of boundary conditions:

$$\left. \begin{array}{l} \mathbf{u}_s - \mathbf{u}_\Gamma = \mathbf{0} \\ \mathbf{u}_s \cdot \mathbf{n}_p - \mathbf{u}_f \cdot \mathbf{n}_p = 0 \end{array} \right\} \quad \text{on } \Gamma_p. \quad (3.75)$$

Enforcing the conditions above, the continuity between imposed displacement field and solid phase displacement as well as the continuity between normal displacements of solid and fluid phase are ensured along the excited boundary  $\Gamma_p$ .

Prescribing a displacement field corresponds to a Dirichlet boundary condition for the classical formulation, as the involved primary variables are fluid and solid phase displacements. Again, for the mixed (or new mixed) formulation no unique categorisation is possible.

### 3.4.2 Supports

A fixed edge is represented by the following boundary conditions:

$$\left. \begin{array}{l} \mathbf{u}_s = \mathbf{0} \\ \mathbf{u}_f \cdot \mathbf{n}_p = 0 \end{array} \right\} \quad \text{on } \Gamma_p. \quad (3.76)$$

Along a rigid boundary both, solid phase displacements and the normal displacements of the fluid phase fall to zero. An unique classification as Dirichlet boundary condition is only possible in the case of the classical formulation.

The case where only the displacement perpendicular to the edge is blocked by the bearing, but a displacement tangential to the edge is allowed, can be expressed by

$$\left. \begin{array}{l} \mathbf{u}_s \cdot \mathbf{n}_p = 0 \\ \mathbf{u}_f \cdot \mathbf{n}_p = 0 \end{array} \right\} \quad \text{on } \Gamma_p. \quad (3.77)$$

This is referred to as sliding edge condition. It corresponds to a Dirichlet boundary condition for the classical formulation and cannot be classified as a Dirichlet or Neumann boundary condition for the mixed (or new mixed) formulation.

A possibility to approximate the special case of a free radiating boundary is presented in [Debergue et al 1999]. [Debergue et al 1999] proposes to use a simplified model that does not take into account the complex coupling mechanism between the porous layer and the adjacent infinite acoustic fluid. The model considers a plate being coupled to the porous layer, which in turn is connected to an infinite acoustic fluid. It is assumed that the impedance of the solid phase of the porous medium is significantly higher than that of the infinite acoustic fluid and that consequently only the elastic deformations of the porous layer have an influence on the plate vibrations. This way, the impact of the infinite acoustic fluid on the porous layer is neglected and the system of porous medium and plate can be considered to vibrate in vacuum. Since this case is not relevant for the present work, it will not be discussed in more detail. A novel approach for modelling a radiating porous layer that also takes into account shape changes of the radiating boundary is proposed in the context of this work in section 4.4.4.

### 3.4.3 Poroelastic-elastic coupling

At the coupling interface  $\Gamma_{pe}$  between a porous and an elastic domain the following three coupling conditions need to be considered:

$$\left. \begin{array}{l} \boldsymbol{\sigma}_t \mathbf{n}_p - \boldsymbol{\sigma}_e \mathbf{n}_p = \mathbf{0} \\ \mathbf{u}_s - \mathbf{u}_e = \mathbf{0} \\ \mathbf{u}_s \cdot \mathbf{n}_p - \mathbf{u}_f \cdot \mathbf{n}_p = 0 \end{array} \right\} \quad \text{on } \Gamma_{pe}. \quad (3.78)$$

The first equation ensures the equilibrium of the normal stresses. The second one provides the continuity of the solid phase displacements and the displacements of the elastic structure. The third condition expresses that there is no relative mass flow over the coupling interface

$\Gamma_{pe}$ . It replaces the continuity of mass flow, respectively can be considered as a special case of it. The model used here for the elastic domain is presented in section 2.5.

In the context of this work, only the case in which porous and elastic domain are bonded is considered. [Rumpler 2012] also introduces the case where the displacements of the two coupling domains are only coupled in the direction perpendicular to the coupling edge. The displacements along the coupling edge are independent of each other. This is referred to as sliding interface and will not be discussed further in the scope of this thesis.

### 3.4.4 Poroelastic-acoustic coupling

The mutual coupling between a porous domain and an acoustic fluid is characterized by the following set of conditions along the common interface  $\Gamma_{pa}$ :

$$\left. \begin{aligned} \boldsymbol{\sigma}_t \mathbf{n}_p + p_a \mathbf{n}_p &= \mathbf{0} \\ p_f - p_a &= 0 \\ \frac{1}{\rho_a \omega^2} \frac{\partial p_a}{\partial \mathbf{n}_p} - (1 - \phi) \mathbf{u}_s \cdot \mathbf{n}_p - \phi \mathbf{u}_f \cdot \mathbf{n}_p &= 0 \end{aligned} \right\} \text{ on } \Gamma_{pa}. \quad (3.79)$$

The first equation considers the equilibrium of the normal stresses. The second equation expresses the continuity of pressure, which is the primary variable (DOF) of the acoustic fluid. The third equation ensures the continuity of mass flow by enforcing that the relative normal displacement of the multiphase continuum and the normal displacements the acoustic fluid are equal. The acoustic fluid itself is characterized in section 2.4.

### 3.4.5 Poroelastic-poroelastic coupling

Furthermore, the coupling of two porous domains with different material properties is considered. Along their common interface  $\Gamma_{pp}$  the following conditions shall be fulfilled:

$$\left. \begin{aligned} \boldsymbol{\sigma}_{t1} \mathbf{n}_{p1} - \boldsymbol{\sigma}_{t2} \mathbf{n}_{p1} &= \mathbf{0} \\ \mathbf{u}_{s1} - \mathbf{u}_{s2} &= \mathbf{0} \\ p_{f1} - p_{f2} &= 0 \\ \phi_1 (\mathbf{u}_{f1} - \mathbf{u}_{s1}) \cdot \mathbf{n}_{p1} - \phi_2 (\mathbf{u}_{f2} - \mathbf{u}_{s2}) \cdot \mathbf{n}_{p1} &= 0 \end{aligned} \right\} \text{ on } \Gamma_{pp}. \quad (3.80)$$

The individual domains are identified by the indices  $\square_1$  and  $\square_2$ . The first condition expresses the equilibrium of the normal stresses. As the secondary porous domain adjacent

to the porous domain also has two primary variables, two equations are required to express the continuity of DOFs: The second equation considers the continuity of the solid phase displacements; the third equation considers the continuity of the pore pressure. Enforcing the fourth condition, a continuous mass flow across  $\Gamma_{pp}$  is ensured.

### 3.4.6 Poroelastic-membrane coupling

Finally, we consider the case where a limp, impermeable membrane having a certain surface density  $m$  is attached to the porous domain. This results in the following conditions along the interface  $\Gamma_{pm}$ :

$$\left. \begin{aligned} \boldsymbol{\sigma}_t \mathbf{n}_p - \mathbf{t}_m &= \mathbf{0} \\ \mathbf{u}_s - \mathbf{u}_m &= \mathbf{0} \\ \mathbf{u}_s \cdot \mathbf{n}_p - \mathbf{u}_f \cdot \mathbf{n}_p &= 0 \end{aligned} \right\} \quad \text{on } \Gamma_{pm}, \quad (3.81)$$

with  $\mathbf{u}_m$  being the displacements and  $\mathbf{t}_m$  the exterior traction forces corresponding to the membrane. Again, the first condition considers the continuity of normal stresses. The continuity of displacements is ensured by the second condition. The third equation expresses that there is no mass flow across  $\Gamma_{pm}$ .

The weak integral form of the membrane itself is given by

$$\int_{\Gamma_{sm}} \omega^2 m \mathbf{u}_m \times \delta \mathbf{u}_m d\Gamma_{pm} + \int_{\Gamma_{pm}} \mathbf{t}_m \times \delta \mathbf{u}_m d\Gamma_{pm} + \int_{\Gamma_{pm}} \mathbf{f}_m \times \delta \mathbf{u}_m d\Gamma_{pm} = \mathbf{0}, \quad (3.82)$$

with  $\mathbf{f}_m$  being the membrane's load vector. In comparison to the other domains, no lateral extension is assigned to the membrane. Thus, it is represented by one-dimensional elements for two-dimensional problems. Introducing the continuity of the displacements  $\mathbf{u}_s = \mathbf{u}_m$  in equation (3.82), we can interpret the membrane as additional mass applied on pore framework at the boundary nodes.

### 3.4.7 Numerical implementation

This section gives conclusion on how the boundary and coupling conditions introduced above are implemented for the different formulations of the porous domain. The following expressions are obtained by substituting the previously introduced boundary and coupling conditions into the boundary integrals of the weak formulation(s) of the adjacent domain(s). Once



again the procedure is shown on the example of a two-dimensional system that is meshed using quadrilateral elements.

### Classical formulation

- *Excitations*

As mentioned earlier, the imposition of a pressure field  $p_\Gamma$  corresponds to a Neumann boundary condition when the classical formulation is used. As a result, we get a right hand side contribution for the solid and fluid phase:

$$\mathbf{f}_{s_e}^c = -(1 - \phi) \int_{\Gamma_{p_e}} \mathbf{N}_{u\Gamma}^\top p_\Gamma \mathbf{n}_p \, d\Gamma_{p_e}, \quad (3.83)$$

$$\mathbf{f}_{f_e}^c = -\phi \int_{\Gamma_{p_e}} \mathbf{N}_{u\Gamma}^\top p_\Gamma \mathbf{n}_p \, d\Gamma_{p_e}, \quad (3.84)$$

with  $\Gamma_{p_e}$  being the one-dimensional boundary of a two-dimensional porous element.

The Dirichlet boundary condition of imposing a displacement field  $\mathbf{u}_\Gamma$  can be considered analogously as described in section 2.5.2 for the case of a linear elastic structural domain.

- *Supports*

Since they represent Dirichlet boundary conditions when using the classical formulation, the fixed and sliding boundary conditions are implemented like a Dirichlet boundary condition of a linear elastic structural domain (see section 2.5.2).

- *Poroelastic-elastic coupling*

Using the classical formulation for the porous domain, the boundary integral  $I_{\Gamma_{p_e}}^c$  along the coupling interface  $\Gamma_{p_e}$  is given as

$$I_{\Gamma_{p_e}}^c = - \int_{\Gamma_{p_e}} \boldsymbol{\sigma}_s \mathbf{n}_p \times \delta \mathbf{u}_s \, d\Gamma_{p_e} - \int_{\Gamma_{p_e}} \boldsymbol{\sigma}_f \mathbf{n}_p \times \delta \mathbf{u}_f \, d\Gamma_{p_e} + \int_{\Gamma_{p_e}} \boldsymbol{\sigma}_e \mathbf{n}_p \times \delta \mathbf{u}_e \, d\Gamma_{p_e}. \quad (3.85)$$

Introducing the equilibrium condition of equation (3.78) into equation (3.85),  $I_{\Gamma_{p_e}}^c$  vanishes. The continuity conditions of equation (3.78) are taken into account in the assembling procedure.

- *Poroelastic-acoustic coupling*

Coupling a porous domain represented by the classical formulation and an acoustic

fluid results in the following boundary integral, which is composed of a vector and a scalar contribution:

$$I_{\Gamma_{pa}}^c = \underbrace{- \int_{\Gamma_{pa}} \boldsymbol{\sigma}_s \mathbf{n}_p \times \delta \mathbf{u}_s \, d\Gamma_{pa} - \int_{\Gamma_{pa}} \boldsymbol{\sigma}_f \mathbf{n}_p \times \delta \mathbf{u}_f \, d\Gamma_{pa}}_{\text{vector contribution}} + \underbrace{\int_{\Gamma_{pa}} \frac{1}{\rho_a} \frac{\partial p_a}{\partial \mathbf{n}_a} \delta p_a \, d\Gamma_{pa}}_{\text{scalar contribution}}. \quad (3.86)$$

Inserting equation (3.79) into the expression above, we can derive the contributions to the mass and stiffness matrix mapping the mutual coupling:

$$\mathbf{K}_{pa_e}^c = \begin{bmatrix} \mathbf{K}_{sa_e}^c \\ \mathbf{K}_{fa_e}^c \end{bmatrix} = \begin{bmatrix} (1 - \phi) \int_{\Gamma_{pa_e}} \mathbf{N}_{u\Gamma}^\top \mathbf{n}_p \mathbf{N}_p \, d\Gamma_{pa_e} \\ \phi \int_{\Gamma_{pa_e}} \mathbf{N}_{u\Gamma}^\top \mathbf{n}_p \mathbf{N}_p \, d\Gamma_{pa_e} \end{bmatrix}, \quad (3.87)$$

$$\mathbf{M}_{pa_e}^c = \begin{bmatrix} \mathbf{M}_{sa_e}^c & \mathbf{M}_{fa_e}^c \end{bmatrix} = -\mathbf{K}_{pa_e}^{c\top}, \quad (3.88)$$

with  $\Gamma_{pa_e}$  being the one-dimensional interface between two-dimensional porous and acoustic elements.

- *Poroelastic-poroelastic coupling*

The boundary integral along the coupling interface  $\Gamma_{pp}$  reads:

$$I_{\Gamma_{pp}}^c = - \int_{\Gamma_{pp}} \boldsymbol{\sigma}_{s1} \mathbf{n}_{p1} \times \delta \mathbf{u}_{s1} \, d\Gamma_{pp} - \int_{\Gamma_{pp}} \boldsymbol{\sigma}_{f1} \mathbf{n}_{p1} \times \delta \mathbf{u}_{f1} \, d\Gamma_{pp} \\ + \int_{\Gamma_{pp}} \boldsymbol{\sigma}_{s2} \mathbf{n}_{p1} \times \delta \mathbf{u}_{s2} \, d\Gamma_{pp} + \int_{\Gamma_{pp}} \boldsymbol{\sigma}_{f2} \mathbf{n}_{p1} \times \delta \mathbf{u}_{f2} \, d\Gamma_{pp}. \quad (3.89)$$

Inserting the boundary conditions introduced in equation (3.80),  $I_{\Gamma_{pp}}^c$  vanishes. Only the continuity of the displacement fields has to be considered in the assembling procedure.

- *Poroelastic-membrane coupling*

Summing up the individual boundary representations, we get the boundary integral along  $\Gamma_{pm}$ :

$$I_{\Gamma_{pm}}^c = - \int_{\Gamma_{pm}} \boldsymbol{\sigma}_s \mathbf{n}_p \times \delta \mathbf{u}_s \, d\Gamma_{pm} - \int_{\Gamma_{pm}} \boldsymbol{\sigma}_f \mathbf{n}_p \times \delta \mathbf{u}_f \, d\Gamma_{pm} \\ + \int_{\Gamma_{pm}} \omega^2 m \mathbf{u}_m \times \delta \mathbf{u}_m \, d\Gamma_{pm} + \int_{\Gamma_{pm}} \mathbf{t}_m \times \delta \mathbf{u}_m \, d\Gamma_{pm} + \int_{\Gamma_{pm}} \mathbf{f}_m \times \delta \mathbf{u}_m \, d\Gamma_{pm}. \quad (3.90)$$

Introducing equations (3.81), we can find that the coupling between porous domain

and membrane results in a contribution to the mass matrix and the right hand side vector of the solid phase:

$$\mathbf{M}_{\text{sm}_e}^c = - \int_{\Gamma_{\text{pm}_e}} m \mathbf{N}_{\text{u}\Gamma}^\top \mathbf{N}_{\text{u}\Gamma} d\Gamma_{\text{pm}_e}, \quad (3.91)$$

$$\mathbf{f}_{\text{sm}_e}^c = - \int_{\Gamma_{\text{pm}_e}} \mathbf{N}_{\text{u}\Gamma}^\top \mathbf{f}_m d\Gamma_{\text{pm}_e}; \quad (3.92)$$

$\Gamma_{\text{pm}_e}$  is the one-dimensional coupling interface between porous medium and membrane on element level.

In addition to the coupling contributions above, the continuity of the normal displacements of solid and fluid phase  $\mathbf{u}_s \cdot \mathbf{n}_p = \mathbf{u}_f \cdot \mathbf{n}_p$  has to be enforced in the assembling procedure.

- *Coupled vibroacoustic system*

In the case where the porous domain is represented by the classical formulation, setting up equation (2.1) for the vibroacoustic system sketched in figure 3.2 results in

$$\left( \begin{array}{cccc} \mathbf{K}_a & \mathbf{0} & \mathbf{0} & \mathbf{0} \\ \mathbf{K}_{ae} & \mathbf{K}_e & \mathbf{0} & \mathbf{0} \\ \mathbf{K}_{sa}^c & \mathbf{0} & & \\ \mathbf{K}_{fa}^c & \mathbf{0} & \tilde{\mathbf{K}}_p^c & \end{array} \right) - \omega^2 \left( \begin{array}{cccc} \mathbf{M}_a & \mathbf{M}_{ae} & \mathbf{M}_{sa}^c & \mathbf{M}_{fa}^c \\ \mathbf{0} & \mathbf{M}_e & \mathbf{0} & \mathbf{0} \\ \mathbf{0} & \mathbf{0} & \tilde{\mathbf{M}}_s^c + \mathbf{M}_{sm}^c & \tilde{\mathbf{M}}_{sf}^c \\ \mathbf{0} & \mathbf{0} & \tilde{\mathbf{M}}_{sf}^c & \tilde{\mathbf{M}}_f^c \end{array} \right) \begin{bmatrix} \mathbf{p}_a \\ \mathbf{u}_e \\ \mathbf{u}_s \\ \mathbf{u}_f \end{bmatrix} = \begin{bmatrix} \mathbf{f}_a \\ \mathbf{f}_e \\ \mathbf{f}_s^c + \mathbf{f}_{sm}^c \\ \mathbf{f}_f^c \end{bmatrix}. \quad (3.93)$$

The yet non-symmetric representation can be transferred into a symmetric equation system by dividing the first row, which corresponds to the acoustic fluid, by  $\omega^2$ . To abbreviate the expression, an acoustic fluid without Robin boundary is assumed here. The system of equations can be extended analogously to equation (2.41) if the free radiation at an edge of the acoustic fluid is to be modelled.

### Mixed formulation

According to [Debergue et al 1999], we can simplify the boundary and coupling contributions involved with the mixed formulation by rewriting the boundary integrals contained in

equations (3.56) in the following way:

$$\begin{aligned}
 I_{\Gamma_p}^m = & - \underbrace{\int_{\Gamma_p} (\boldsymbol{\sigma}_t \mathbf{n}_p \times \delta \mathbf{u}_s + p_f \mathbf{n}_p \times \delta \mathbf{u}_s) d\Gamma_p}_{\text{vector contribution}} \\
 & - \underbrace{\int_{\Gamma_p} (\mathbf{u}_s \cdot \mathbf{n}_p \delta p_f + \phi (\mathbf{u}_f \cdot \mathbf{n}_p - \mathbf{u}_s \cdot \mathbf{n}_p) \delta p_f) d\Gamma_p}_{\text{scalar contribution}},
 \end{aligned} \tag{3.94}$$

when using  $\phi \left(1 + \frac{\tilde{Q}}{R}\right) \approx 1$ , which, according to [Allard and Atalla 2009], holds for typical sound-absorbing porous materials.  $I_{\Gamma_p}^m$  summarizes the boundary integrals from the solid and fluid equation and consequently consists of vector and scalar contributions. As a consequence, all boundary integrals formulated in this section along the coupling interfaces consist of scalar and vector contributions as well. A specification of these will be omitted in the following.

- *Excitations*

Prescribing a pressure field  $p_\Gamma$  at the edge of a porous domain which is modelled by the mixed formulation is a Dirichlet boundary condition for the fluid phase. It can be employed like described in section 2.4.2 for an acoustic fluid. Even though imposing  $p_\Gamma$  is a Neumann boundary condition for the solid phase, we don't have to consider a right hand side contribution as  $I_{\Gamma_p}^m$  vanishes when inserting the boundary conditions contained in equations (3.73).

Imposing a displacement field  $\mathbf{u}_\Gamma$  corresponds to a Dirichlet boundary condition for the solid phase and is treated in analogy to section 2.5.2. For the fluid phase, this excitation is a Neumann boundary condition and results in the following right hand side contribution:

$$\mathbf{f}_{f_e}^m = \int_{\Gamma_{pe}} \mathbf{N}_{p\Gamma}^\top (\mathbf{u}_\Gamma \cdot \mathbf{n}_p) d\Gamma_{pe}. \tag{3.95}$$

- *Supports*

For both fixed and sliding edge supports,  $I_{\Gamma_p}^m$  vanishes and only the Dirichlet boundary conditions of the solid phase have to be considered in analogy to section 2.5.2.

- *Poroelastic-elastic coupling*

The boundary integral  $I_{\Gamma_{pe}}^m$  corresponding to the mixed formulation reads

$$\begin{aligned} I_{\Gamma_{pe}}^m = & - \int_{\Gamma_{pe}} (\mathbf{u}_s \cdot \mathbf{n}_p \delta p_f + \phi (\mathbf{u}_f \cdot \mathbf{n}_p - \mathbf{u}_s \cdot \mathbf{n}_p) \delta p_f) d\Gamma_{pe} \\ & - \int_{\Gamma_{pe}} (\boldsymbol{\sigma}_t \mathbf{n}_p \times \delta \mathbf{u}_s + p_f \mathbf{n}_p \times \delta \mathbf{u}_s) d\Gamma_{pe} + \int_{\Gamma_{pe}} \boldsymbol{\sigma}_e \mathbf{n}_p \times \mathbf{u}_e d\Gamma_{pe}. \end{aligned} \quad (3.96)$$

Inserting the boundary conditions given along the interface between porous and structural domain, we can derive a symmetrical coupling contribution to the stiffness matrix:

$$\mathbf{K}_{fe}^m = - \int_{\Gamma_{pa_e}} \mathbf{N}_{ul}^\top \mathbf{n}_p \mathbf{N}_{p\Gamma} d\Gamma_{pa_e}. \quad (3.97)$$

Additionally,  $\mathbf{u}_s = \mathbf{u}_e$  has to be ensured by the assembling procedure.

- *Poroelastic-acoustic coupling*

Using the mixed formulation, we can derive the coupling contributions between porous domain and acoustic fluid based on the following boundary integral:

$$\begin{aligned} I_{\Gamma_{pa}}^m = & - \int_{\Gamma_{pa}} (\boldsymbol{\sigma}_t \mathbf{n}_p \times \delta \mathbf{u}_s + p_f \mathbf{n}_p \times \delta \mathbf{u}_s) d\Gamma_{pa} \\ & - \int_{\Gamma_{pa}} (\mathbf{u}_s \cdot \mathbf{n}_p \delta p_f + \phi (\mathbf{u}_f \cdot \mathbf{n}_p - \mathbf{u}_s \cdot \mathbf{n}_p) \delta p_f) d\Gamma_{pa} + \int_{\Gamma_{pa}} \frac{1}{\rho_a} \frac{\partial p_a}{\partial \mathbf{n}_a} \delta p_a d\Gamma_{pa}. \end{aligned} \quad (3.98)$$

Inserting equations (3.79) into equation (3.98),  $I_{\Gamma_{pa}}^m$  vanishes. Thus, only  $p_f = p_a$  has to be considered in the assembling procedure.

- *Poroelastic-poroelastic coupling*

$I_{\Gamma_{pp}}^m$  corresponding to the mixed formulation reads:

$$\begin{aligned} I_{\Gamma_{pp}}^m = & - \int_{\Gamma_{pp}} (\boldsymbol{\sigma}_{t1} \mathbf{n}_{p1} \times \delta \mathbf{u}_{s1} + p_{f1} \mathbf{n}_{p1} \times \delta \mathbf{u}_{s1}) d\Gamma_{pp} \\ & - \int_{\Gamma_{pp}} (\mathbf{u}_{s1} \cdot \mathbf{n}_{p1} \delta p_{f1} + \phi_1 (\mathbf{u}_{f1} \cdot \mathbf{n}_{p1} - \mathbf{u}_{s1} \cdot \mathbf{n}_{p1}) \delta p_{f1}) d\Gamma_{pp} \\ & + \int_{\Gamma_{pp}} (\boldsymbol{\sigma}_{t2} \mathbf{n}_{p1} \times \delta \mathbf{u}_{s2} + p_{f2} \mathbf{n}_{p1} \times \delta \mathbf{u}_{s2}) d\Gamma_{pp} \\ & + \int_{\Gamma_{pp}} (\mathbf{u}_{s2} \cdot \mathbf{n}_{p1} \delta p_{f2} + \phi_2 (\mathbf{u}_{f2} \cdot \mathbf{n}_{p1} - \mathbf{u}_{s2} \cdot \mathbf{n}_{p1}) \delta p_{f2}) d\Gamma_{pp}. \end{aligned} \quad (3.99)$$

Inserting the respective coupling conditions for the interface  $\Gamma_{pp}$ ,  $I_{\Gamma_{pp}}^m$  vanishes. The continuity of solid displacements and pore pressure is to be fulfilled in the assembling procedure.

- *Poroelastic-membrane coupling*

Coupling a membrane to a porous domain represented by the mixed formulation results in the following boundary integral:

$$\begin{aligned} I_{\Gamma_{pm}}^m = & - \int_{\Gamma_{pm}} (\boldsymbol{\sigma}_t \mathbf{n}_p \times \delta \mathbf{u}_s + p_f \mathbf{n}_p \times \delta \mathbf{u}_s) d\Gamma_{pm} \\ & - \int_{\Gamma_{pm}} (\mathbf{u}_s \cdot \mathbf{n}_p \delta p_f + \phi (\mathbf{u}_f \cdot \mathbf{n}_p - \mathbf{u}_s \cdot \mathbf{n}_p) \delta p_f) d\Gamma_{pm} \\ & + \int_{\Gamma_{pm}} \omega^2 m \mathbf{u}_m \times \delta \mathbf{u}_m d\Gamma_{pm} + \int_{\Gamma_{pm}} \mathbf{t}_m \times \delta \mathbf{u}_m d\Gamma_{pm} + \int_{\Gamma_{pm}} \mathbf{f}_m \times \delta \mathbf{u}_m d\Gamma_{pm}. \end{aligned} \quad (3.100)$$

Inserting equation (3.81), we can find that the mutual coupling is represented by a symmetrical coupling contribution to the stiffness matrix of the porous domain and a contribution to the mass matrix and the right hand side vector of the solid phase:

$$\mathbf{K}_{pm_e}^m = - \int_{\Gamma_{pa_e}} \mathbf{N}_{u\Gamma}^T \mathbf{n}_p \mathbf{N}_{p\Gamma} d\Gamma_{pa_e}, \quad (3.101)$$

$$\mathbf{M}_{sm_e}^m = - \int_{\Gamma_{pm_e}} m \mathbf{N}_{u\Gamma}^T \mathbf{N}_{u\Gamma} d\Gamma_{pm_e}, \quad (3.102)$$

$$\mathbf{f}_{sm_e}^m = - \int_{\Gamma_{pm_e}} \mathbf{N}_{u\Gamma}^T \mathbf{f}_m d\Gamma_{pm_e}. \quad (3.103)$$

- *Coupled vibroacoustic system*

The equation of motion for a coupled vibroacoustic system with porous components modelled with the mixed formulation reads:

$$\left( \begin{bmatrix} \mathbf{K}_a & \mathbf{0} & \mathbf{0} & \mathbf{0} \\ \mathbf{K}_{ae} & \mathbf{K}_e & \mathbf{0} & \mathbf{K}_{fe}^m \\ \mathbf{0} & \mathbf{0} & \mathbf{K}_s^m & \tilde{\mathbf{K}}_{sf}^m + \mathbf{K}_{pm}^m \\ \mathbf{0} & \mathbf{K}_{fe}^{m\top} & \mathbf{K}_{pm}^{m\top} & \tilde{\mathbf{K}}_f^m \end{bmatrix} - \omega^2 \begin{bmatrix} \mathbf{M}_a & \mathbf{M}_{ae} & \mathbf{0} & \mathbf{0} \\ \mathbf{0} & \mathbf{M}_e & \mathbf{0} & \mathbf{0} \\ \mathbf{0} & \mathbf{0} & \tilde{\mathbf{M}}_s^m + \mathbf{M}_{sm}^m & \mathbf{0} \\ \mathbf{0} & \mathbf{0} & \tilde{\mathbf{M}}_{sf}^m & \tilde{\mathbf{M}}_f^m \end{bmatrix} \right) \begin{bmatrix} \mathbf{p}_a \\ \mathbf{u}_e \\ \mathbf{u}_s \\ \mathbf{p}_f \end{bmatrix} = \begin{bmatrix} \mathbf{f}_a \\ \mathbf{f}_e \\ \mathbf{f}_{sm}^m \\ \mathbf{f}_f^m \end{bmatrix}. \quad (3.104)$$

Again, no Robin boundary along the acoustic fluid is considered here.

While, as explained in detail in [Debergue et al 1999], implementing boundary and

coupling conditions takes less effort when modelling the porous domain with the mixed formulation than when using the classical formulation, we can not derive a symmetric system of equations here.

### New mixed formulation

Using the new mixed formulation introduced by [Atalla et al 2001], the effort for implementing coupling and boundary conditions can be further reduced. Exception to this is the coupling between a porous domain and an acoustic fluid, which requires less effort when using the original mixed formulation. The boundary integral corresponding to the new mixed formulation can be read from equations (3.65):

$$I_{\Gamma_p}^{m*} = - \underbrace{\int_{\Gamma_p} \boldsymbol{\sigma}_t \mathbf{n}_p \times \delta \mathbf{u}_s \, d\Gamma_p}_{\text{vector contribution}} - \underbrace{\int_{\Gamma_p} \phi (\mathbf{u}_f \cdot \mathbf{n}_p - \mathbf{u}_s \cdot \mathbf{n}_p) \delta p_f \, d\Gamma_p}_{\text{scalar contribution}}. \quad (3.105)$$

The term corresponds to an abbreviated version of the expression for the original mixed formulation and also includes vector and scalar contributions.

Below, only the resulting contributions corresponding to the individual boundaries and couplings are named. The individual boundary integrals along the interfaces are set up analogously to the classical and mixed formulation and are not explicitly displayed here.

- *Excitations*

In comparison to the original mixed formulation, prescribing a pressure field  $p_\Gamma$  results in a right hand side contribution for the solid phase  $\mathbf{f}_{s_e}$  in addition to the Dirichlet boundary condition for the pore pressure  $p_f$ , with

$$\mathbf{f}_{s_e}^{m*} = \int_{\Gamma_{pe}} \mathbf{N}_{u\Gamma}^\top p_\Gamma \mathbf{n}_p \, d\Gamma_{pe}. \quad (3.106)$$

Imposing  $\mathbf{u}_\Gamma$  along the boundary of the porous domain, the boundary integral vanishes and we only need to implement the corresponding Dirichlet boundary condition for the solid phase.

- *Supports*

As the boundary integral vanishes for both, fixed and sliding edge supports, only the corresponding Dirichlet boundary conditions for the solid phase have to be modelled.

- *Poroelastic-elastic coupling*

Using the new mixed formulation, the boundary integral along the interface between porous and structural domain vanishes. This corresponds to a natural coupling. Only the continuity of displacements  $\mathbf{u}_p = \mathbf{u}_e$  has to be ensured by the assembling procedure.

- *Poroelastic-acoustic coupling*

In addition to the continuity of pressure that is fulfilled by the assembling procedure, we need to add symmetric coupling contributions to the stiffness matrix when coupling an acoustic fluid with a porous domain which is represented by the new mixed formulation:

$$\mathbf{K}_{sa_e}^{m*} = - \int_{\Gamma_{pa_e}} \mathbf{N}_{u\Gamma}^\top \mathbf{n}_p \mathbf{N}_{p\Gamma} d\Gamma_{pa_e}. \quad (3.107)$$

- *Poroelastic-poroelastic coupling*

Coupling two porous domains that are both represented by the new mixed formulation, we only need to ensure the continuity of solid displacements and pore pressure along the interface in the assembling procedure.

- *Poroelastic-membrane coupling*

Using the new mixed formulation for the porous domain, the coupling with a membrane results in a contribution to the mass matrix and the right hand side of the solid phase:

$$\mathbf{M}_{sm_e}^{m*} = - \int_{\Gamma_{pm_e}} m \mathbf{N}_{u\Gamma}^\top \mathbf{N}_{u\Gamma} d\Gamma_{pm_e}, \quad (3.108)$$

$$\mathbf{f}_{sm_e}^{m*} = - \int_{\Gamma_{pm_e}} \mathbf{N}_{u\Gamma}^\top \mathbf{f}_m d\Gamma_{pm_e}. \quad (3.109)$$

- *Coupled vibroacoustic system*

Modelling the porous components with the new mixed formulation, we can derive the following system of equations for a coupled vibroacoustic system:

$$\left( \begin{bmatrix} \mathbf{K}_a & \mathbf{0} & \mathbf{K}_{sa}^{m*\top} & \mathbf{0} \\ \mathbf{K}_{ae} & \mathbf{K}_e & \mathbf{0} & \mathbf{0} \\ \mathbf{K}_{sa}^{m*} & \mathbf{0} & \mathbf{K}_s^m & \tilde{\mathbf{K}}_{sf}^{m*} \\ \mathbf{0} & \mathbf{0} & \mathbf{0} & \tilde{\mathbf{K}}_f^m \end{bmatrix} - \omega^2 \begin{bmatrix} \mathbf{M}_a & \mathbf{M}_{ae} & \mathbf{0} & \mathbf{0} \\ \mathbf{0} & \mathbf{M}_e & \mathbf{0} & \mathbf{0} \\ \mathbf{0} & \mathbf{0} & \tilde{\mathbf{M}}_s^m + \mathbf{M}_{sm}^{m*} & \mathbf{0} \\ \mathbf{0} & \mathbf{0} & \tilde{\mathbf{M}}_{sf}^{m*} & \tilde{\mathbf{M}}_f^m \end{bmatrix} \right) \begin{bmatrix} \mathbf{p}_a \\ \mathbf{u}_e \\ \mathbf{u}_s \\ \mathbf{p}_f \end{bmatrix} = \begin{bmatrix} \mathbf{f}_a \\ \mathbf{f}_e \\ \mathbf{f}_s^{m*} + \mathbf{f}_{sm}^{m*} \\ \mathbf{0} \end{bmatrix}. \quad (3.110)$$



We can conclude that the overall effort for implementing coupling and boundary conditions of a vibroacoustic system can be reduced, when using the new mixed formulation instead of the original mixed formulation. Solely the implementation of the coupling between the porous domain and the acoustic fluid is more complex.

### Overview over implementation of coupling and boundary conditions

Table 3.3 gives an overview over the effort involved for implementing the coupling and boundary conditions according to the classical, mixed and new mixed formulation. Since the equivalent fluid models can be considered as reduced versions of the mixed formulation, introducing only the pore pressure as DOF and thus leading to simplified coupling conditions, they are not explicitly discussed here. Further, no reference is made to the total displacement formulation, as it isn't used to model porous domains in the context of this thesis.

			<b>Classical formulation<sup>1</sup></b>	<b>Mixed formulation</b>	<b>New mixed formulation</b>
<b>Boundary conditions</b>	<b>Excitations</b>	Imposed pressure field	Right hand side contribution	Imposition of resp. Dirichlet BC	Imposition of resp. Dirichlet BC and right hand side contribution
		Imposed displacement field	Imposition of resp. Dirichlet BC	Imposition of resp. Dirichlet BC and right hand side contribution	Imposition of resp. Dirichlet BC
	<b>Supports</b>	Fixed edge		Imposition of resp. Dirichlet BC	Imposition of resp. Dirichlet BC
		Sliding edge			
<b>Coupling conditions<sup>2</sup></b>	Poroelastic-elastic coupling		-	Coupling contributions to elemental matrices	-
	Poroelastic-acoustic coupling		Coupling contributions to elemental matrices	-	Coupling contributions to elemental matrices
	Poroelastic-poroelastic coupling		-		
	Poroelastic-membrane coupling		Right hand side contribution and coupling contributions to elemental matrices		

**Table 3.3:** Overview over implementation of coupling and boundary conditions.

## 3.5 Comparison of the formulations on test configurations

The different formulations of the JCAM introduced in section 3.3 are now compared on two two-dimensional application cases. First, the test configurations are defined. To show the effect of the investigated absorber configurations, the test cavity is also analysed for the case where no absorber is installed. After validating the calculation results referring to the literature, the calculation results obtained from the different formulations are compared. In the interpretation, particular focus is put on the approximation error introduced by the reduced classical formulation.

### 3.5.1 Definition of the test configurations

To compare the different formulations of the JCAM introduced in section 3.3, the two two-dimensional application cases depicted in figure 3.3 are defined. Both configurations consist of an acoustic cavity that is coupled to a porous absorber. The dimensions of the coupled systems are the same. The systems are excited by prescribing the amplitude of the displacement in the left lower corner of the acoustic cavity to the value  $3 \cdot 10^{-5}$  m. The displacement is assumed to decline linearly from the left lower corner to the neighbouring boundary nodes. The remaining part of the outer edges of the acoustic cavities are assumed to be fully reflecting. The porous layers are supported by fixed edge conditions at their backs and sliding edge conditions on their sides.

Since the relevant wave propagation patterns in the system are difficult to estimate due to complex reflections on the rigid side walls of the cavity, the required node density is determined via stepwise refinement of the mesh. It is found that the solution converges over the considered frequency range from 0 to 2000 Hz when the geometries are meshed with quadrilateral elements with an edge length of 0.002 m. As an estimate for the shortest wavelength in the system, the slower compressional wave in the porous absorber determined via equation (3.3) is divided by the highest excitation frequency. For the mesh used, this results in about a minimum of four nodes per wavelength. Since equation (3.3) assumes wave propagation in an infinitely extended, three-dimensional porous medium, this can, if at all, only be classified as a rough estimation.

---

<sup>1</sup>The reduced classical formulation is based on the same equations as the standard classical formulation and therefore generally involves the same coupling effort. As a simplification of the frequency dependent quantities is performed, elemental matrices and also the coupling contributions to them are frequency independent.

<sup>2</sup>In addition to the respective contributions to right hand side and elemental matrices, the continuity of DOFs along all coupling interfaces has to be ensured in the assembling step.

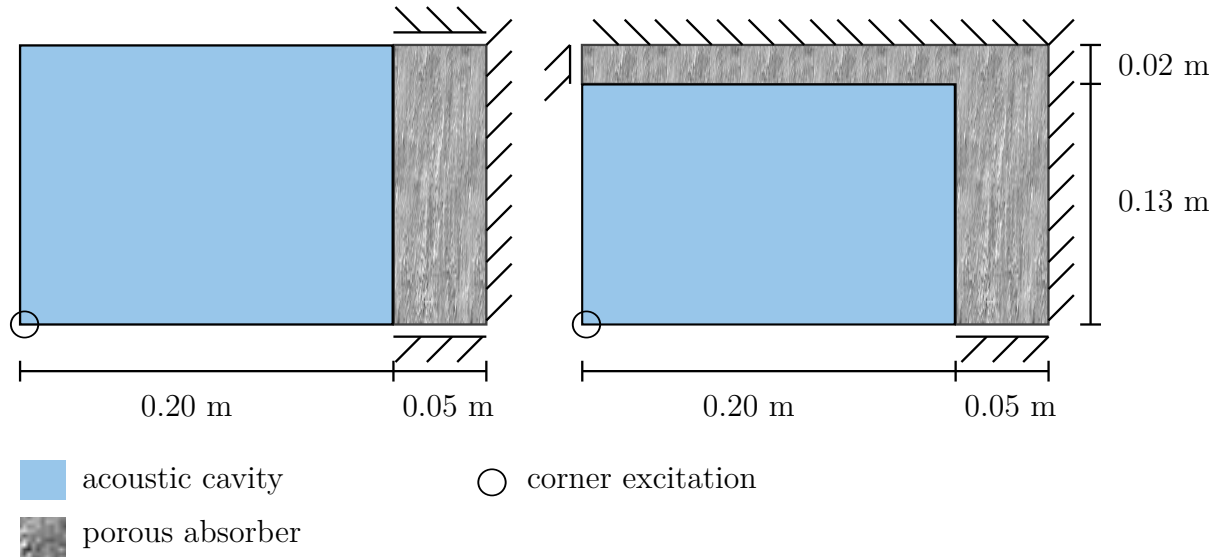


**Figure 3.3:** Test configurations for comparison of different JCAM formulations.

For both application cases the material parameters of the porous absorber are given in table 3.4. The fluid in the acoustic cavity and the pores is air.

<b>Solid frame</b>	$\rho_s = 750 \frac{\text{kg}}{\text{m}^3}$ $\lambda_s = 487.5 \cdot 10^3 \text{ Pa}$ $\mu_s = 325 \cdot 10^3 \text{ Pa}$ $\eta_s = 0$
<b>Fluid phase</b>	$\rho_f = 1.21 \frac{\text{kg}}{\text{m}^3}$ $\eta = 1.84 \cdot 10^{-8} \frac{\text{Ns}}{\text{m}^2}$ $P_0 = 101 \cdot 10^3 \text{ Pa}$ $\gamma = 1.4$ $Pr = 0.71$
<b>Porous domain</b>	$\Phi = 0.96$ $\alpha_\infty = 1.7$ $\sigma = 32 \cdot 10^3 \frac{\text{Ns}}{\text{m}^4}$ $\Lambda = 90 \cdot 10^{-6} \text{ m}$ $\Lambda' = 165 \cdot 10^{-6} \text{ m}$

**Table 3.4:** Material parameters of porous absorber.

To allow a comparison to the reference literature, the different formulations of the JCAM are compared using the respective value of the mean quadratic pressure in the cavity  $L_p$ :

$$L_p = 10 \log \frac{\int_{\Omega_a} p_a^2 d\Omega_a}{p_{\text{ref}}^2 \int_{\Omega_a} d\Omega_a}, \quad (3.111)$$

with  $p_{\text{ref}} = 20 \cdot 10^{-6}$  Pa as reference sound pressure in the air.

### 3.5.2 Analysis of the test cavity without absorber

In a first step, the course of the mean quadratic pressure in the cavity is computed for the case where no absorbers are installed. For this step, the area occupied by the porous absorber is replaced by an acoustic fluid. The result is given in figure 3.4. The peaks in the course of  $L_p$  can be attributed to the eigen-tones of the cavity.

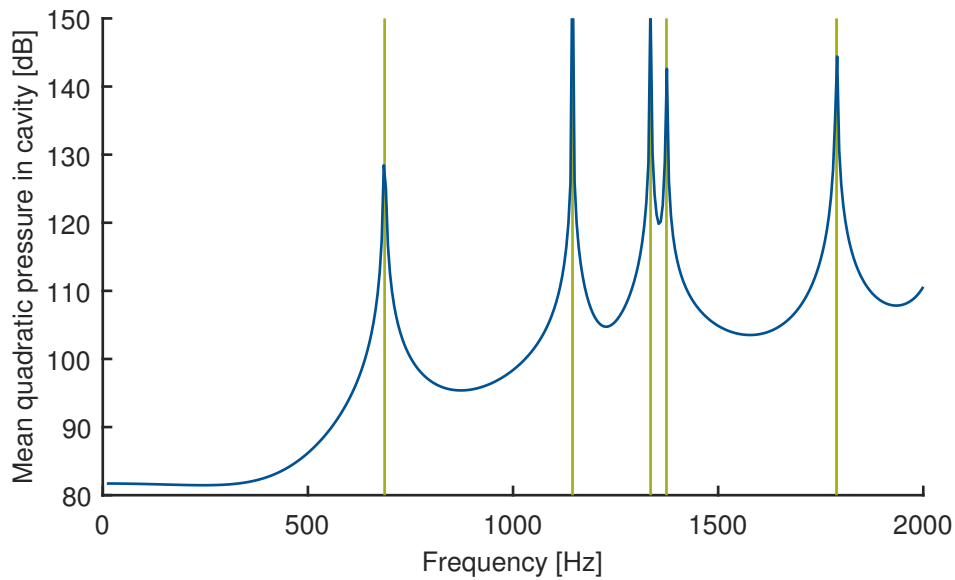


**Figure 3.4:** Mean quadratic pressure in cavity without porous absorber (—); (—) mark eigen-tones of acoustic cavity.

According to [Cremer and Müller 1982] the eigen-tones of a rectangular acoustic cavity with rigid boundaries are given by

$$f_{\text{room}} = \frac{c_{\text{air}}}{2} \sqrt{\left(\frac{n_x}{l_x}\right)^2 + \left(\frac{n_y}{l_y}\right)^2 + \left(\frac{n_z}{l_z}\right)^2}, \quad (3.112)$$

with the cavity's dimensions  $l_x$ ,  $l_y$  and  $l_z$ .  $c_{\text{air}}$  is the wave speed in the air. The individual eigen-tones correspond to different combinations of the counting variables  $n_x$ ,  $n_y$  and  $n_z$ . For the studied configuration  $l_x = 0.25$  m and  $l_y = 0.15$  m. As we consider a two-dimensional acoustic cavity, the contribution corresponding to the  $z$ -direction vanishes.

The analytical values of the eigen-tones of the studied cavity in the frequency range from 0 to 2000 Hz, determined using equation (3.112), are marked with green lines in figure 3.4.

They lie exactly in the peaks of the  $L_p$ -curve, which proves that the simulation outcome is plausible. As a supplement, figure 3.5 shows the distribution of the acoustic pressure within the cavity for the eigen-tones.

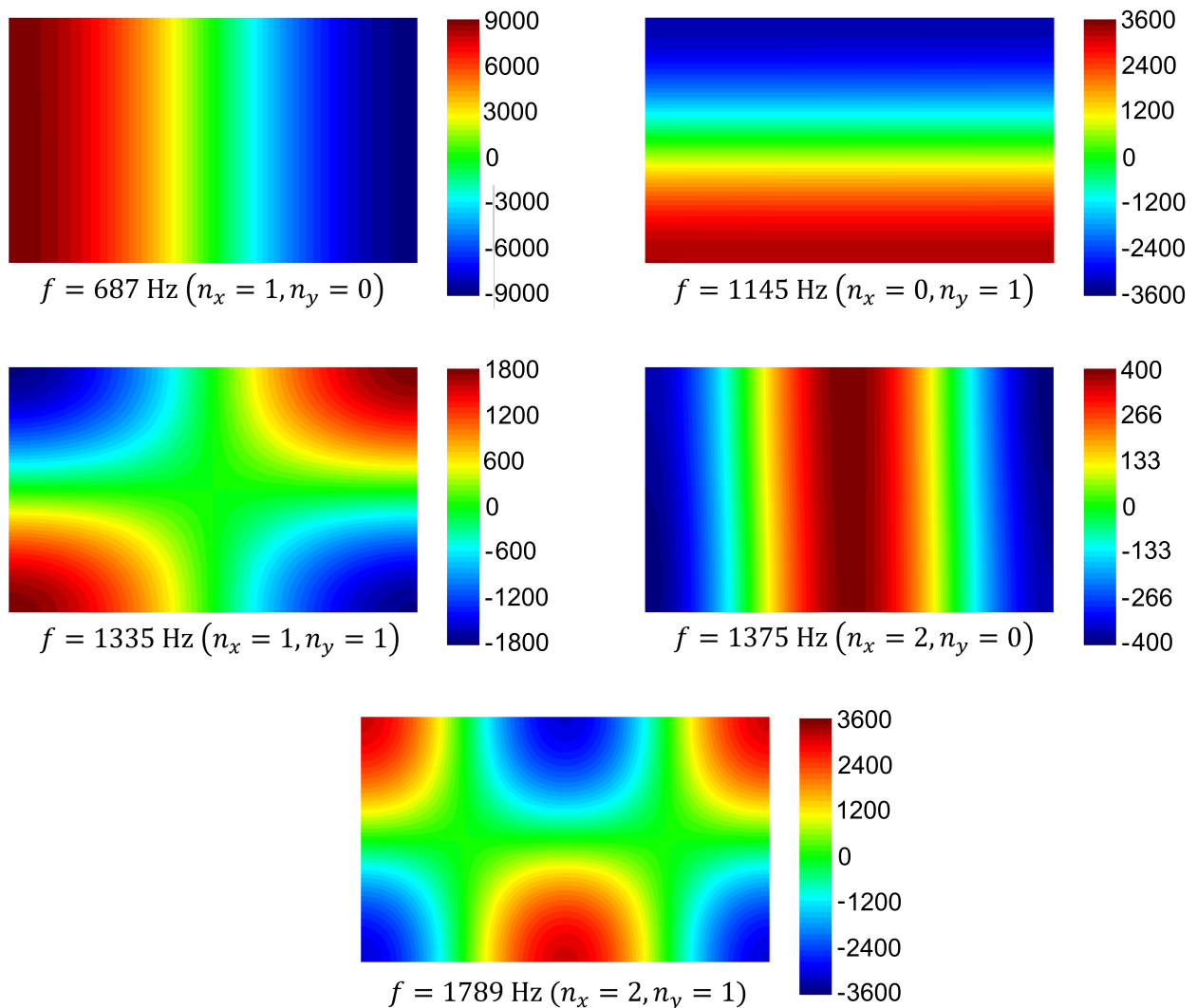
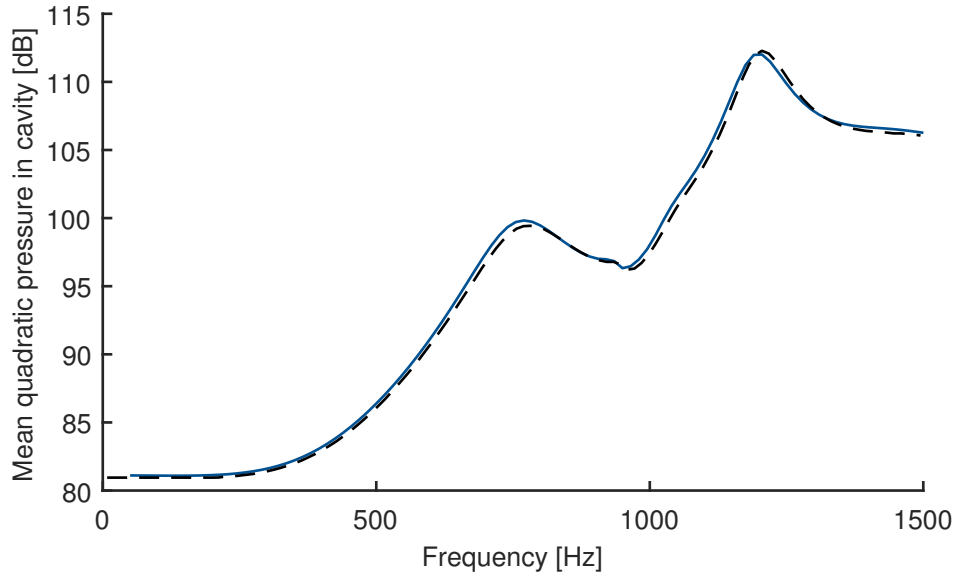


**Figure 3.5:** Pressure distribution within acoustic cavity for eigen-tones in frequency range from 0 to 2000 Hz.

### 3.5.3 Comparison with reference solution

The system with porous absorber along one edge is also studied in [Rumpler et al 2013]. Since [Rumpler et al 2013] evaluates the mean quadratic pressure in the cavity,  $L_p$  is also determined here and later serves as a reference variable for comparing the different formulations. As depicted in figure 3.6, the course of the mean quadratic pressure can be reproduced

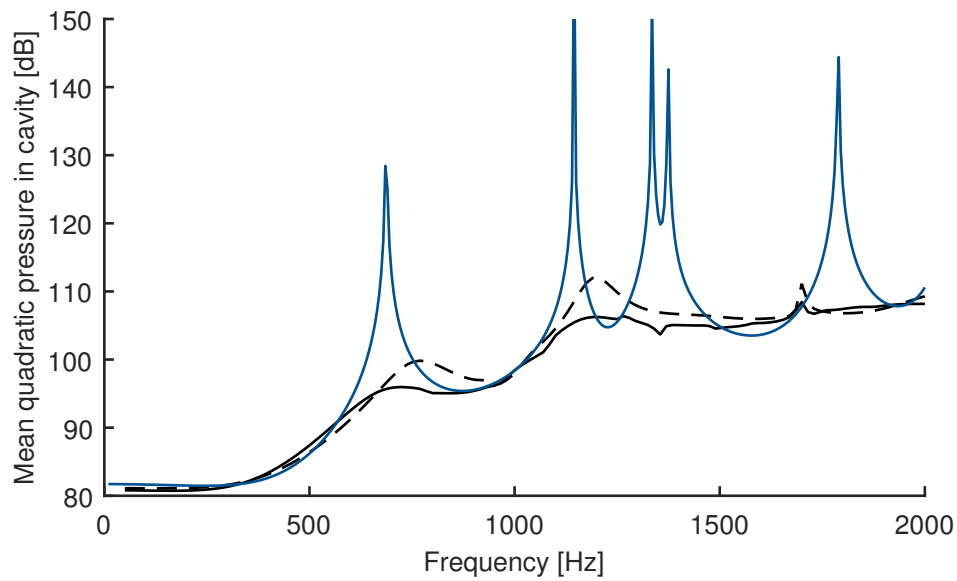
and thus the calculation results are considered plausible. Same as in the reference solution, the classical formulation is used to model the porous absorber.



**Figure 3.6:** Mean quadratic pressure in cavity with porous absorber at one edge (—) and reference solution given in [Rumpler et al 2013] (- - -); absorber is modelled using classical formulation.

### 3.5.4 Comparison of the different formulations

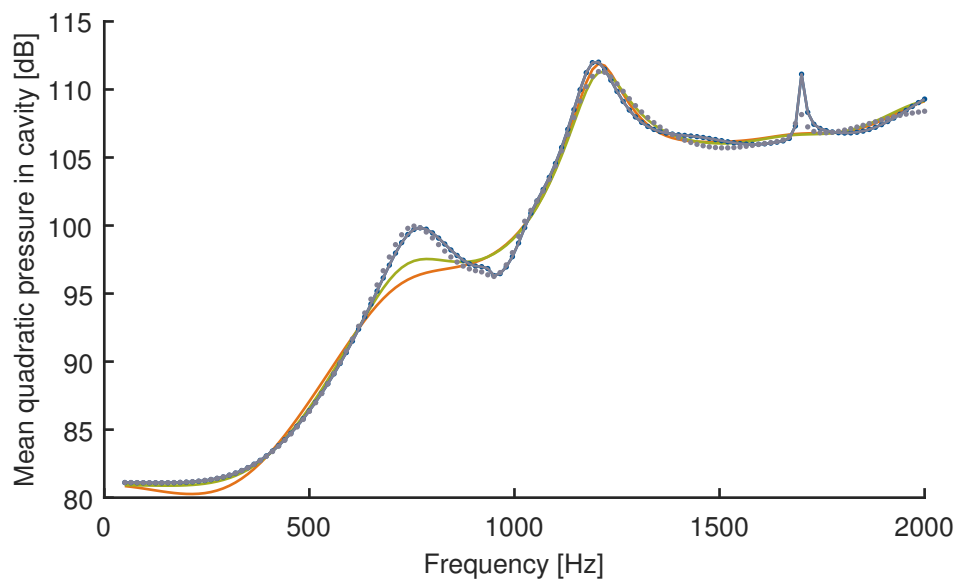
Now, the different formulations of the JCAM are compared using the two test configurations. In advance, the test configurations are compared with each other. Figure 3.7 shows the mean quadratic pressure in the cavity for the two test configurations. The porous absorber is modelled using the classical formulation. In addition to the test configurations, the case of the acoustic cavity without porous absorber is depicted. Here, the area occupied by the porous absorber is replaced by an acoustic fluid. We can see that especially the eigen-tones of the acoustic cavity (peaks in the respective  $L_p$ -curve) are damped by introducing porous absorbers. For the configuration with porous absorbers along two edges, the damping is enhanced in comparison to the case with a porous absorber at one edge.



**Figure 3.7:** Mean quadratic pressure in cavity without porous absorber (—), with porous absorber at one edge (- - -) and with porous absorber at two edges (—); absorbers are modelled using classical formulation.

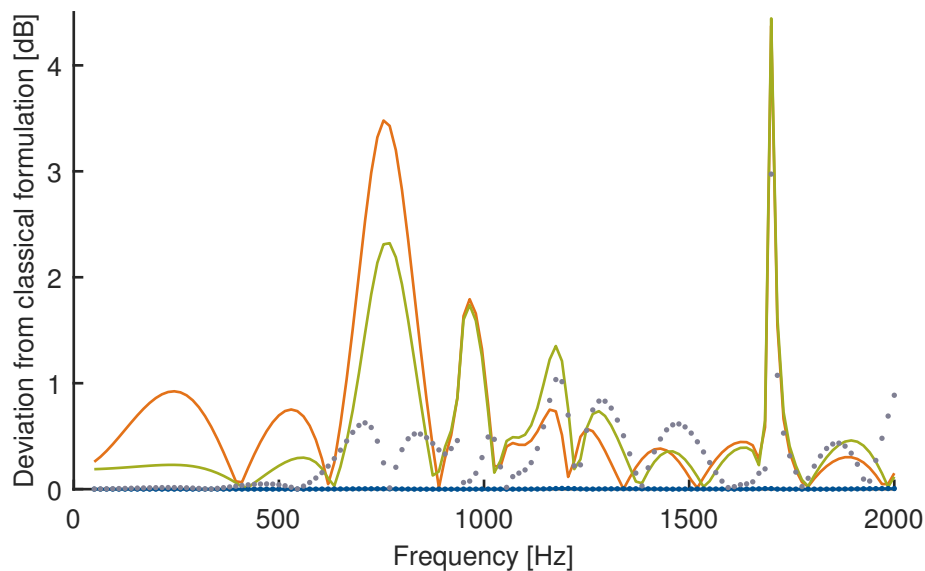
### Cavity with absorber at one edge

Figure 3.8 shows the mean quadratic pressure in the cavity corresponding to the studied formulations for the configuration with a porous absorber at one edge.



**Figure 3.8:** Mean quadratic pressure in cavity with porous absorber at one edge for classical formulation (—), reduced classical formulation (· · ·), mixed formulation (—), new mixed formulation (· · ·), rigid equivalent fluid (—) and limp equivalent fluid (—).

Figure 3.9 shows the absolute value of the deviation between the results obtained with the different formulations and the result obtained using the classical formulation, which is chosen to serve as reference result. The results corresponding to classical, mixed and new mixed formulation coincide. The reduced classical formulation provides good results especially for the frequency range below 550 Hz. Also for higher frequencies the course of  $L_p$  can be reproduced quite well. Larger deviations occur when using the rigid or limp equivalent fluid model. This shows that both the assumption of a rigid and a limp pore framework cannot accurately represent the behaviour of the elastic solid phase. Since the chosen support of the porous absorber does not allow for rigid body modes anyway, the limp equivalent fluid model cannot establish itself here compared to rigid equivalent fluid model.



**Figure 3.9:** For acoustic cavity with porous layer at one edge: deviation between  $L_p$  corresponding to classical formulation and reduced classical formulation ( $\cdots$ ), mixed formulation ( $-$ ), new mixed formulation ( $\cdots$ ), rigid equivalent fluid ( $-$ ), limp equivalent fluid ( $-$ ).

In particular, at the frequencies at which fluid and solid displacements are of similar scale, the equivalent fluid models differ from the other formulations. As shown in figure 3.10, this is the case for an excitation frequency of 1700 Hz, where the largest deviation between multiphase and equivalent fluid models occurs. If in this case the elastic deformation of the solid is not mapped, also the displacement pattern in the fluid cannot be reproduced, which explains the deviation between the equivalent fluid models and the other formulations.

If, on the other hand, the fluid displacements are significantly larger than those of the pore framework, the agreement between multiphase models and equivalent fluid models is quite



good. This is the case for an excitation frequency of 1530 Hz. Figure 3.11 proves that here the fluid motion dominates the displacement pattern within the absorber.

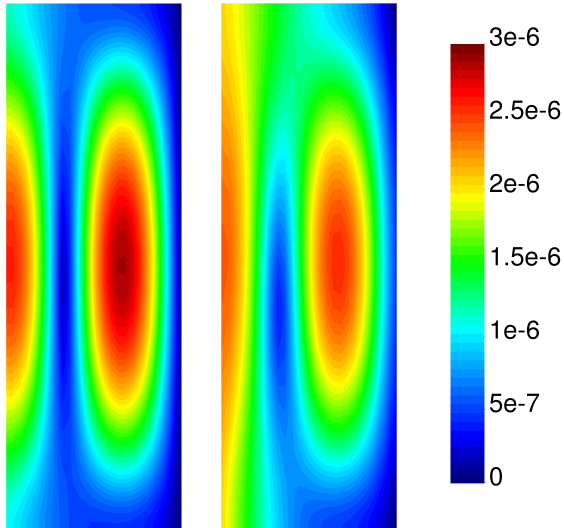


**Figure 3.10:** Deformation of absorber at 1700 Hz; left: displacement of solid phase of porous absorber; right: displacement of fluid phase of porous absorber.

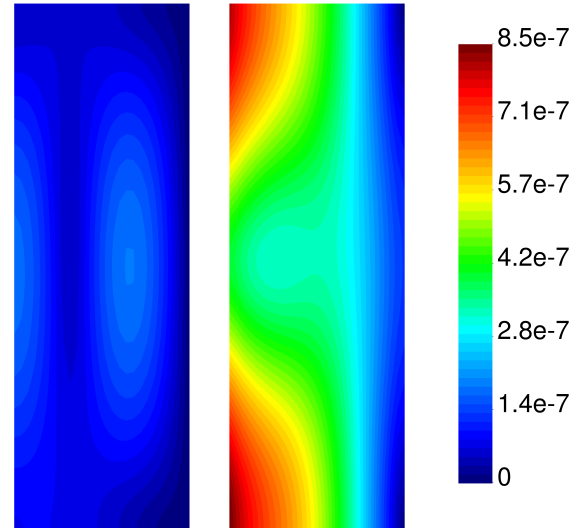


**Figure 3.11:** Deformation of absorber at 1530 Hz; left: displacement of solid phase of porous absorber; right: displacement of fluid phase of porous absorber.

### Cavity with absorbers at two edges

Figure 3.12 depicts the course of  $L_p$  corresponding to the studied formulations for the configuration where porous absorbers are mounted along two edges of the acoustic cavity. Figure 3.13 gives the deviation between the classical formulation and the other ones. The result is consistent with the observations made on the example with the acoustic cavity and a porous absorber along one edge. The small mismatch between classical formulation and coinciding mixed and new mixed formulation can be attributed to numerical inaccuracies. The negligible deviation was to be expected, since it can also be observed in the comparison between mixed and classical formulation made in [Atalla et al 1998], where the mixed formulation in the form used here is introduced. In comparison to the case with porous absorber at one edge, the upper limit for the excitation frequency up to which the reduced classical formulation almost coincides with the reference solution is lower and corresponds to about 500 Hz. This observation can be attributed to the higher complexity of the second application case.

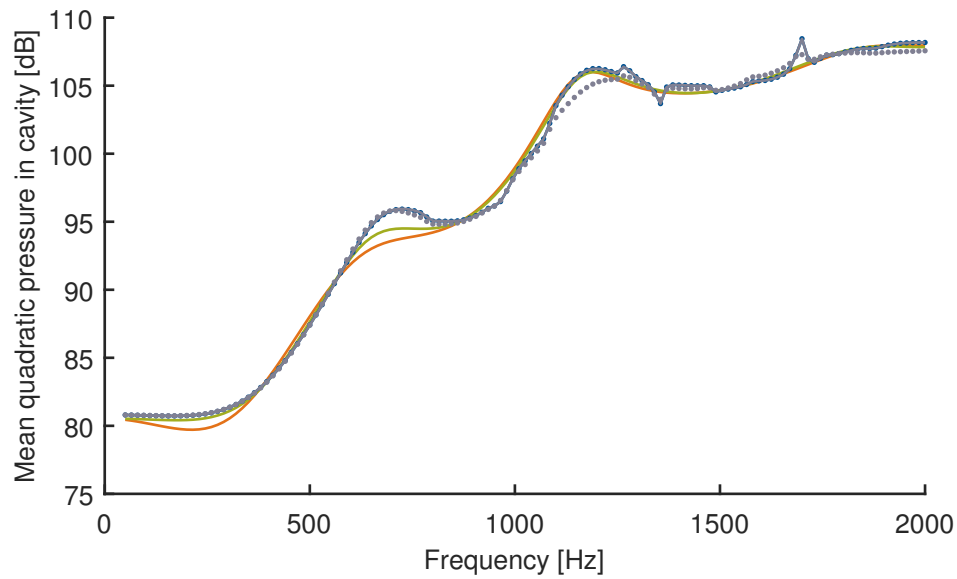


**Figure 3.12:** Mean quadratic pressure in cavity with porous absorbers at two edges for classical formulation (—), reduced classical formulation (· · ·), mixed formulation (—), new mixed formulation (· · ·), rigid equivalent fluid (—) and limp equivalent fluid (—).

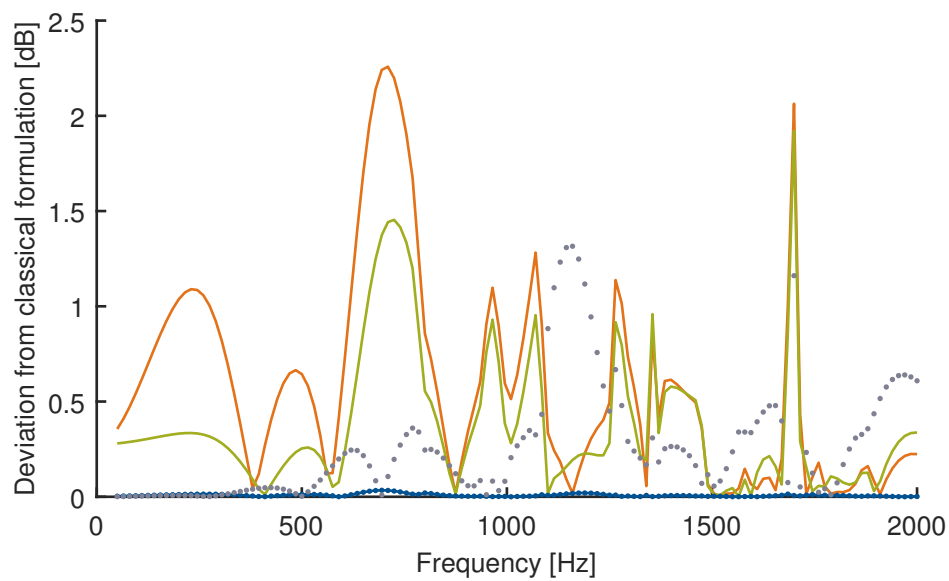


**Figure 3.13:** For acoustic cavity with porous layers at two edges: deviation between  $L_p$  corresponding to classical formulation and reduced classical formulation (· · ·), mixed formulation (—), new mixed formulation (· · ·), rigid equivalent fluid (—), limp equivalent fluid (—).

### 3.5.5 Evaluation of the approximation error introduced by the reduced classical formulation

The results obtained with the reduced classical formulation are now to be examined in more detail. Therefore, the error introduced by the linearisation of  $\tilde{K}_f$  and  $\tilde{b}$  is studied for the given material parameters. Figures 3.14 and 3.15 show the error introduced by the linearisation of the equivalent bulk modulus of the fluid phase and the viscous drag. Thereby the deviation of the linearised variable  $a^*$  compared to the correct value  $a$  is computed via  $\frac{\Re(a) - \Re(a^*)}{\Re(a)}$  for the real part, via  $\frac{\Im(a) - \Im(a^*)}{\Im(a)}$  for the imaginary part and via  $\frac{|a| - |a^*|}{|a|}$  for the absolute value.

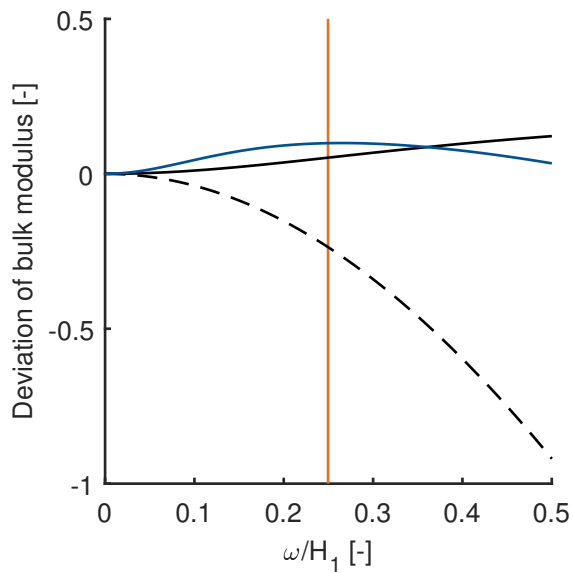


**Figure 3.14:** Deviation of linearised equivalent bulk modulus from exact solution: real part (—), imaginary part (---) and absolute value (—); (—) marks dimensionless frequency ratio for  $f = 500$  Hz.

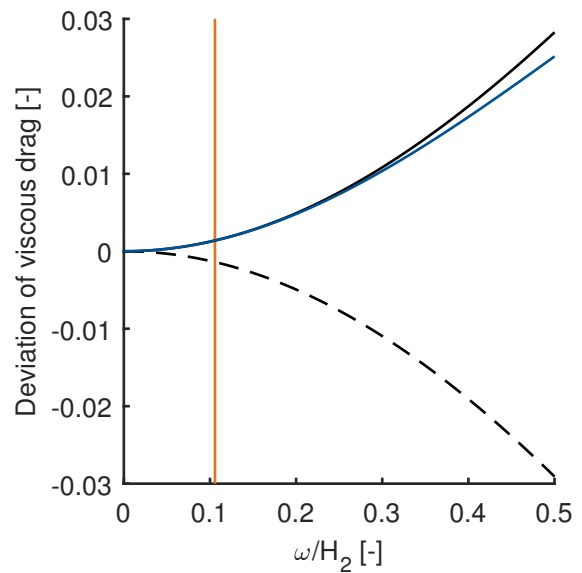


**Figure 3.15:** Deviation of linearised viscous drag from exact solution: real part (—), imaginary part (---) and absolute value (—); (—) marks dimensionless frequency ratio for  $f = 500$  Hz.

The approximation error introduced by linearising  $\tilde{K}_f$  is higher than for the linearisation of  $\tilde{b}$ . We can also see that for the bulk modulus the deviation from the exact value is bigger for the imaginary part than for the real part. From the fact that the deviation of the absolute value is of the same magnitude as the deviation of the real part, it can be concluded that the real part of both bulk modulus and viscous drag is bigger than the imaginary part. Within figures 3.14 and 3.15 an orange line marks the value of the respective material dependent dimensionless frequency ratio for  $f = 500$  Hz. For the test configurations investigated, the reduced classical formulation almost coincides with the reference solution below this upper

frequency limit. For frequencies higher than 500 Hz, the linearised parameters deviate more strongly from the exact ones, which is reflected in a poorer agreement of the calculation results. A frequency of 500 Hz corresponds to  $\frac{\omega}{H_1} = 0.25$  and  $\frac{\omega}{H_2} = 0.11$ .  $H_1$  and  $H_2$  are material dependent parameters which are defined in equations (3.46) and (3.47). [Panneton and Atalla 1997] observe a good approximation to the reference solution for  $\frac{\omega}{H_1} \ll 1 \cap \frac{\omega}{H_2} \ll 1$ , which is consistent with the observations made in the context of this thesis.

### 3.5.6 Summary

The following conclusions are drawn from the comparison of the formulations conducted above:

- The difference between the results obtained with the classical formulation and the mixed formulation is negligible.
- The classical formulation involves more DOFs than the mixed formulation and leads to larger systems of equations. This disadvantage can be compensated, depending on the application, by the fact that the classical formulation leads, compared to the mixed formulation, to symmetric system matrices.
- Since the coupling between the mixed formulation and the acoustic fluid is natural, for the configurations considered a lower coupling effort is involved for the mixed formulation compared to the classical formulation.
- The mixed and the new mixed formulation lead to the same result, but the coupling effort for the new mixed formulation is higher for the considered configurations.
- Especially for low frequencies the reduced classical formulation is a good alternative. For the studied configurations it performs best for  $\frac{\omega}{H_1} < 0.25 \cap \frac{\omega}{H_2} < 0.11$ , whereby  $H_1$  and  $H_2$  are material dependent parameters. The advantage here is that the system matrices do not have to be recalculated for each frequency considered. For the mixed formulation no comparably simple reduced form can be derived.
- For the considered configurations neither the limp nor the rigid equivalent fluid model is able to approach the elastic behaviour of the solid phase accurately. They only provide a rough approximation of the result obtained with the classical formulation.

## 3.6 Conclusion

This chapter introduces the JCAM for modelling porous absorbers. Besides the classical formulation, which uses the displacements of fluid and solid phase as DOFs, two different variants of the mixed formulation, in which the pore pressure serves as unknown instead of the fluid displacements, are explained. In addition, a reduced version of the classical formulation for application in the low-frequency range is presented. It has the advantage that the system matrices do not have to be recalculated for each frequency considered. Further, two equivalent fluid models are shown, one assuming a rigid and the other one a limp pore framework. It is explained how FEM formulations for porous media can be derived from the different formulations. In addition, the relevant boundary and coupling conditions of porous media modelled according to the different formulations and their implementation into a FEM model are treated in detail. Finally, the different formulations are compared on two test configurations.

## 4 Modelling strategies for periodic structures

### 4.1 Introduction

The geometry of the metamaterials that are investigated in the context of this thesis is periodic. Since the structure is finite in reality, theoretically the edges of the metamaterial need to be modelled as well. From a certain dimension, however, an infinitely periodic structure can be assumed and boundary effects can be neglected. This chapter deals with the efficient representation of infinitely extended periodic structures. The wave propagation along the structure and also the wave transmission through the structure is considered. The derivations in this chapter refer to two-dimensional problems with one-dimensional periodicity, but can easily be extended for three-dimensional applications with two- or three-dimensional periodicity.

### 4.2 Basic theory

Using the Wave Finite Element Method (WFEM) periodic structures can be analysed based on a FEM model of one single repetitive section also termed unit cell. The periodicity is introduced via specific coupling conditions at the cell boundaries. The characteristics of those coupling conditions emerge from the so called Bloch Theorem (see section 4.2.3).

The method dates back to [Brillouin 1946] and was enhanced by [Mead 1973; Orris and Petyt 1974; Langley 1993; Mace et al 2005]. [Duhamel et al 2006] extends the method for mapping also finite systems. Besides studying the free wave propagation along periodic structures, the response of finite structures due to spatially limited loads [Duhamel et al 2006] and the sound transmission through the structure [Yang et al 2017; Errico et al 2019] can be examined. [Serra et al 2015] applies the WFEM for analysing elastic frame porous

structures. According to [Zhou et al 2015; Van Belle et al 2020], the efficiency of the method can be further enhanced by embedding model order reduction strategies like the Component Mode Synthesis (CMS). The CMS itself was introduced by [Hurty 1960] and is most often used in the version given in [Craig Jr and Bampton 1968]. The sensitivity of the WFEM towards numerical errors is analysed in [Mace and Manconi 2008; Waki et al 2009].

### 4.2.1 Selection of the unit cell

When studying periodic structures using the WFEM, the unit cell of the structure has to be specified. The unit cell generally corresponds to the smallest possible section whose sequencing results in the periodic structure. Often there are several possibilities to choose the unit cell.

Figure 4.1 shows three different unit cells which, when horizontally strung together, all correspond to the same periodic structure. While the first two unit cells could be used as an input for a WFEM analysis, the third unit cell is not a valid choice as, after discretisation, not every right boundary node will have a corresponding left boundary node. Taking reference to [Zhou et al 2015], for most approaches of the WFEM the second unit cell enables a more efficient analysis than the first one does. This is because by using the same discretisation, the number of boundary nodes in the first cell is higher than in the second one. As shown in the following sections, the computation effort is, for most of the evaluation schemes, mainly influenced by the number of boundary nodes.

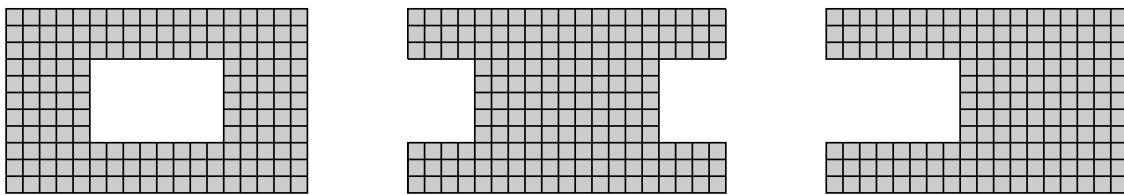


Figure 4.1: Selection of optimal unit cell.

### 4.2.2 Characterization of the unit cell

Without applying the periodicity conditions yet, the cell itself can be characterized by the equation of motion under steady state harmonic loading with a frequency of  $\omega$ , which is given in equation (2.1). The matrices  $\mathbf{K}$ ,  $\mathbf{C}$  and  $\mathbf{M}$  contained therein can be derived using any standard FEM implementation. The unit cell can be of complex shape and material composition. In the scope of this thesis, it is required that number and vertical position of

the nodes at the left and right boundary of the cell coincide. The entries of the right hand side vector  $\mathbf{f}$  depend on the respective application case.

[Collet et al 2011; Magliacano et al 2020] propose a novel method termed shift cell operator technique instead of the conventional WFEM approach. Here, the periodicity is integrated into the element formulation of the elements of which the unit cell is composed. Although it can be shown that this approach results in a reduction of the computational effort compared to the conventional WFEM, the disadvantage arises that the unit cell cannot be represented using a standard FEM implementation. Therefore, the conventional WFEM is used in the context of this work.

### 4.2.3 Introduction of the periodicity

The periodicity of the structure is described using the Bloch Theorem, which is also known as Floquet theorem. Originally applied to problems in the field of quantum mechanics [Bloch 1929], the theoretical considerations can be transferred to structural dynamics. It states that the response function of a periodic structure is given by the response function of a single unit cell and an exponential term which describes the change in amplitude and phase as the waves travel from one cell to the next. Thereby the relative change in amplitude and phase between adjacent cells does not depend on the position of these cells within the periodic structure [Brillouin 1946]. The relation between the response functions of two adjacent cells can be expressed as

$$\mathbf{q}(x + L_x) = \mathbf{q}(x)\mu = \mathbf{q}(x)e^{-i\kappa L_x}; \quad (4.1)$$

with  $\mathbf{q}$  depicting the degrees of freedom of the unit cell.  $L_x$  is the length of the unit cell and  $\mu$  the propagation constant. The wavenumber  $\kappa$  is a complex unity and can be expressed as  $\kappa = \kappa_r + i\kappa_i$ . Depending on the value of  $\kappa$ , the exponential term can be assigned to three different propagation characteristics. While  $\kappa_i = 0$  results in undamped waves,  $\kappa_r = 0$  corresponds to evanescent waves, being near fields that do not undergo any spatial oscillation but decay straight away. Damped oscillating waves, termed as attenuating waves, occur if both  $\kappa_i \neq 0$  and  $\kappa_r \neq 0$ . The different types of waves are shown in figure 4.2. While the propagation characteristics of the waves are determined by the absolute values of  $\kappa_r$  and  $\kappa_i$ , the sign of  $\kappa_r$  and  $\kappa_i$  determines the propagation direction.



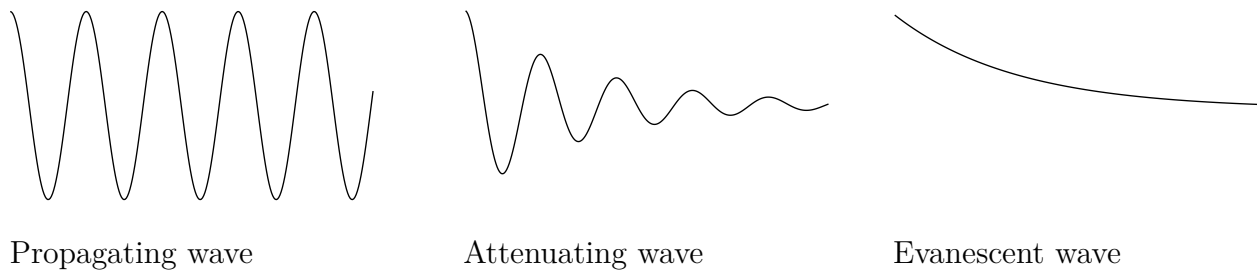


**Figure 4.2:** Distinction of waves regarding to their propagation characteristics.

## 4.3 Wave propagation along the structure

In certain application cases, it is necessary to investigate what kind of waves propagate along the structure in a given frequency range. As already introduced, specific unit cell designs can lead to stop bands being frequency ranges where no undamped waves propagate along the structure. To exploit this property in the design of vibroacoustic systems, it is necessary to compute the location of these stop bands. Depending on the sought complexity of the result, two different approaches are possible. Both approaches and also the considered types of problems are specified in this section.

### 4.3.1 Problem description

The considered system is a periodic metamaterial as exemplarily shown in figure 4.3. The cell is two-dimensional and can have almost any material composition and geometry. The structure is periodic with respect to the  $x$ -direction.

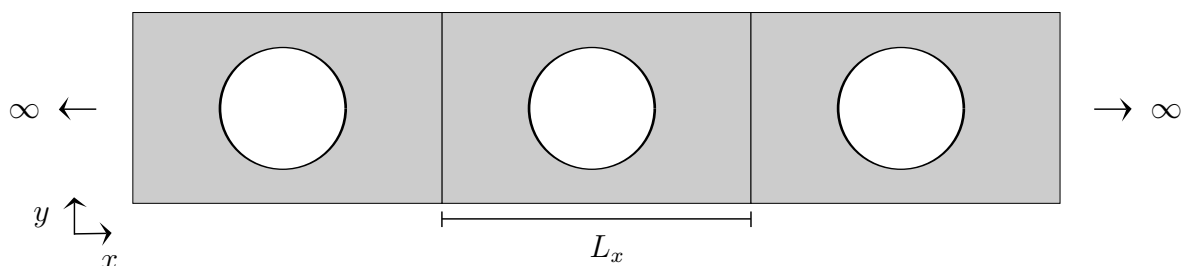


**Figure 4.3:** Periodic metamaterial.

The nodes of the unit cell model are subsequently distinguished into nodes at the left and right coupling interface and internal nodes using the indices  $\square_L$ ,  $\square_R$  and  $\square_I$ .

### 4.3.2 Inverse approach

One common approach of the WFEM is called inverse approach. It derives the dispersion characteristics of periodic structures solving for the frequency at a given wavenumber. Using this approach, only undamped waves are taken into account. This way, stop bands can be detected easily. However, no conclusions can be drawn about the wave characteristics within the stop bands.

In the context of this work, we assume that there is no damping within the material when carrying out analyses using the inverse approach. Considering only propagating waves,  $\kappa_i$  vanishes and the propagation constant can be simplified:

$$\mu = e^{-i\kappa_r L_x}. \quad (4.2)$$

Using the Bloch Theorem, we can find the following relation between DOFs and right hand side contributions at the left and right boundary of the unit cell:

$$\mathbf{u}_R = \mu \mathbf{u}_L, \quad (4.3)$$

$$\mathbf{f}_R = -\mu \mathbf{f}_L. \quad (4.4)$$

Inserting equation (4.3) and (4.4) into equation (2.1) and assuming that the internal nodes are not loaded by external forces ( $\mathbf{f}_I = \mathbf{0}$ ), we can derive the following eigenvalue problem:

$$(\mathbf{K}^{\text{red}} - \omega^2 \mathbf{M}^{\text{red}}) \mathbf{u}^{\text{red}} = \mathbf{0}, \quad (4.5)$$

with  $\mathbf{K}^{\text{red}} = \mathbf{R}^H \mathbf{K} \mathbf{R}$ ,  $\mathbf{M}^{\text{red}} = \mathbf{R}^H \mathbf{M} \mathbf{R}$  and  $\mathbf{u}^{\text{red}} = [\mathbf{u}_L \ \mathbf{u}_I]^\top$ . The reduction matrix  $\mathbf{R}$  is defined as

$$\mathbf{R} = \begin{bmatrix} \mathbf{I} & \mathbf{0} \\ \mathbf{0} & \mathbf{I} \\ \mu \mathbf{I} & \mathbf{0} \end{bmatrix}, \quad (4.6)$$

where  $\mathbf{I}$  is the identity matrix. The superscript  $\square^H$  marks the complex conjugate transpose of a matrix. Equation (4.5) is solved for the frequency at a given wavenumber.

As the elemental matrices corresponding to porous media usually are frequency dependent, the inverse approach does not depict an appropriate method to study the dispersion characteristics of periodic structures with porous components. An exception to this arises when

the porous materials are modelled on the basis of equation (3.48) using the reduced classical formulation, i.e. when the frequency dependence of the model parameters for the porous domain is strongly simplified.

### 4.3.3 Direct approach

Contrary to the inverse approach, the direct approach takes all kind of waves into consideration. Here, an eigenvalue problem is derived which is solved for the wavenumber for a given frequency.

Introducing the dynamic stiffness matrix  $\mathbf{D} = \mathbf{K} + i\omega\mathbf{C} - \omega^2\mathbf{M}$ , we can reformulate equation (2.1):

$$\begin{bmatrix} \mathbf{D}_{LL} & \mathbf{D}_{LR} & \mathbf{D}_{LI} \\ \mathbf{D}_{RL} & \mathbf{D}_{RR} & \mathbf{D}_{RI} \\ \mathbf{D}_{IL} & \mathbf{D}_{IR} & \mathbf{D}_{II} \end{bmatrix} \begin{bmatrix} \mathbf{q}_L \\ \mathbf{q}_R \\ \mathbf{q}_I \end{bmatrix} = \begin{bmatrix} \mathbf{f}_L \\ \mathbf{f}_R \\ \mathbf{f}_I \end{bmatrix} = \begin{bmatrix} \mathbf{f}_L \\ \mathbf{f}_R \\ \mathbf{0} \end{bmatrix}. \quad (4.7)$$

The fact that the internal nodes are not loaded by external forces ( $\mathbf{f}_I = \mathbf{0}$ ) allows us to condense the internal DOFs from the system of equations:

$$\begin{bmatrix} \hat{\mathbf{D}}_{LL} & \hat{\mathbf{D}}_{LR} \\ \hat{\mathbf{D}}_{RL} & \hat{\mathbf{D}}_{RR} \end{bmatrix} \begin{bmatrix} \mathbf{q}_L \\ \mathbf{q}_R \end{bmatrix} = \begin{bmatrix} \mathbf{f}_L \\ \mathbf{f}_R \end{bmatrix}, \quad (4.8)$$

with

$$\hat{\mathbf{D}}_{LL} = \mathbf{D}_{LL} - \mathbf{D}_{LI}\mathbf{D}_{II}^{-1}\mathbf{D}_{IL}, \quad (4.9a)$$

$$\hat{\mathbf{D}}_{LR} = \mathbf{D}_{LR} - \mathbf{D}_{LI}\mathbf{D}_{II}^{-1}\mathbf{D}_{IR}, \quad (4.9b)$$

$$\hat{\mathbf{D}}_{RL} = \mathbf{D}_{RL} - \mathbf{D}_{RI}\mathbf{D}_{II}^{-1}\mathbf{D}_{IL}, \quad (4.9c)$$

$$\hat{\mathbf{D}}_{RR} = \mathbf{D}_{RR} - \mathbf{D}_{RI}\mathbf{D}_{II}^{-1}\mathbf{D}_{IR}. \quad (4.9d)$$

Using equation (4.3) and (4.4) and requiring the continuity of displacements and equilibrium of forces at the interface between two adjacent cells, we can derive the following eigenvalue problem:

$$\mathbf{T} \begin{bmatrix} \mathbf{q}_L \\ \mathbf{f}_L \end{bmatrix} = \mu \begin{bmatrix} \mathbf{q}_L \\ \mathbf{f}_L \end{bmatrix}; \quad (4.10)$$

the transfer matrix  $\mathbf{T}$  is given as

$$\mathbf{T} = \begin{bmatrix} -\hat{\mathbf{D}}_{\text{LR}}^{-1}\hat{\mathbf{D}}_{\text{LL}} & \hat{\mathbf{D}}_{\text{LR}}^{-1} \\ -\hat{\mathbf{D}}_{\text{RL}} + \hat{\mathbf{D}}_{\text{RR}}\hat{\mathbf{D}}_{\text{LR}}^{-1}\hat{\mathbf{D}}_{\text{LL}} & -\hat{\mathbf{D}}_{\text{RR}}\hat{\mathbf{D}}_{\text{LR}}^{-1} \end{bmatrix}. \quad (4.11)$$

As the orders of magnitude of DOFs and right hand side contributions vary considerably, the transfer matrix might suffer from ill conditioning issues. Options to solve this problem are given in [Zhong and Williams 1995] and [Duhamel et al 2006].

The direct approach is also applicable to periodic structures with porous components. However, it should be noted that without applying a simplification on the frequency dependency of the material parameters, the system matrices must be recalculated for each frequency of investigation and, depending on the chosen formulation, may not be symmetric.

## 4.4 Sound transmission through the structure

Within more recent contributions, the WFEM is employed to evaluate the sound transmission through periodic structures. While [Yang et al 2017; Errico et al 2019] already used the WFEM to compute the sound transmission through complex three-dimensional panels, to the knowledge of the author the method hasn't been used yet for elastic frame porous panels modelled by the classical formulation of the JCAM.

The approaches in section 4.3 investigate what kind of waves evolve along a two-dimensional structure with one-dimensional periodicity. For this purpose, eigenvalue problems were solved either for the frequency for known wavenumbers, or for the wavenumbers under specification of the frequency. The theory behind does not require any certain relation between the wavelength of the determinable wave solutions and the dimensions of the unit cell. In comparison, no eigenvalue problems are solved in the scope of section 4.4. Here, the deformation of the structure under a given load, which is defined by its amplitude and wavenumber, is determined. From this, the absorption, reflection and transmission coefficients are computed. Similar to section 4.3, it is not necessary that the wavelength of the excitation has a certain relation to the dimensions of the unit cell.

After introducing the two-dimensional system of observation, this section summarizes how the sound transmission through non porous and also porous structures can be computed using the WFEM.

### 4.4.1 Problem description

The system of observation is a two-dimensional periodic structure of arbitrary material composition as shown in figure 4.4. A semi-infinite acoustic fluid is coupled to the top and bottom of the structure.

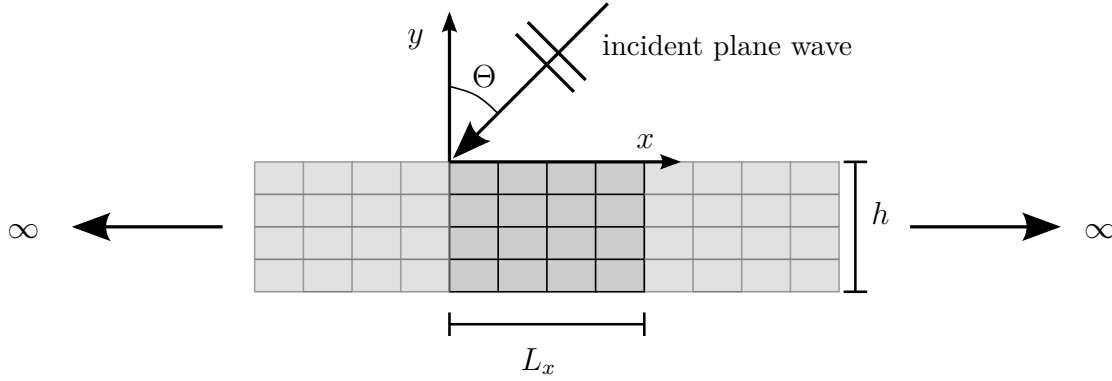


**Figure 4.4:** Periodic metamaterial with incident inclined plane wave.

The structure is excited by an inclined plane wave. Depending on the investigated structure, parts of the incident wave are reflected, transmitted and absorbed. For a time harmonic excitation, the functions of incident, reflected and transmitted wave are given in the frequency domain as

$$p_i(x,y) = p_i e^{i(-k_x x + k_y y)}, \quad (4.12)$$

$$p_r(x,y) = p_r e^{i(-k_x x - k_y y)}, \quad (4.13)$$

$$p_t(x,y) = p_t e^{i(-k_x x + k_y y)}. \quad (4.14)$$

$k_x$  and  $k_y$  are the wavenumbers in  $x$ - and  $y$ - direction and can be derived from the properties of the semi-infinite acoustic fluid and the inclination  $\Theta$  of the incident wave by decomposing the wavenumber  $k$ :

$$k = \omega \sqrt{\frac{\rho_a}{E_a}} \quad (4.15)$$

$$k_x = k \sin(\Theta) \quad (4.16)$$

$$k_y = \sqrt{k^2 - k_x^2} \quad (4.17)$$

The pressure field in the upper fluid domain is composed of the incident and reflected wave and given as  $-(p_i(x,y) + p_r(x,y))$ . The pressure field in the lower fluid is  $p_t(x,y)$ . We can

compute the pressure field at the metamaterials top  $p_a(x,0)$  and bottom  $p_a(x, -h)$  as

$$p_a(x,0) = -(p_i(x,0) + p_r(x,0)) = -(p_i + p_r) e^{-ik_x x}, \quad (4.18)$$

$$p_a(x, -h) = p_t(x, -h) = p_t e^{i(-k_x x - k_y h)}, \quad (4.19)$$

where  $h$  is the thickness of the periodic structure.

The aim of the solution strategies proposed below is to determine the reflected and transmitted part of the incident wave (i.e.  $p_r$  and  $p_t$  for a given value of  $p_i$ ). The strategies apply for periodic structures of constant thickness, but can be extended for structures with thickness variations.

#### 4.4.2 General pre-processing

This section contains the pre-processing necessary to calculate the sound transmission loss through a structure using the WFEM, regardless of whether the boundary layers are porous or not. Following the steps summarized here, it is shown how the excitation by an inclined plane wave and the coupling to the semi-infinite acoustic domains are introduced into the modelling process. The corresponding steps depend on the material of the boundary layers.

##### Presorting the system of equations

Similar to section 4.3, the periodic structure is modelled using the WFEM. The unit cell is again characterized by its equation of motion under steady state harmonic loading. The DOFs are now distinguished into DOFs corresponding to left  $\square_L$ , right  $\square_R$ , upper and lower boundary  $\square_B$  and internal  $\square_I$  nodes, leading to the following representation:

$$\begin{bmatrix} \mathbf{D}_{LL} & \mathbf{D}_{LR} & \mathbf{D}_{LB} & \mathbf{D}_{LI} \\ \mathbf{D}_{RL} & \mathbf{D}_{RR} & \mathbf{D}_{RB} & \mathbf{D}_{RI} \\ \mathbf{D}_{BL} & \mathbf{D}_{BR} & \mathbf{D}_{BB} & \mathbf{D}_{BI} \\ \mathbf{D}_{IL} & \mathbf{D}_{IR} & \mathbf{D}_{IB} & \mathbf{D}_{II} \end{bmatrix} \begin{bmatrix} \mathbf{q}_L \\ \mathbf{q}_R \\ \mathbf{q}_B \\ \mathbf{q}_I \end{bmatrix} = \begin{bmatrix} \mathbf{f}_L \\ \mathbf{f}_R \\ \mathbf{f}_B \\ \mathbf{f}_I \end{bmatrix} + \begin{bmatrix} \mathbf{e}_L \\ \mathbf{e}_R \\ \mathbf{e}_B \\ \mathbf{e}_I \end{bmatrix}, \quad (4.20)$$

whereby the right hand side is split up into internal reactions  $\mathbf{f}$  and excitations  $\mathbf{e}$ . The corner nodes are assigned to the left and right nodes, but require special treatment as the excitation and coupling to the fluid domain needs to be considered in addition to the periodicity conditions.

In analogy to section 4.3.3, the unloaded internal DOFs ( $\mathbf{f}_I, \mathbf{e}_I = 0$ ) can be condensed from the system of equations:

$$\underbrace{\begin{bmatrix} \hat{\mathbf{D}}_{LL} & \hat{\mathbf{D}}_{LR} & \hat{\mathbf{D}}_{LB} \\ \hat{\mathbf{D}}_{RL} & \hat{\mathbf{D}}_{RR} & \hat{\mathbf{D}}_{BB} \\ \hat{\mathbf{D}}_{BL} & \hat{\mathbf{D}}_{BR} & \hat{\mathbf{D}}_{BB} \end{bmatrix}}_{\hat{\mathbf{D}}} \begin{bmatrix} \mathbf{q}_L \\ \mathbf{q}_R \\ \mathbf{q}_B \end{bmatrix} = \begin{bmatrix} \mathbf{f}_L \\ \mathbf{f}_R \\ \mathbf{0} \end{bmatrix} + \begin{bmatrix} \mathbf{e}_L \\ \mathbf{e}_R \\ \mathbf{e}_B \end{bmatrix}. \quad (4.21)$$

In equation (4.21), also the internal reactions corresponding to the top and bottom nodes are assumed to vanish ( $\mathbf{f}_B = 0$ ).

### Application of the Bloch Theorem

Applying Bloch's theorem according to equations (4.3) and (4.4), we can further condense the system of equations:

$$\Lambda_L \begin{bmatrix} \hat{\mathbf{D}}_{LL} & \hat{\mathbf{D}}_{LR} & \hat{\mathbf{D}}_{LB} \\ \hat{\mathbf{D}}_{RL} & \hat{\mathbf{D}}_{RR} & \hat{\mathbf{D}}_{BB} \\ \hat{\mathbf{D}}_{BL} & \hat{\mathbf{D}}_{BR} & \hat{\mathbf{D}}_{BB} \end{bmatrix} \Lambda_R \begin{bmatrix} \mathbf{q}_L \\ \mathbf{q}_B \end{bmatrix} = \Lambda_L \begin{bmatrix} \mathbf{e}_L \\ \mathbf{e}_R \\ \mathbf{e}_B \end{bmatrix}, \quad (4.22)$$

with

$$\Lambda_L = \begin{bmatrix} \mathbf{I} & \frac{1}{\mu}\mathbf{I} & \mathbf{0} \\ \mathbf{0} & \mathbf{0} & \mathbf{I} \end{bmatrix} \quad (4.23)$$

and

$$\Lambda_R = \begin{bmatrix} \mathbf{I} & \mathbf{0} \\ \mu\mathbf{I} & \mathbf{0} \\ \mathbf{0} & \mathbf{I} \end{bmatrix}. \quad (4.24)$$

The excitation vector  $\mathbf{e}$  maps the excitation and the coupling to the fluid domain. Its entries depend on whether the boundary layers are linear elastic or porous and will be specified in the following sections.

### 4.4.3 Linear elastic boundary layers

First, the top and bottom layer of the periodic structure are assumed to be linear elastic (i.e. non porous). In this case, the nodal DOFs at the top and bottom surface of the unit cell are the displacements in x- and y-direction ( $u_{e,x}$  and  $u_{e,y}$ ). [Yang et al 2017; Errico et al 2019] show how the sound transmission through three-dimensional periodic structures can be determined using the WFEM. This section applies the proposed solution approach on two-dimensional periodic structures and presents the theory in a modified way.

#### Excitation and coupling to the fluid domain

In analogy to section 2.6, two coupling conditions must be satisfied at the interface between the periodic structure and the semi-infinite fluid domain. The first one ensures the continuity of displacements:

$$\frac{1}{\rho_a \omega^2} \frac{\delta p_a}{\delta y} = u_{e,y}. \quad (4.25)$$

Inserting the pressure fields in the upper and lower fluid domain, we can derive the following expressions:

$$p_i - p_t = \frac{i\rho_a \omega^2}{k_y e^{-ik_x x}} u_{e,y}(x, 0) \quad \text{along the upper interface } y = 0 \text{ and} \quad (4.26)$$

$$p_t = -\frac{i\rho_a \omega^2}{k_y e^{i(-k_x x - k_y h)}} u_{e,y}(x, -h) \quad \text{for the lower interface } y = -h. \quad (4.27)$$

Second, we have to enforce the equilibrium of forces at the coupling interfaces:  $\sigma_y = -p_a$ . This results in

$$\sigma_y(x, 0) = -p_a(x, 0), \quad (4.28)$$

$$\sigma_y(x, -h) = -p_a(x, -h). \quad (4.29)$$

Inserting equations (4.26) and (4.27) into equations (4.28) and (4.29), we can express the acoustic excitation and the coupling between fluid domain and periodic structure via equivalent normal stresses at the unit cell's top and bottom surface:

$$\sigma_y(x, 0) = 2p_i e^{-ik_x x} - D_a u_{e,y}(x, 0), \quad (4.30)$$

$$\sigma_y(x, -h) = D_a u_{e,y}(x, -h), \quad (4.31)$$



whereby  $D_a = \frac{i\rho_a\omega^2}{k_y}$  is the equivalent fluid density.

Integrating the equivalent normal stresses over the top and bottom surface of the unit cell, we can compute the equivalent excitation vector to be applied on the unit cell. Assuming piecewise constant equivalent normal stresses, the integration can be simplified to a multiplication by the nodal intake surface  $\Delta x$ . As a result we get:

$$\begin{bmatrix} \mathbf{e}_L \\ \mathbf{e}_R \\ \mathbf{e}_B \end{bmatrix} = \mathbf{e}_1 + \text{diag}(\mathbf{e}_2) \begin{bmatrix} \mathbf{q}_L \\ \mathbf{q}_R \\ \mathbf{q}_B \end{bmatrix}, \quad (4.32)$$

with

$$e_{1,x}(x,y) = 0, \quad (4.33)$$

$$e_{1,y}(x,y) = \begin{cases} 2p_1 e^{-ik_x x} \Delta x & y = 0, \\ 0 & y \neq 0, \end{cases} \quad (4.34)$$

and

$$e_{2,x}(x,y) = 0, \quad (4.35)$$

$$e_{2,y}(x,y) = \begin{cases} -D_a \Delta x & y = 0, \\ D_a \Delta x & y = -h, \\ 0 & \text{else.} \end{cases} \quad (4.36)$$

### Formulation of the equation system to be solved

Introducing equation (4.32) into equation (4.22) leads to

$$\mathbf{\Lambda}_L [\hat{\mathbf{D}} - \text{diag}(\mathbf{e}_2)] \mathbf{\Lambda}_R \begin{bmatrix} \mathbf{q}_L \\ \mathbf{q}_B \end{bmatrix} = \mathbf{\Lambda}_L \mathbf{e}_1, \quad (4.37)$$

which shall be solved for  $\mathbf{q}$  for a given excitation.

For the special case where the bottom of the unit cell is not coupled to a semi-infinite acoustic fluid but supported by a rigid backing, the DOFs at the bottom vanish and the corresponding rows and columns in equation (4.37) may be removed.

### Post-processing of the sound transmission loss and absorption coefficient

Having solved equation (4.37) for the vector of DOFs  $\mathbf{q}$ , we can compute  $p_r$  and  $p_t$  using equations (4.26) and (4.27). Out of that the sound transmission loss  $T$  can be computed as

$$T = -10 \log(\tau(\Theta)), \quad (4.38)$$

with the power transmission coefficient being defined by

$$\tau(\Theta) = \frac{|p_t^2|}{|p_i^2|}. \quad (4.39)$$

If the bottom of the unit cell is supported by a rigid backing,  $\tau(\Theta) = 0$  and  $T$  is not searched for.

The reflection coefficient is given as

$$r(\Theta) = \frac{|p_r^2|}{|p_i^2|}. \quad (4.40)$$

Knowing both, transmission and reflection coefficient, we can compute the absorption coefficient:

$$\alpha(\Theta) = 1 - \tau(\Theta) - r(\Theta). \quad (4.41)$$

#### 4.4.4 Porous boundary layers

The top and bottom layer of the periodic structure now consist out of porous material. The porous domain is modelled using the classical formulation of the JCAM, as for the given application case the coupling to the semi-infinite fluid domains is more straight forward and the symmetry of the system matrix could later on be exploited to reduce the computational effort. Using the classical formulation results in four nodal DOFs at the unit cells top and bottom surface for the considered two-dimensional problem: the displacements in  $x$ - and  $y$ -direction corresponding to the solid ( $u_{s,x}$  and  $u_{s,y}$ ) and fluid phase ( $u_{f,x}$  and  $u_{f,y}$ ).

### Excitation and coupling to the fluid domain

In comparison to linear elastic boundary layers, modelling the excitation and the coupling to the semi-infinite fluid layers is more complex. Again, we need to enforce the continuity of displacements along the interface between the periodic structure and the semi-infinite fluid domains:

$$\frac{1}{\rho_a \omega^2} \frac{\delta p_a}{\delta y} = (1 - \phi) u_{s,y} + \phi u_{f,y}, \quad (4.42)$$

which leads to

$$p_i - p_t = D_a \frac{1}{e^{-ik_x x}} \left( (1 - \phi) u_{s,y}(x, 0) + \phi u_{f,y}(x, 0) \right), \quad (4.43)$$

$$p_t = -D_a \frac{1}{e^{i(-k_x x - k_y h)}} \left( (1 - \phi) u_{s,y}(x, -h) + \phi u_{f,y}(x, -h) \right). \quad (4.44)$$

The equilibrium of forces is expressed by

$$\sigma_{s,y} = -(1 - \phi) p_a, \quad (4.45)$$

$$\sigma_{f,y} = -\phi p_a. \quad (4.46)$$

Introducing equations (4.43) and (4.44) into equations (4.45) and (4.46), we can find the equivalent normal stresses at the unit cells top ( $y = 0$ ) and bottom ( $y = -h$ ) surface:

$$\sigma_{s,y}(x, 0) = (1 - \phi) \left( 2p_i e^{-ik_x x} - D_a \left( (1 - \phi) u_{s,y}(x, 0) + \phi u_{f,y}(x, 0) \right) \right), \quad (4.47)$$

$$\sigma_{f,y}(x, 0) = \frac{\phi}{1 - \phi} \sigma_{s,y}(x, 0), \quad (4.48)$$

$$\sigma_{s,y}(x, -h) = (1 - \phi) \left( D_a \left( (1 - \phi) u_{s,y}(x, -h) + \phi u_{f,y}(x, -h) \right) \right), \quad (4.49)$$

$$\sigma_{f,y}(x, -h) = \frac{\phi}{1 - \phi} \sigma_{s,y}(x, -h), \quad (4.50)$$

mapping both, the excitation by an inclined plane wave at the upper boundary and the coupling to the semi-infinite fluid domains.

The nodal excitations in  $y$ -direction can be computed from the normal stresses via integration with respect to  $x$ . Same as above, this can be approached by a multiplication with the nodal intake surface  $\Delta x$ . We get:

$$e_{s,y}(x,0) = \underbrace{(1-\phi)2p_i e^{-ik_x x} \Delta x}_{\text{Right hand side contribution to } \hat{\mathbf{e}}} - \underbrace{(1-\phi)^2 D_a u_{s,y}(x,0) \Delta x}_{\text{Left hand side contribution to diagonal of } \hat{\mathbf{D}}_e} - \underbrace{(\phi - \phi^2) D_a u_{f,y}(x,0) \Delta x}_{\text{Left hand side contribution to off-diagonal of } \hat{\mathbf{D}}_e}, \quad (4.51)$$

$$e_{f,y}(x,0) = \underbrace{\phi 2p_i e^{-ik_x x} \Delta x}_{\text{Right hand side contribution to } \hat{\mathbf{e}}} - \underbrace{\phi^2 D_a u_{f,y}(x,0) \Delta x}_{\text{Left hand side contribution to diagonal of } \hat{\mathbf{D}}_e} - \underbrace{(\phi - \phi^2) D_a u_{s,y}(x,0) \Delta x}_{\text{Left hand side contribution to off-diagonal of } \hat{\mathbf{D}}_e}, \quad (4.52)$$

$$e_{s,y}(x, -h) = \underbrace{\phantom{(1-\phi)2p_i e^{-ik_x x} \Delta x}}_{\text{Right hand side contribution to } \hat{\mathbf{e}}} - \underbrace{(1-\phi)^2 D_a u_{s,y}(x, -h) \Delta x}_{\text{Left hand side contribution to diagonal of } \hat{\mathbf{D}}_e} + \underbrace{(\phi - \phi^2) D_a u_{f,y}(x, -h) \Delta x}_{\text{Left hand side contribution to off-diagonal of } \hat{\mathbf{D}}_e}, \quad (4.53)$$

$$e_{f,y}(x, -h) = \underbrace{\phantom{\phi 2p_i e^{-ik_x x} \Delta x}}_{\text{Right hand side contribution to } \hat{\mathbf{e}}} - \underbrace{\phi^2 D_a u_{f,y}(x, -h) \Delta x}_{\text{Left hand side contribution to diagonal of } \hat{\mathbf{D}}_e} + \underbrace{(\phi - \phi^2) D_a u_{s,y}(x, -h) \Delta x}_{\text{Left hand side contribution to off-diagonal of } \hat{\mathbf{D}}_e}. \quad (4.54)$$

We can express the right hand side vector as

$$\begin{bmatrix} \mathbf{e}_L \\ \mathbf{e}_R \\ \mathbf{e}_B \end{bmatrix} = \hat{\mathbf{e}} + \hat{\mathbf{D}}_e \begin{bmatrix} \mathbf{q}_L \\ \mathbf{q}_R \\ \mathbf{q}_B \end{bmatrix}, \quad (4.55)$$

where the non-zero components of  $\hat{\mathbf{e}}$  and  $\hat{\mathbf{D}}_e$  are given in equations (4.51)-(4.54).

### Formulation of the equation system to be solved

Inserting equation (4.55) into equation(4.22), we find

$$\Lambda_L \left[ \hat{\mathbf{D}} - \hat{\mathbf{D}}_e \right] \Lambda_R \begin{bmatrix} \mathbf{q}_L \\ \mathbf{q}_B \end{bmatrix} = \Lambda_L \hat{\mathbf{e}}. \quad (4.56)$$

The system of equations depicted above is solved for  $\mathbf{q}$  for a given excitation by an inclined, plane acoustic wave. From  $\mathbf{q}$  the reflection, transmission and absorption coefficient and the sound transmission loss can be post-processed in analogy to section 4.4.3.

Supports at the bottom interface can be considered by eliminating the respective DOFs from equation (4.56). Combing the strategies presented above, we can evaluate the sound transmission through periodic structures where one of the coupling interfaces with the semi-infinite fluids is porous and the other one is elastic.

## 4.5 Conclusion

This chapter explains how the dispersion characteristics of periodic structures can be evaluated using the WFEM. Making use of the Bloch theorem, the periodic structure is represented by a FEM model of a single unit cell. Two approaches for studying the wave propagation along the periodic structure are given: the inverse and the direct approach. The inverse approach solves for the frequency ranges in which propagating waves emerge. The frequency ranges to which no propagating waves are assigned are referred to as stop bands. The direct approach also takes into account damped and evanescent waves and therefore generally involves a higher computational effort than the inverse approach. In addition to that, this chapter shows how the WFEM can be employed to compute the sound transmission through periodic structures. Hereby the existing strategy for elastic unit cells is extended to periodic structures consisting of porous material modelled by the classical formulation of the JCAM.

## 5 Numerical studies

### 5.1 Introduction

As proved by the literature review in the introduction of this thesis, periodic metamaterials show favourable dispersion characteristics for many application cases. After having introduced numerical solutions strategies for efficiently analysing the vibroacoustic behaviour of periodic metamaterials in the previous chapters, this chapter verifies the presented solution approaches and performs numerical studies on exemplary designs. Thereby one main point of investigation is the evaluation of the impact of inclusions and secondary vibrational systems on the dispersion characteristics of linear elastic plates. In addition, the potential of the proposed solution methods is demonstrated by two different examples. First, the influence of point mass inclusions on the absorption of porous layers is determined. Furthermore, it is shown that inclusions can manipulate the sound transmission through two-shell walls.

### 5.2 Stop band behaviour of periodic metamaterials

This set of numerical studies investigates how inclusions within the unit cell affect the wave propagation along a periodic metamaterial. First, the impact of the inclusion shape on the emerging stop band pattern is analysed. Second, tuned mass dampers (TMDs) are embedded into the inclusion and the impact of the TMD orientation on the wave propagation is evaluated. Parts of the work presented below were already published in [Weber et al 2019] and [Weber et al 2020].

For all calculations displayed within the scope of this section, the unit cell consists of aluminum; the employed material parameters are given in table 5.1. The two-dimensional cells all are of height  $H = 0.04$  m and length  $L_x = 0.06$  m. The structures are analysed in a frequency range up to 45 kHz. As the focus is put on the investigation of the stop band

patterns corresponding to the studied unit cell designs, the computations are carried out using the inverse approach of the WFEM.

Young's modulus	$E_e = 70 \text{ GPa}$
Density	$\rho_e = 2699 \frac{\text{kg}}{\text{m}^3}$
Poisson's ratio	$\nu_e = 0.34$

**Table 5.1:** Material parameters of aluminium.

### 5.2.1 Preliminary study

In the course of a preliminary study, the results obtained with the selected solution method are checked for plausibility. In addition, it is explained how dispersion characteristics are visualized in the scope of this thesis. For this purpose, the wave propagation corresponding to a unit cell without inclusion is studied using the inverse approach of the WFEM.

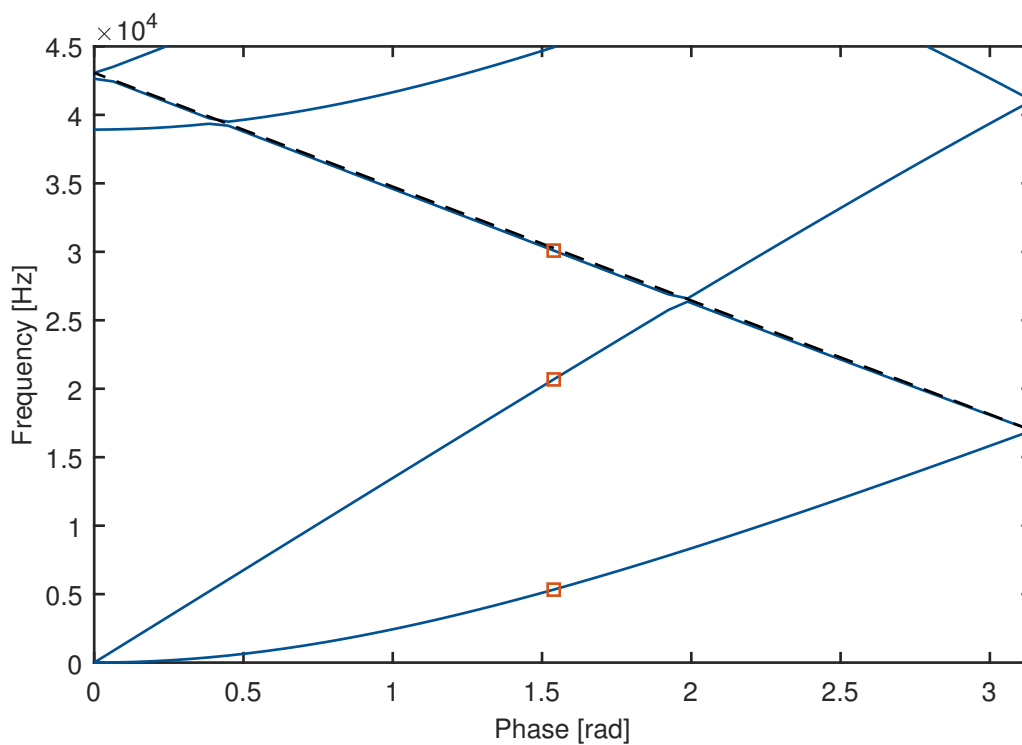


**Figure 5.1:** Dispersion curves for homogeneous unit cell (—); auxiliary line (- - -) and markers for certain combinations of phase and frequency  $\square$ , for which deformation pattern is plotted in figure 5.2.

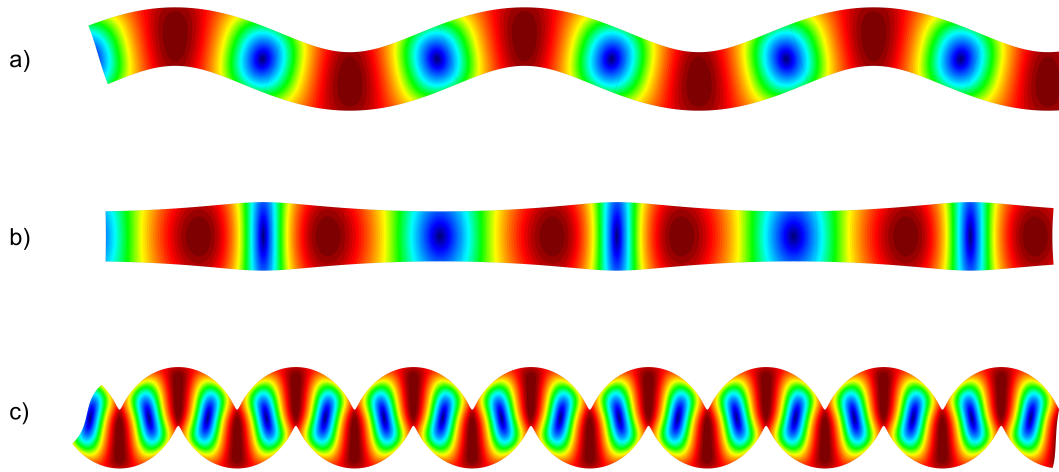


**Figure 5.2:** Deformed shape of homogeneous periodic structure for a) ( $\frac{\pi}{2}$  rad, 5.33 kHz), b) ( $\frac{\pi}{2}$  rad, 20.68 kHz) and c) ( $\frac{\pi}{2}$  rad, 30.09 kHz).

Figure 5.1 shows the cell's dispersion characteristics in a frequency range from 0 to 45 kHz. The phase  $\kappa_{\text{R}}L_x$  depicts the phase shift as the wave travels from one unit cell to the next. The so-called dispersion curves or frequency bands visualize for which combinations of frequency and phase propagating waves emerge. The shape of the dispersion curves gives conclusion on the corresponding wave type. For higher frequencies, for which complex propagation patterns can be observed, an evaluation of the deformed geometry provides clear information about the wave type. For the studied two-dimensional periodic structure of finite height  $H$ , dispersive bending waves and non dispersive quasi-longitudinal waves emerge. With the material composition and geometry not varying along  $L_x$ , it is evident that no stop bands occurs.

Two dispersion curves in figure 5.1 start from the origin. The bending wave being dispersive, the slope of the corresponding dispersion curve is not constant. Thus the lower curve depicts the bending wave. The other band with approximately constant slope corresponds to the quasi-longitudinal wave. From the slope we can deduce the wave speed  $c_{\text{Q}} = 5090 \frac{\text{m}}{\text{s}}$ , which only deviates by less than half a percent from the theoretically expected value that can be computed using the respective formula in table 2.1. Thus, the computation outcome can be considered plausible.

Figure 5.2 shows the deformed periodic structure for the combinations of phase and frequency marked on the dispersion curves in figure 5.1. The deformation patterns confirm that the two curves starting from the origin correspond to bending wave respectively quasi-longitudinal wave. The slope of the third band, which adjoins the curve assigned to the bending wave, is approximately constant. Only with the auxiliary line with constant slope inserted in figure



5.1, it can be seen that this curve also belongs to a dispersive wave. Figure 5.2 confirms that the third band represents the bending wave for higher frequencies. On the basis of figure 5.1, it can be said that for the configuration under consideration, for higher frequencies a lower dispersivity of the bending wave can be observed. This suggests that above a certain frequency range, the ordinary bending theory can no longer be used to assess the system's dispersion characteristics.

### 5.2.2 Impact of the inclusion shape

This section studies the influence of the inclusion shape on the wave propagation within the periodic structure. In a first step, the dispersion characteristics corresponding to the three inclusion shapes given in figure 5.3 are computed.

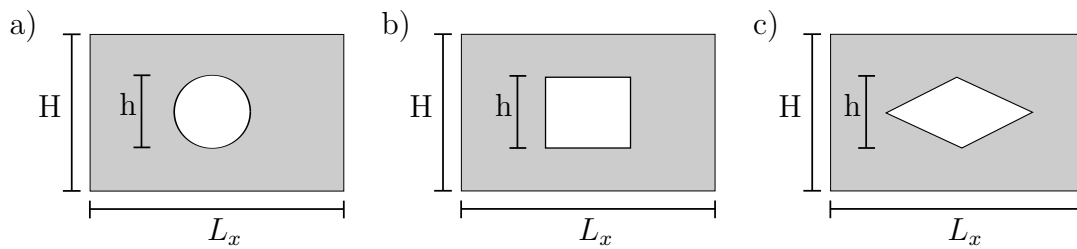


**Figure 5.3:** First set of inclusion shapes: a) circle, b) rectangle, c) rhombus.

The geometry of the circular, rectangular and rhombic inclusion is given by their height  $h = 0.02$  m and area  $A = 3.14 \cdot 10^{-4}$  m<sup>2</sup>. All inclusions are positioned in the centre of the unit cell. To study only the influence of the shape and not that of the mass loss caused by the inclusion, all inclusion shapes are attributed with the same height and area.

The dispersion characteristics of the unit cells are given in figures 5.4 to 5.6. For all configurations a stop band is observed, with the width depending on the shape of the inclusion. Figure 5.7 compares the stop band location and width. The stop band corresponding to circular and rectangular inclusion is similar; the smallest stop band is obtained for the rhombic inclusion.

In order to relate the stop band width to the geometry of the unit cell, we take a look at the mass distribution of the examined cell geometries. The mass distributions over the length of the cells are visualized in figure 5.8. The mass density corresponds to the product of the material's density and the material filled height (total height minus local inclusion height). The average mass density is given by  $E(X) = \rho_e \frac{(HL_x) - A}{L_x}$ .

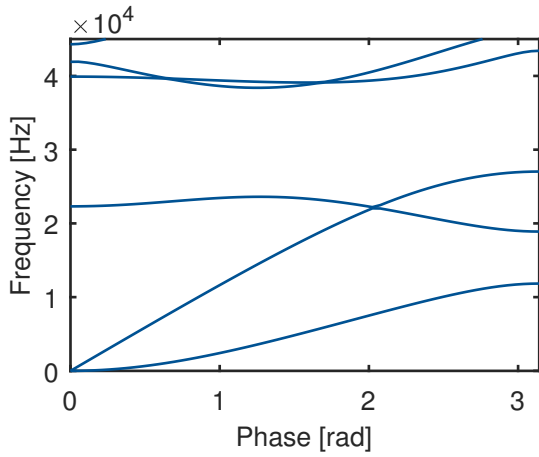


**Figure 5.4:** Dispersion curves for unit cell with circular inclusion.

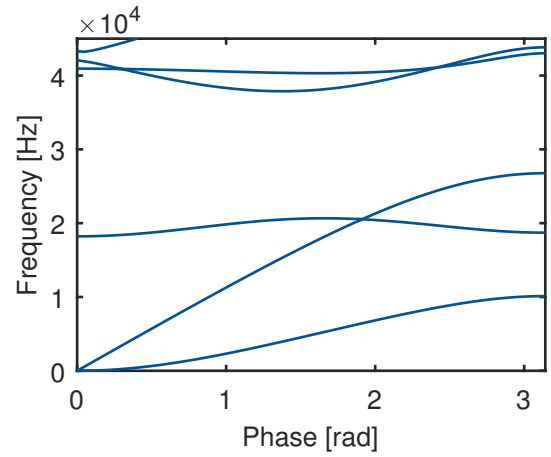


**Figure 5.5:** Dispersion curves for unit cell with rectangular inclusion.

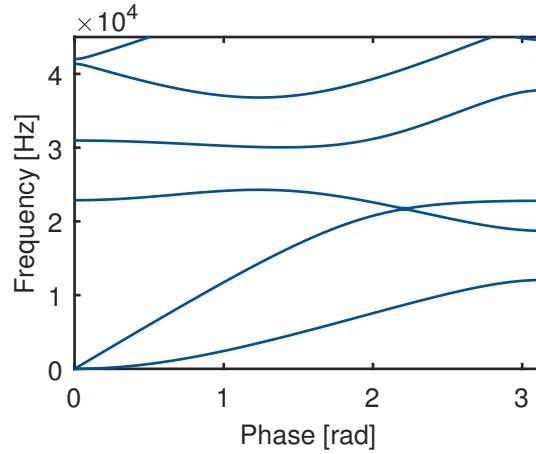


**Figure 5.6:** Dispersion curves for unit cell with rhombic inclusion.

The uniformity of the mass distribution can be quantified by the value of the variance of the mass distribution:

$$\text{Var}(X) = \int_0^{L_x} (X - E(X))^2 dx. \quad (5.1)$$

$X$  is the mass density and  $E(X)$  the average mass density. The smaller the value of  $\text{Var}(X)$ , the more uniform is the mass distribution over the length of the cell. Table 5.2 contains the variances corresponding to the set of inclusion shapes under investigation. For the unit cells studied, it can be stated that the more uniform the mass distribution along the unit cell, and accordingly the smaller  $\text{Var}(X)$ , the smaller the stop band.

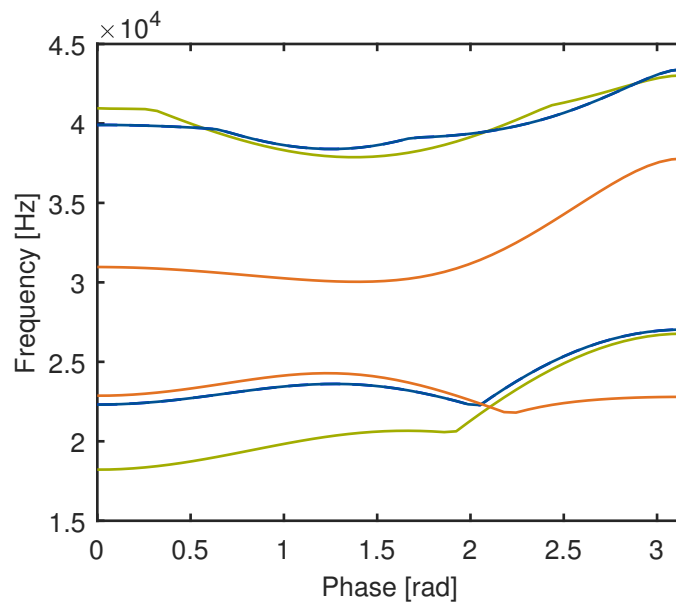


**Figure 5.7:** Comparison of stop band width for different inclusion types: circle (—), rectangle (—) and rhombus (—).

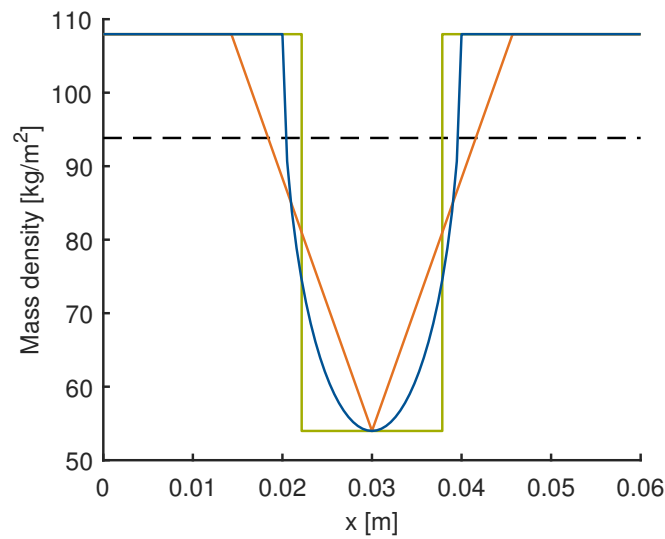


**Figure 5.8:** Distribution of mass with respect to  $x$ : circle (—), rectangle (—) and rhombus (—); (- -) marks average mass density.

Inclusion shape	Variance $[\frac{\text{kg}^2}{\text{m}^3}]$
Circle	26.87
Rectangle	33.22
Rhombus	18.53

**Table 5.2:** Variance of mass distribution corresponding to first set of unit cells.

To investigate this observation in more detail, a second set of unit cells is examined. Their geometry is specified in figure 5.9. Now, not only unit cells with inclusions but also with notches are considered. The inclusions are located in the centre of the cell. The radius  $r$  determines the size of the circular inclusions and notches. The height  $h$  and the width  $b$  indicate the size of the rectangular inclusions and notches.

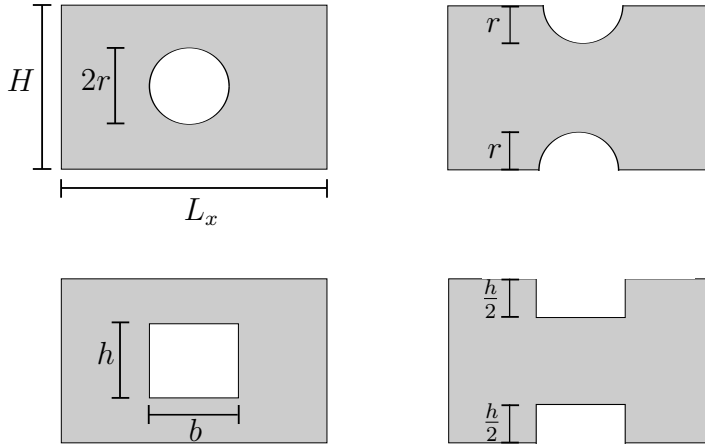


**Figure 5.9:** Second set of cell geometries; left: inclusions; right: notches.

The variance of mass distribution corresponding to the rectangular inclusion/notch may be expressed by

$$\text{Var}(X)_{\square} = \rho_e^2 h^2 \left( b - \frac{b^2}{L_x} \right). \quad (5.2)$$

First, the dispersion characteristics of unit cells with rectangular inclusions and notches of different sizes are analysed;  $b$  is altered, while  $h = 0.02$  m. For the limit cases  $b = 0$  and  $b = L_x$  no stop band emerges. The first case corresponds to a homogeneous unit cell without inclusion, while for the second case two stacked but unconnected homogeneous layers are considered.

In figure 5.10 both the variance in mass distribution and the stop band width are plotted for rectangular inclusions with  $b = [0, L_x]$ . Hereby the stop band width corresponds to the total frequency range between 0 and 45 kHz where no undamped waves emerge. If there is more than one stop band, the total stop band width is obtained by summing up the individual stop band widths. It can be observed that both the variance in mass distribution and the

stop band width rise for increasing values of  $b$  from zero to a maximum value and then return to zero. The difference is that the maximum is reached for unequal values of  $b$ . It can be concluded that although the stop band tends to increase with an increasing variance, this statement is not generally true. For example, the variance increases from  $b = 0.02$  m to  $b = 0.03$  m, but the observed stop band is smaller.

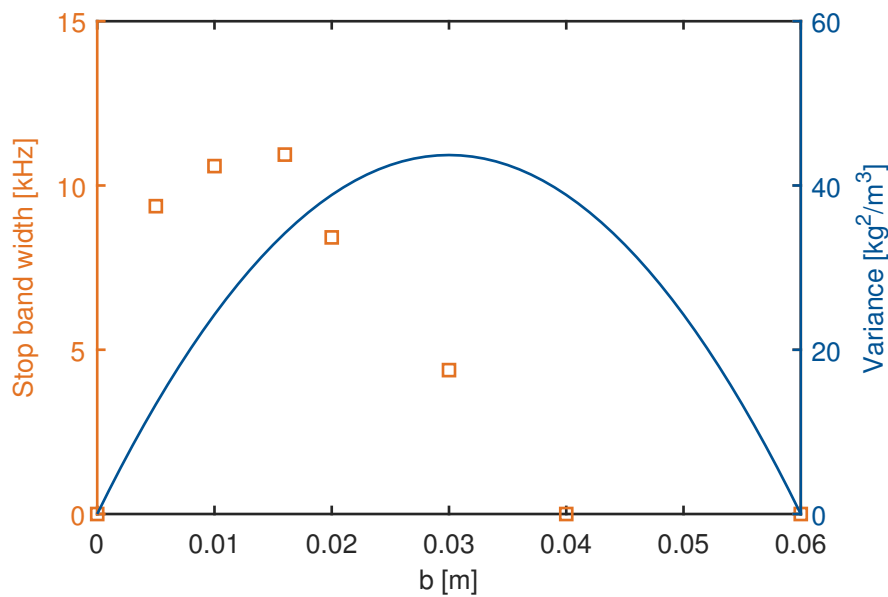


**Figure 5.10:** Correlation between variance in mass distribution and stop band width for unit cell with rectangular inclusion.

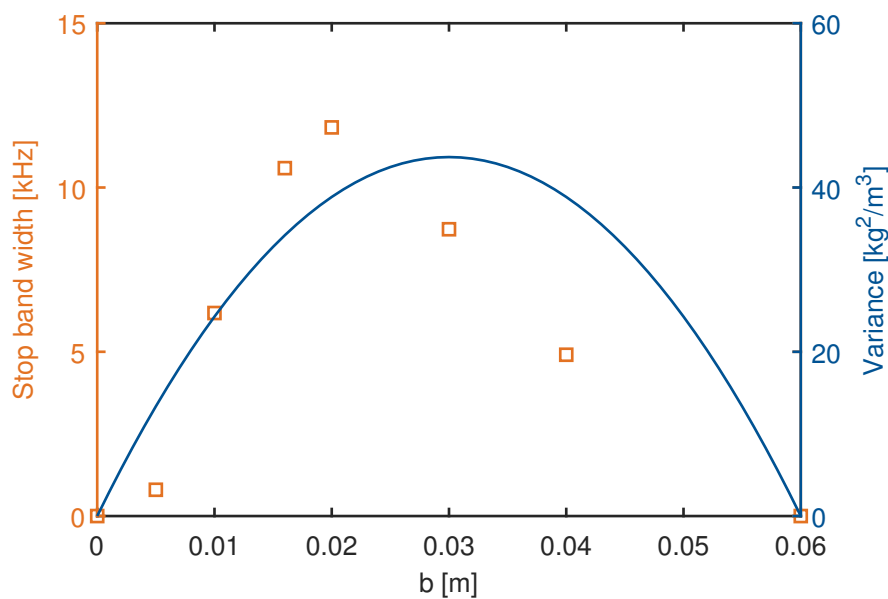


**Figure 5.11:** Correlation between variance in mass distribution and stop band width for unit cell with rectangular notch.

Figure 5.11 shows the correlation between the variance in mass distribution and the stop band width for rectangular notches. One can observe a similar behaviour as with the rectangular inclusions.

Next, the dispersion characteristics of unit cells with differently shaped inclusions/notches but the same variance in mass distribution are evaluated. We choose a circular inclusion/notch of radius  $r = 0.01$  m, resulting in a variance in mass distribution of  $26.86 \frac{\text{kg}^2}{\text{m}^3}$ . We adapt the dimensions of a rectangular inclusion/notch to match the variance in mass distribution and the total mass of the unit cells with circular inclusion/notch.

Figure 5.12 shows the dispersion curves corresponding to the unit cell with circular inclusion and notch. We observe a stop band for both, the circular inclusion and the circular notch, whereby the stop band corresponding to the notch is smaller and located in a higher frequency range than the stop band corresponding to the inclusion.

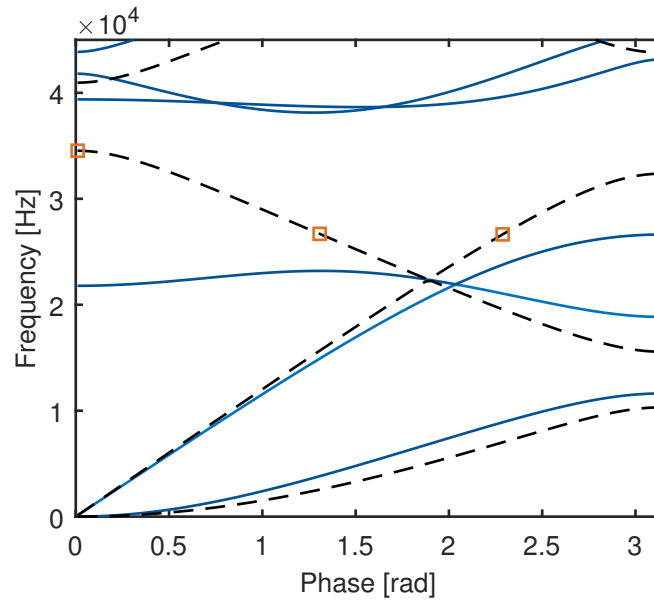
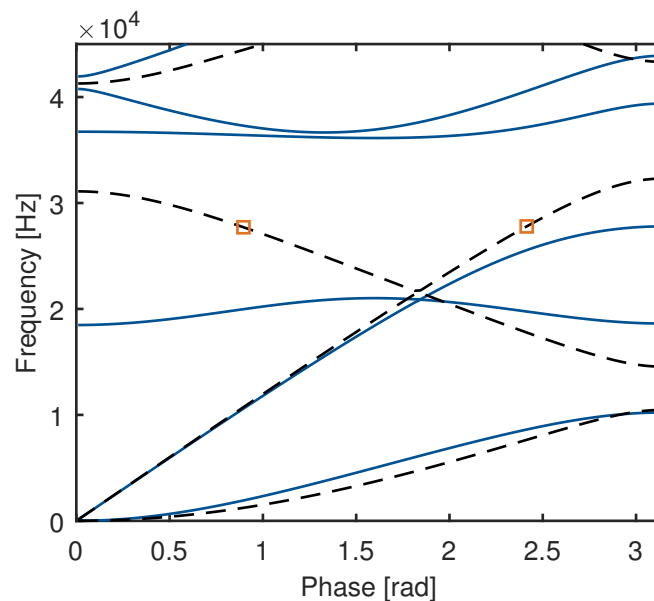


**Figure 5.12:** Dispersion curves for unit cell with circular inclusion (—) and circular notch (- - -); for combinations of phase and frequency marked by  $\square$ , deformation pattern is plotted in figure 5.15.

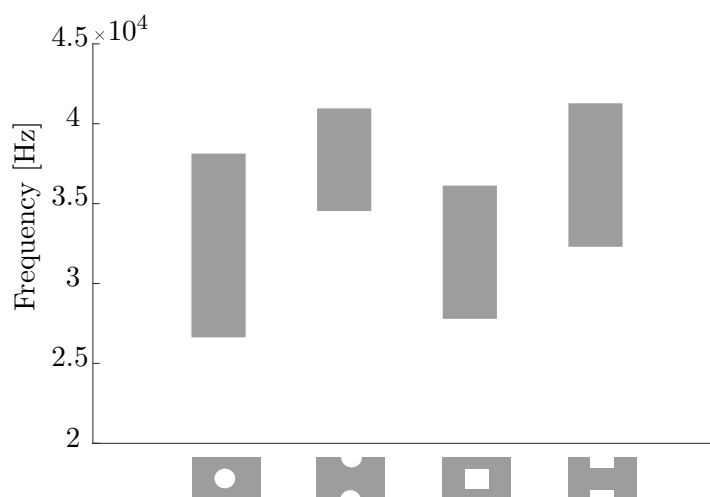
Figure 5.13 compares the dispersion characteristics of the unit cells with rectangular inclusion and rectangular notch. Again the stop band corresponding to the notch is located in a higher frequency range, but the stop band width is of similar size as of the one corresponding to the inclusion.

Figure 5.14 summarizes the stop band width and location corresponding to the studied geometries. As stated before, all geometries induce the same total unit cell mass and the same

variance in mass distribution. The circular inclusion leads to the broadest stop band, while the circular notch results in the smallest stop band. The stop band widths corresponding to rectangular inclusion and notch are of similar sizes, and centred around frequencies similar to those of the corresponding circular shapes. We conclude that not only the mass distribution along the cell but also the inclusion/notch shape itself has an impact on the dispersion characteristics of the periodic structure and in particular on the stop band width.



**Figure 5.13:** Dispersion curves for unit cell with rectangular inclusion (—) and rectangular notch (- - -); for combinations of phase and frequency marked by  $\square$ , deformation pattern is plotted in figure 5.16.



**Figure 5.14:** Stop band location and width of unit cells with differently shaped inclusions but equal variance in mass distribution.

To further study the impact of the cell design on the stop band location, we take a look at the deformed periodic structures for the locations marked with a box on the dispersion curves in figures 5.12 and 5.13. Figure 5.15 a) visualizes the deformed structure for a unit cell with circular inclusion just below the stop band. We can see that the wavelength of the observed quasi longitudinal wave roughly equals twice the length of the unit cell. For higher frequencies, the wave will be trapped between the inclusions leading to the observed stop band. Plotting the deformed shape of the periodic structure with circular notches for the same frequency (figure 5.15 c) and d)), we can see that for both, bending and quasi longitudinal wave, the wavelength is not an integer multiple of the cell length. We can state that for equal frequencies, the wavelength of the waves propagating along the structure with circular inclusions is smaller than the one of the waves propagating along the structure with circular notches. As a result, the frequency range in which a stop band due to destructive interference occurs is shifted towards higher frequencies (figure 5.15 b)). As illustrated in figure 5.16, this observation can be transferred to the periodic structure with rectangular inclusions and notches.

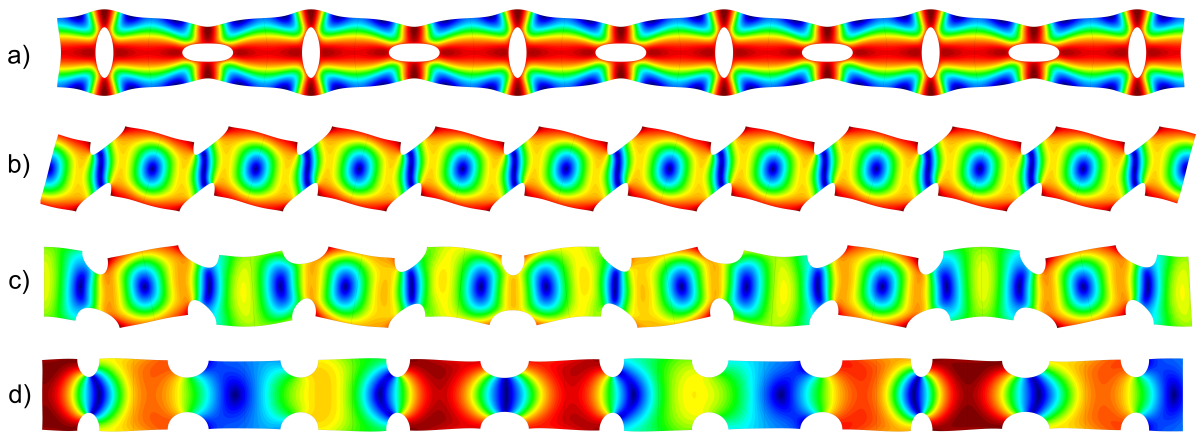


**Figure 5.15:** Deformed shape of periodic structure with circular inclusion for a) ( $\pi$  rad, 26.63 kHz) and circular notch for b) (0 rad, 34.54 kHz), c) (1.31 rad, 26.63 kHz), d) (2.28 rad, 26.63 kHz).

From the performed numerical investigations on the impact of the inclusion shape on the dispersion patterns one can draw the following conclusions:

- For inclusions of the same area, the shape of the inclusion has an impact on the dispersion characteristics.
- In the performed numerical studies a higher variance in mass distribution does not necessarily lead to a broader stop band. Still, a higher variance in mass distribution tends to result in a wider stop band.



- For cell configurations with the same variance in mass distribution, the shape of the inclusion has an impact on the stop band location and width. Within the analysed geometries, the circular inclusion leads to a broader stop band than the rectangular inclusion and notch and the circular notch. In addition, the stop bands corresponding to the notches are located at higher frequency ranges than the ones corresponding to the inclusions.

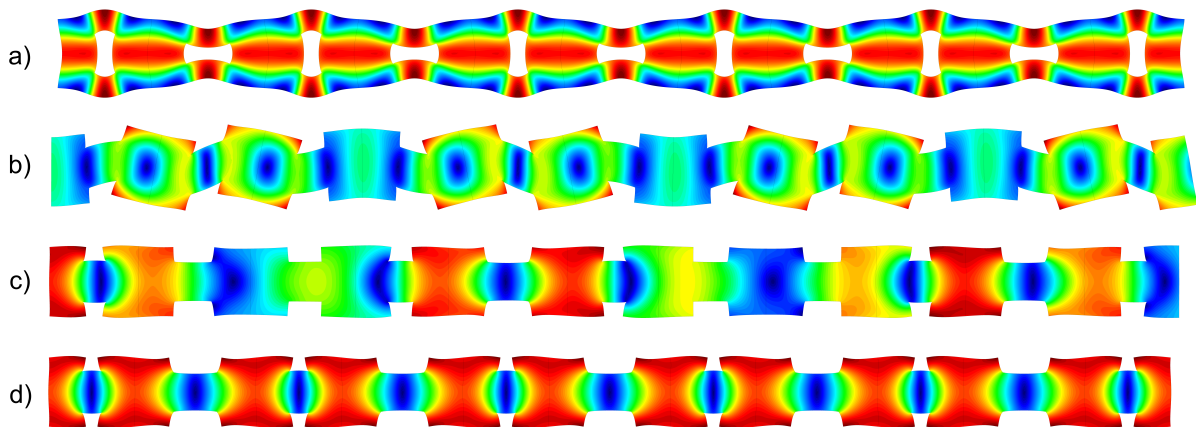


**Figure 5.16:** Deformed shape of periodic structure with rectangular inclusion for a) ( $\pi$  rad, 27.79 kHz) and rectangular notch for b) (0.89 rad, 27.79 kHz), c) (2.41 rad, 27.79 kHz), d) ( $\pi$  rad, 32.30 kHz).

### 5.2.3 Impact of subsystems within the inclusions

Now the influence of the alignment of a TMD within the inclusion on the wave propagation in the periodic metamaterial is evaluated. For this analysis, a unit cell with circular inclusion with a radius of 0.01 m is chosen. Figure 5.17 shows the TMD-alignments to be considered.

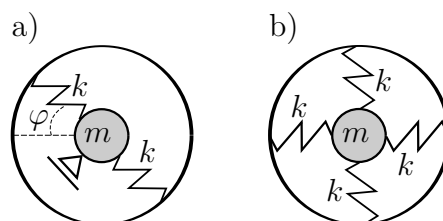
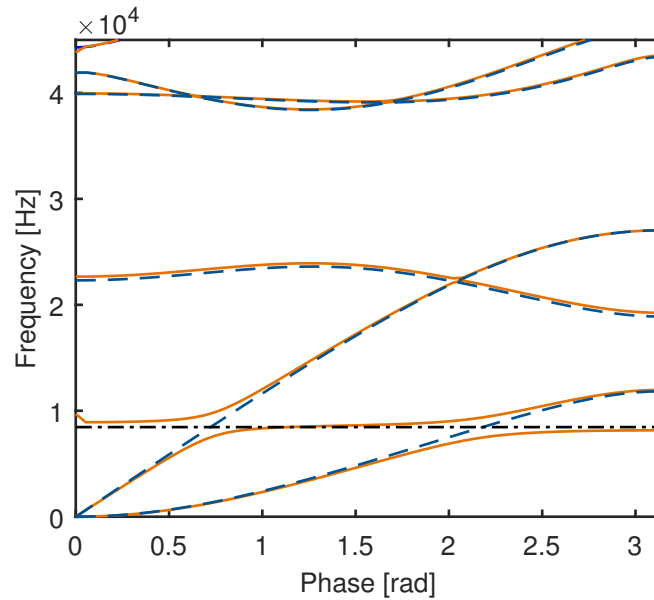


**Figure 5.17:** Spring alignments to be considered: a) single-spring inclined by angle  $\varphi$ , b) double-spring.

As the damping is set to zero, the TMDs are modeled by spring(s) and a concentrated mass. In addition to a TMD with a spring which is inclined by an angle  $\varphi$ , a configuration with two orthogonal springs (termed as double-spring) is examined. The mass is located in the centre

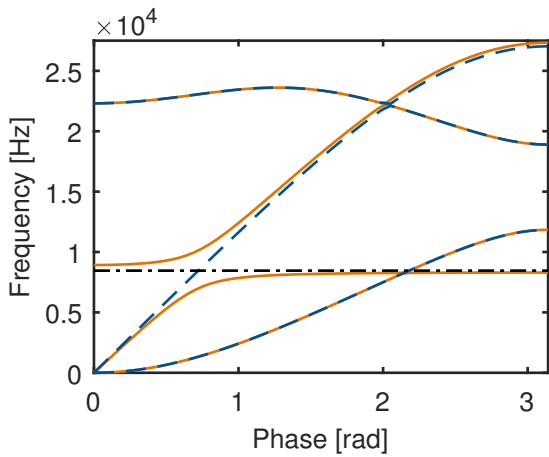
of the spring(s). It is assumed that the mass is only able to move along the direction of the spring(s). The material configuration of mass and spring(s) will not be changed during the investigations. While the mass equals  $A\rho_e = 0.85$  kg, which is the mass that has been removed from the unit cell due to embedding the inclusion, the spring stiffness is chosen as  $1.20 \frac{\text{GN}}{\text{m}}$ . The first eigenfrequency of all TMD configurations is given by  $f_{\text{TMD}} = \frac{1}{2\pi} \sqrt{\frac{2k}{m}}$  and equals 8457 Hz.

Figure 5.18 compares the dispersion characteristics of a cell with circular inclusion without TMD and with TMD which is inclined by  $\varphi = \frac{\pi}{4}$  rad. A straight dotted line marks the eigenfrequency of the TMD. It can be seen that both, the bending and quasi longitudinal wave are deflected due to the TMD. Furthermore, figure 5.18 shows that for the chosen material parameters the TMD particularly affects the frequency range below the stop band. Consequently, in the following we will concentrate on that frequency range.



**Figure 5.18:** Dispersion curves for unit cell with circular inclusion without TMD (---) and with single-spring TMD inclined by  $\frac{\pi}{4}$  rad (—); (- · -) marks eigenfrequency of TMD.

Figures 5.19 and 5.20 display the dispersion characteristics with a TMD inclined by  $\varphi = 0$  rad and  $\varphi = \frac{\pi}{2}$  rad. While a horizontal TMD only deflects the quasi longitudinal wave, a vertical TMD only modifies the band corresponding to the bending wave. Figure 5.21 shows that those limit cases merge into one another when varying  $\varphi$  between 0 rad and  $\frac{\pi}{2}$  rad. Furthermore, figure 5.22 verifies that, as the system is symmetric, an inclination  $\varphi$  of  $\frac{\pi}{4}$  rad and  $-\frac{\pi}{4}$  rad will lead to the same result. This statement holds for all pairs  $\pm\varphi$ .



**Figure 5.19:** Dispersion curves for unit cell with circular inclusion without TMD (---) and with single-spring TMD inclined by 0 rad (—); (- · -) marks eigenfrequency of TMD.

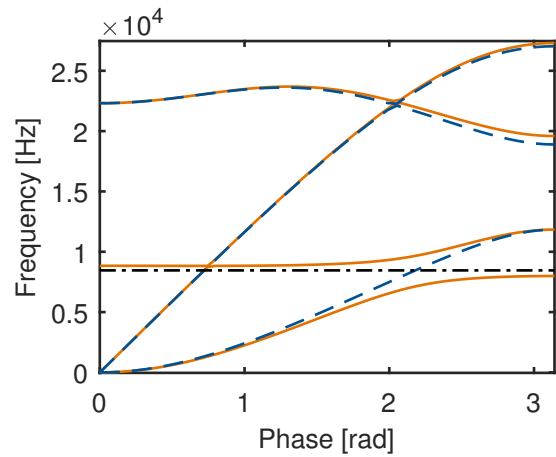


**Figure 5.20:** Dispersion curves for unit cell with circular inclusion without TMD (---) and with single-spring TMD inclined by  $\frac{\pi}{2}$  rad (—); (- · -) marks eigenfrequency of TMD.

The observed behaviour can be explained taking reference to the direction of particle motion corresponding to the different wave types. The part of wave energy transferred into the TMD will increase with increasing compliance of the direction of wave motion and spring force. While the forces within a horizontal spring coincide with the direction of particle motion of quasi longitudinal waves, the forces within a vertical spring match the direction of particle motion corresponding to bending waves.

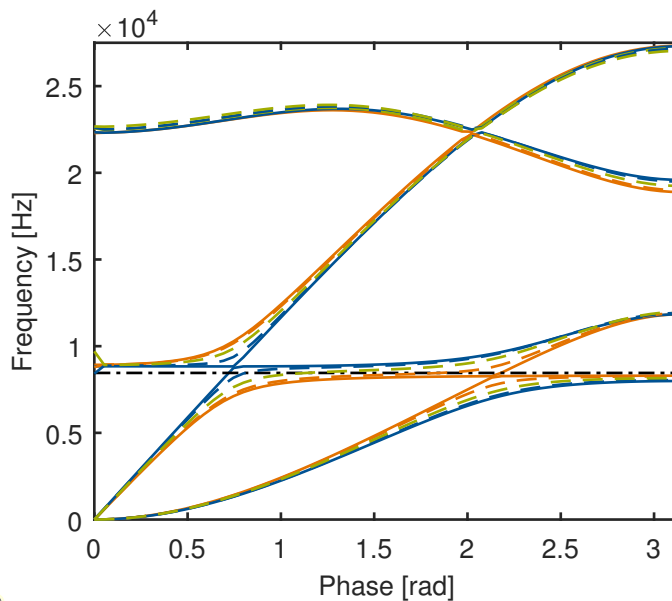


**Figure 5.21:** Dispersion curves for unit cell with circular inclusion and single-spring TMD inclined by 0 rad (—),  $\frac{\pi}{8}$  rad (---),  $\frac{\pi}{4}$  rad (- · -),  $\frac{3\pi}{8}$  rad (· · ·) and  $\frac{\pi}{2}$  rad (—); (- · -) marks eigenfrequency of TMD.

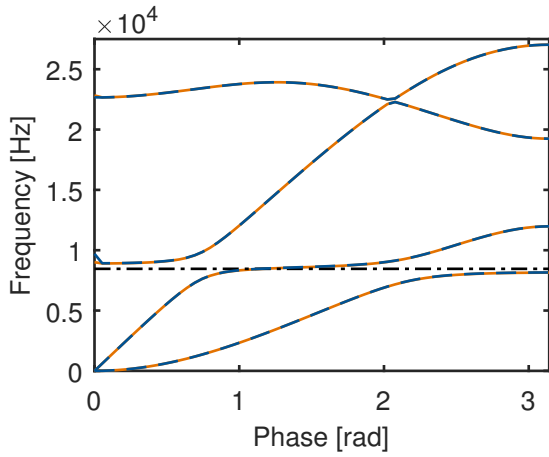


**Figure 5.22:** Dispersion curves for unit cell with circular inclusion and single-spring TMD inclined by  $\frac{\pi}{4}$  rad (—) and  $-\frac{\pi}{4}$  rad (- - -); (- · -) marks eigenfrequency of TMD.

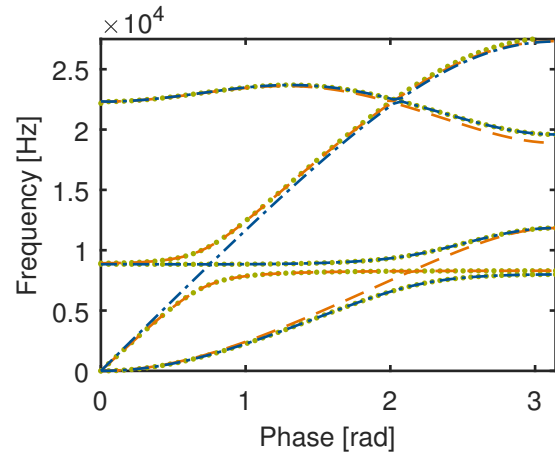


**Figure 5.23:** Dispersion curves for unit cell with circular inclusion with single-spring TMD inclined by 0 rad (- - -) and  $\frac{\pi}{2}$  rad (- · -) and with double-spring TMD (- · ·).

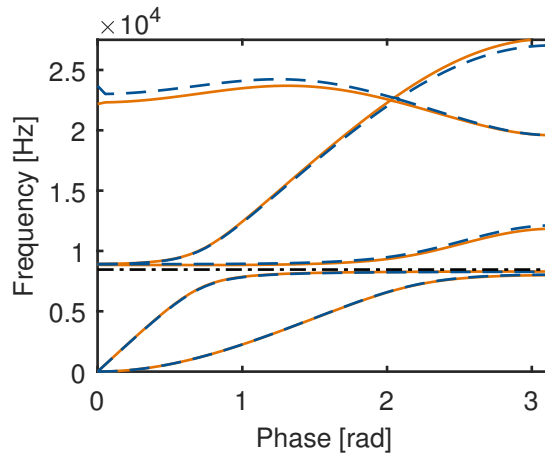


**Figure 5.24:** Dispersion curves for unit cell with circular inclusion and regular double-spring TMD (—) and double-spring TMD inclined by  $-\frac{\pi}{4}$  rad (- - -); (- · -) marks eigenfrequency of TMD.

As introduced in figure 5.17, in addition to a single-spring TMD, a TMD consisting of a double-spring system is considered. Figure 5.23 compares the dispersion curves corresponding to the double-spring configuration shown in figure 5.17 to those of TMDs with single springs inclined by  $\varphi = 0$  rad and  $\varphi = \frac{\pi}{2}$  rad. While for single-spring TMDs no total stop band at the eigenfrequency of the TMD is observed, for the double-spring system a stop band at the eigenfrequency occurs. Spring forces in direction of the particle motion corresponding to both, quasi longitudinal and bending wave explain the observed behaviour.

As long as the two springs have the same spring stiffness and are orthogonal with respect to each other, the portion of spring stiffness in horizontal and vertical direction is not modified

by an inclination of the double-spring. Figure 5.24 confirms that inclining the double-spring system will not change the dispersion curves in the area of the eigenfrequency of the TMD.

Investigating the influence of the TMD alignment on the dispersion characteristics of the studied metamaterials with inclusions leads to the following conclusions:

- Varying the inclination of a single-spring TMD, waves can be influenced purposefully.
- For the configurations studied, a double-spring system is required to obtain a total stop band at the eigenfrequency of the TMD.

## 5.3 Sound transmission characteristics of periodic metamaterials

In this section, the sound transmission and absorption of exemplary elastic and porous structures is analysed using the WFEM.

### 5.3.1 Preliminary study

The purpose of this preliminary study is to verify the plausibility of the results obtained with the in solution strategies presented in section 4.4.

#### Sound transmission through linear elastic structure

First, the sound transmission loss through a plate with infinite lateral extension is computed using the WFEM. The height of the plate is defined to be 0.003 m. The plate's material parameters are given in table 5.3. The same example was also used in [Yang 2018] for verifying the computation results. An analytical solution for the depicted problem is given in [Fahy and Gardonio 2007].

Young's modulus	$E_e = 2 \cdot 10^{11} \text{ Pa}$
Density	$\rho_e = 7800 \frac{\text{kg}}{\text{m}^3}$
Poisson's ratio	$\nu_e = 0$

**Table 5.3:** Material parameters of studied plate.

Figure 5.25 shows the transmission loss for the plate being excited by a plane wave that is inclined by an angle of  $50^\circ$ . Both, the outcome of the WFEM approach and the analytical solution are given and a good agreement of the results can be observed.

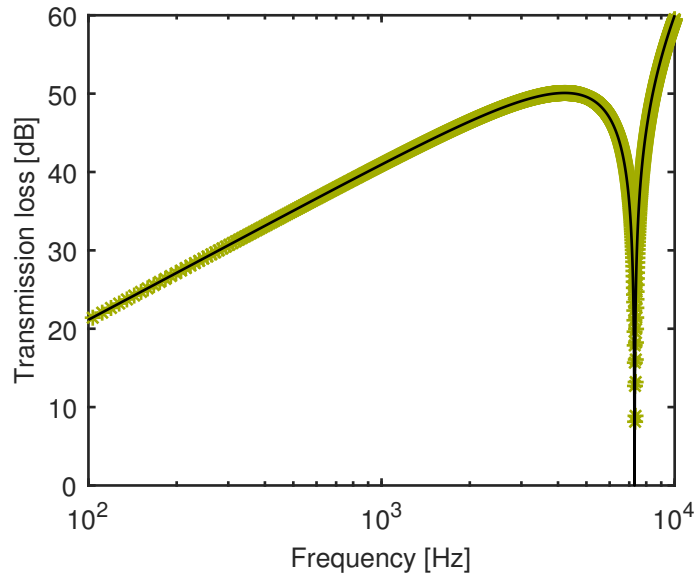


**Figure 5.25:** Transmission loss through plate for excitation with plane wave inclined by  $50^\circ$ : analytical solution (—), WFEM (\* \* \*).

The dip in the transmission loss corresponds to the coincidence frequency. Here, the lateral wavenumber of the excitation corresponds to the wavenumber of the bending wave within the plate. Thus, the plate is set into resonance. The dynamic stiffness of the plate is zero, resulting in a vanishing transmission loss.

### Surface impedance of porous layer

To evaluate the results obtained with the solution approach suggested in section 4.4.4, the surface impedance of a porous layer with infinite lateral extension supported by a rigid backing is computed. The thickness  $h$  of the porous layer corresponds to 0.1 m; the material parameters are given in table 5.4. The structure is excited by a normal incidence plane wave. The problem is sketched in figure 5.26.

Equation (4.56) can be solved for the normal solid and fluid displacements at the top of the porous layer under the given excitation. From that the surface impedance can be computed

via

$$Z_n = \frac{1}{i\omega(\Phi u_{f,n} + (1 - \Phi)u_{s,n})}. \quad (5.3)$$

A reference solution to this problem is given in [Atalla et al 1998].

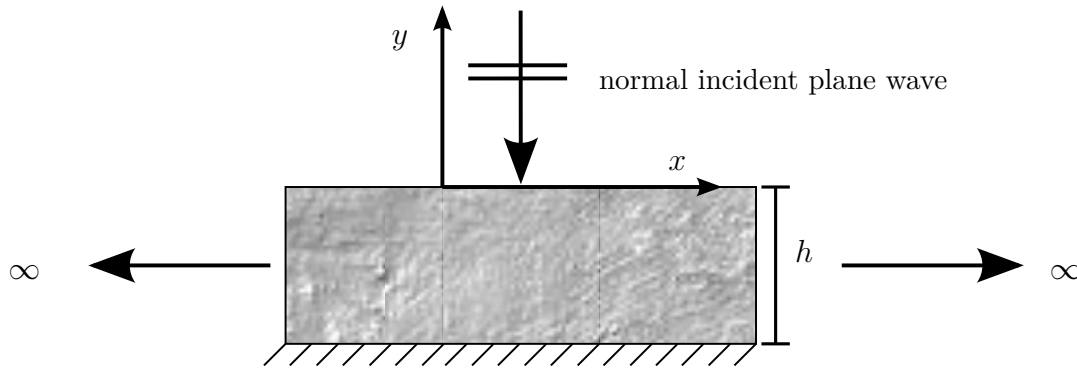


**Figure 5.26:** Porous layer excited by normal incident plane wave.

<b>Solid frame</b>	$\rho_s = 2167 \frac{\text{kg}}{\text{m}^3}$ $\lambda_s = 0 \text{ Pa}$ $\mu_s = 2200 \cdot 10^3 \text{ Pa}$ $\eta_s = 0.1$
<b>Fluid phase</b>	$\rho_f = 1.21 \frac{\text{kg}}{\text{m}^3}$ $\eta = 1.84 \cdot 10^{-8} \frac{\text{Ns}}{\text{m}^2}$ $P_0 = 101 \cdot 10^3 \text{ Pa}$ $\gamma = 1.4$ $Pr = 0.71$
<b>Porous domain</b>	$\Phi = 0.94$ $\alpha_\infty = 1.06$ $\sigma = 40 \cdot 10^3 \frac{\text{Ns}}{\text{m}^4}$ $\Lambda = 56 \cdot 10^{-6} \text{ m}$ $\Lambda' = 110 \cdot 10^{-6} \text{ m}$

**Table 5.4:** Material parameters of porous absorber.

Figures 5.27 and 5.28 show the real and imaginary part of the surface impedance of the studied porous layer according to different solution approaches. The value of the reference solution given in [Atalla et al 1998] deviates from the results obtained using the WFEM. Only the basic course of the curves, including the position of the peaks, is the same. Especially for frequencies below 500 Hz, the deviation of the results obtained with the WFEM using classical and reduced classical formulation are small. Thus, in this lower frequency range using the reduced classical formulation is an appropriate strategy to save computational

effort. Figures 5.29 and 5.30 give detailed insight into the simplification of the material model introduced when using the reduced classical formulation instead of the classical formulation. We can see, that the approximation error introduced by the linearisation of the bulk modulus is much higher than the error introduced by the linearisation of the viscous drag. Within figures 5.29 and 5.30 an orange line marks the value of the respective material dependent dimensionless frequency ratio for  $f = 500$  Hz. The reduced classical formulation performs best for  $\frac{\omega}{H_1} < 0.11 \cap \frac{\omega}{H_2} < 0.07$ .  $H_1$  and  $H_2$  are material dependent parameters which are defined in equations (3.46) and (3.47).

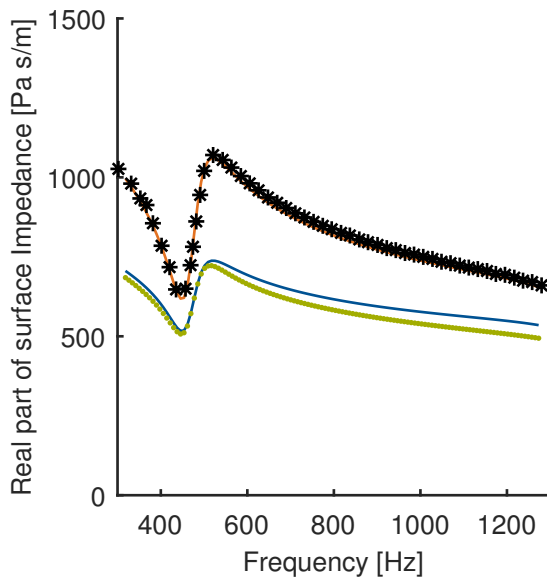


**Figure 5.27:** Real part of surface impedance of porous layer according to [Atalla et al 1998] (\*\*\*), WFEM with classical formulation (—), WFEM with reduced classical formulation (· · ·) and unit cell model with fixed lateral displacements and  $p_\tau = 0$  (—).

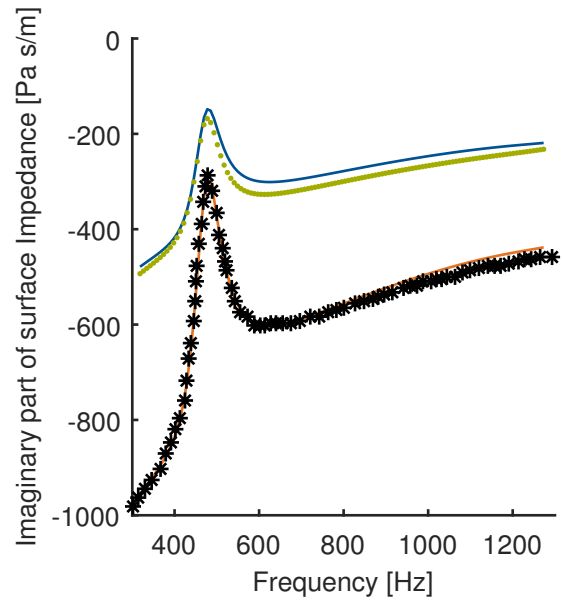


**Figure 5.28:** Imaginary part of surface impedance of porous layer according to [Atalla et al 1998] (\*\*\*), WFEM with classical formulation (—), WFEM with reduced classical formulation (· · ·) and unit cell model with fixed lateral displacements and  $p_\tau = 0$  (—).

To explain the quantitative deviation between WFEM and reference solution another calculation is performed. As input geometry we use the unit cell that we also use for the WFEM analysis. Instead of applying periodic boundary conditions, we set all lateral displacements to zero. The normal incidence plane wave is considered as right hand side for the top nodes. The reflection of the wave is not considered in the model ( $p_\tau = 0$ ). Computing the surface impedance for the described model gives almost exactly the same result as given in [Atalla et al 1998]. On this basis, we assume that the difference between the reference solution and



the WFEM is because the reference solution neglects that a part of the incoming wave is reflected. Thus, the calculation result obtained by the WFEM would correspond to a more realistic model than the reference solution. Since the deviation from the reference solution can be explained, the calculation results obtained by the WFEM approach are classified as plausible.

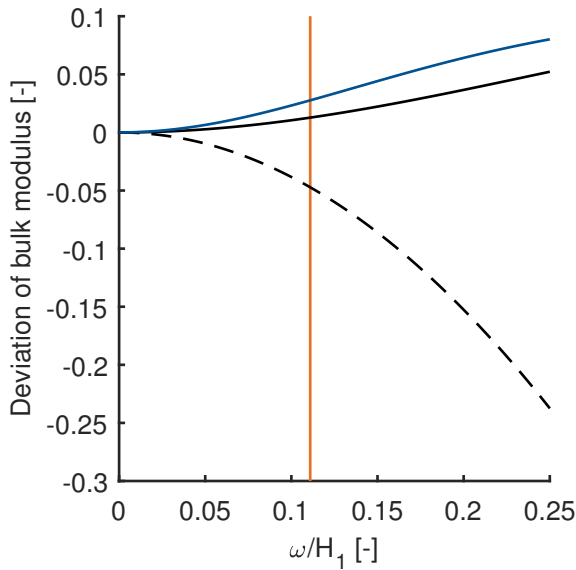


**Figure 5.29:** Deviation of linearised equivalent bulk modulus from exact solution: real part (—), imaginary part (- - -) and absolute value (—); (—) marks dimensionless frequency ratio for  $f = 500$  Hz.

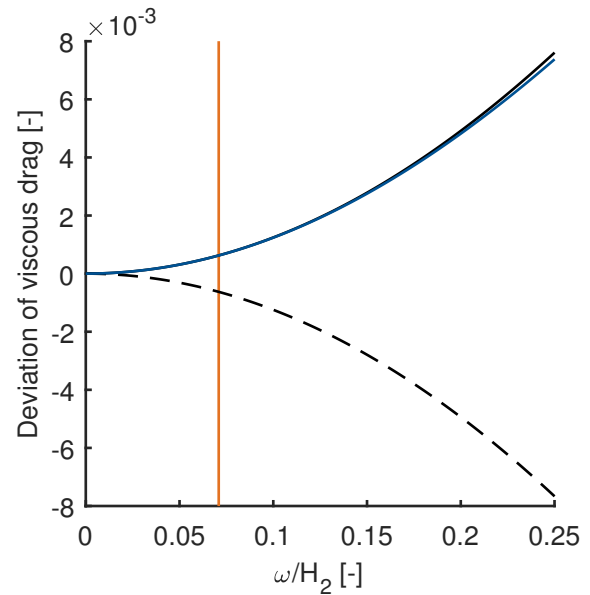


**Figure 5.30:** Deviation of linearised viscous drag from exact solution: real part (—), imaginary part (- - -) and absolute value (—); (—) marks dimensionless frequency ratio for  $f = 500$  Hz.

### 5.3.2 Impact of inclusions on the sound transmission loss through linear elastic structures

In this section, the unit cells shown in figure 5.3 are examined again. Material and dimensions correspond to section 5.2.2. This time, not the wave propagation along the structure, but the sound transmission through the structure is studied. The structures are all exited by a plane wave inclined by an angle of  $\frac{\pi}{4}$  rad.

Figure 5.31 shows the transmission loss computed for the studied cell geometries for a frequency range between 100 and 1000 Hz. For comparison, the transmission loss corresponding to a structure of the same height and material but without inclusion is given.

The dip in the respective transmission loss curve marks the limit frequency (or coincidence frequency) at oblique incidence with  $\Theta = \frac{\pi}{4}$  rad. At this frequency, the horizontal component of the wavelength of the excitation corresponds to the wavelength of the bending wave propagating within the structure. Thus, the bending wave is excited easily and with high amplitude [Lerch et al 2009]. The strong oscillations within the structure lead to a low transmission loss at this frequency.

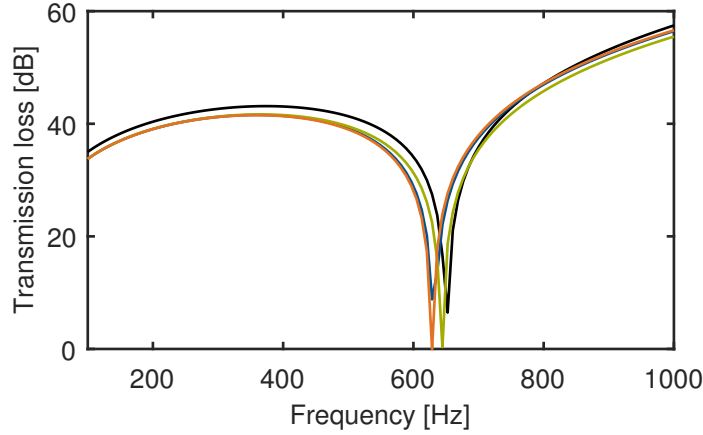


**Figure 5.31:** Transmission loss for excitation with plane wave inclined by  $\frac{\pi}{4}$  rad and structure with circular inclusions (—), rectangular inclusions (—), rhombic inclusions (—) and without inclusions (—); frequency range between 100 and 1000 Hz.

For the limit case of  $\Theta = \frac{\pi}{2}$  rad, [Müller and Möser 2004] gives an analytical expression for estimating the limit frequency of plate like structures:

$$f_c \approx \frac{6.4 \cdot 10^3}{h} \sqrt{\frac{\rho_e}{E_e}}; \quad (5.4)$$

with  $h$  corresponding to the thickness of the plate.

For an oblique incident excitation, [Lerch et al 2009] states that at the limit frequency

$$c_B = \frac{c_{\text{air}}}{\sin(\Theta)}. \quad (5.5)$$

From table 2.1 we know that

$$c_B = A\sqrt{\omega}, \quad (5.6)$$

where  $A$  is given by the dimensions of the structure and the material it is made of. The expression for  $A$  depends on if the studied geometry corresponds to a plate or a beam.

With  $\omega = 2\pi f$  we find that for normal incidence

$$A\sqrt{2\pi f_c} = c_{\text{air}}, \quad (5.7)$$

and for oblique incidence

$$A\sqrt{2\pi f_{c,\Theta}} = \frac{c_{\text{air}}}{\sin(\Theta)}. \quad (5.8)$$

Solving equation (5.7) and (5.8) for  $c_{\text{air}}$  and setting the results equal, we can find the following relationship between the coincidence frequency at oblique incidence  $f_{c,\Theta}$  and  $f_c$ :

$$f_{c,\Theta} = \frac{f_c}{\sin(\Theta)^2}. \quad (5.9)$$

For the homogeneous structure without inclusions, we can find  $f_{c,\Theta} = 628.35$  Hz. The value of the numerical solution is slightly higher. This mismatch results from the fact that equation (5.9) gives only an approximative value for the coincidence frequency at oblique incidence for thin plate like structures. Still, the analytical estimation of the limit frequency shows that the result of the numerical calculation is plausible.

Overall, for the frequency range shown in figure 5.31, the impact of the inclusions is small compared to the structure without inclusions, as only the coincidence frequency is shifted slightly towards lower frequencies. We can see that for structures of the same mass, the inclusion shape has an impact on the value of the coincidence frequency. The coincidence frequency corresponding to the structure with rectangular inclusions is higher than the one for the structures with circular and rhombic inclusions. For the structures with circular and rhombic inclusions, the coincidence frequency  $f_{c,\Theta}$  is almost the same when excited by a plane wave inclined by an angle of  $\frac{\pi}{4}$  rad.

Knowing that the coincidence frequency is proportional to the quotient of mass and stiffness (equation (5.4)), we would expect that the reduction in mass due to the inclusion leads to a significant reduction of the coincidence frequency. But, as embedding the inclusion at the same time lowers the structures stiffness, we only observe a slight reduction of the coincidence frequency. The inclusions leading to a reduction of the coincidence frequency tells that the impact of the reduction in mass predominates the effect of the reduced stiffness. As the reduction in mass is the same for all inclusion shapes, the difference in the coincidence frequency is determined by the reduction in stiffness which is not necessarily the same for the considered inclusion shapes.

To show that the coincidence frequency is not only affected by the mass of the structure, an additional analysis is performed. The system with inclusions is replaced by a homogeneous structure of the same thickness and mass. This gives an equivalent density of  $\rho_{\text{eq}} = 2346 \frac{\text{kg}}{\text{m}^3}$ . Figure 5.32 shows the transmission loss corresponding to this configuration. Here, besides the result of the WFEM calculation, the result of an analytical expression given in [Fahy and Gardonio 2007] is depicted. As expected, only taking into account the mass reduction due to the inclusions (without simultaneous consideration of the reduction in stiffness) leads to a lower coincidence frequency. The discrepancy between numerical and analytical calculation can be explained by the fact that the analytical solution covers only rather thin plate like structures. The configuration considered here is obviously at the border of the application range of the plate theory.

Figure 5.33 shows the transmission loss for the different inclusion geometries and the homogeneous structure for a frequency range between 100 and 45 000 Hz. For frequencies above 2500 Hz, there is a clear impact of the inclusions. In comparison to the homogeneous structure, multiple peaks and dips in the course of the transmission loss can be seen for all studied inclusion geometries. The frequency dips can be attributed to higher order resonances. For frequencies above 20 000 Hz, the transmission loss of the structures with inclusions is smaller than for the homogeneous structure. According to [Müller and Möser 2004], the reduction of the transmission loss due to the inclusions results from resonances of the limiting parts of the inclusions and thickness resonances of the structure induced by the reduction in stiffness.

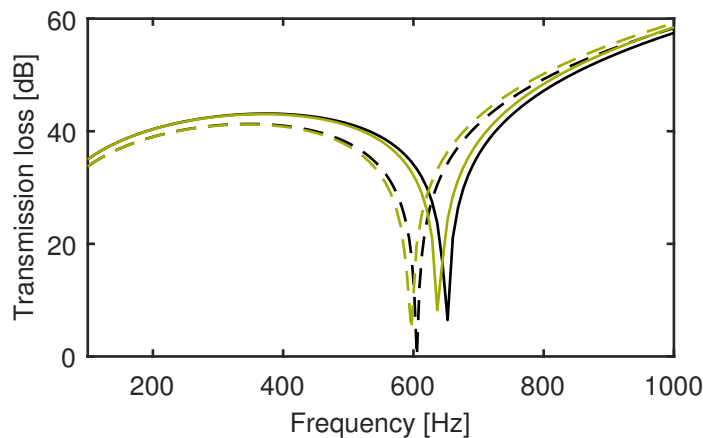


**Figure 5.32:** Transmission loss for excitation with plane wave inclined by  $\frac{\pi}{4}$  rad for homogeneous structure with full density (—) and reduced equivalent density (- -); black curve corresponds to WFEM results, green curve to analytical solution given in [Fahy and Gardonio 2007].

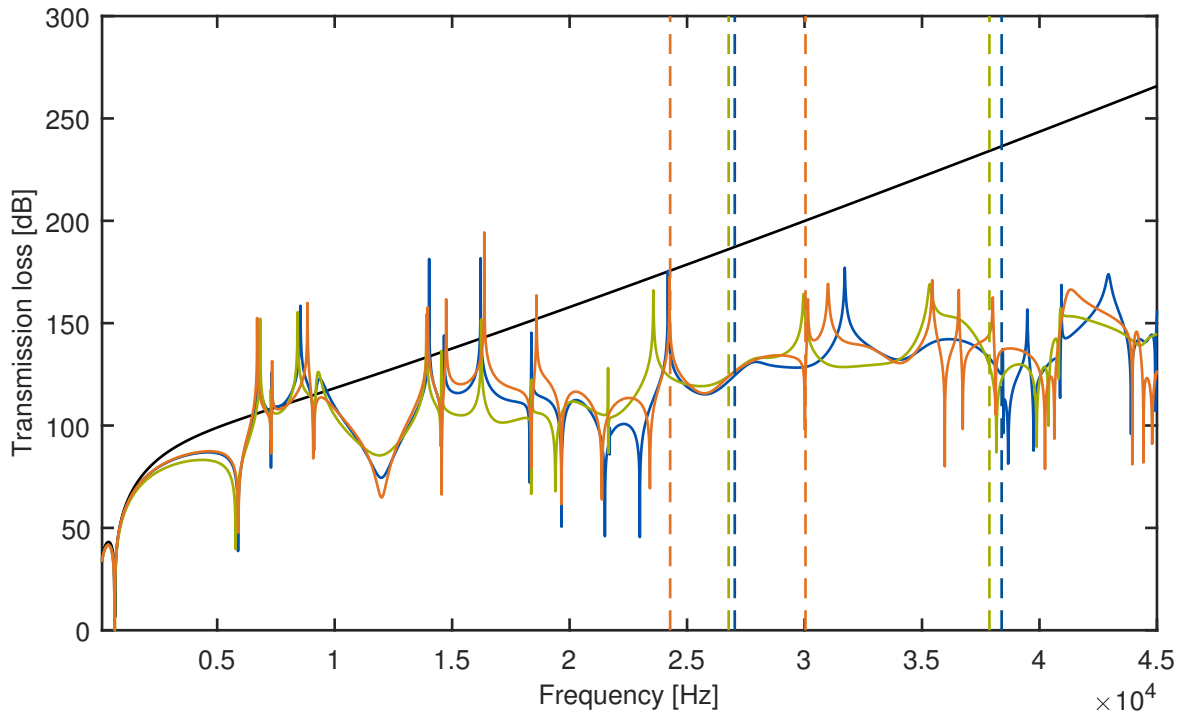


**Figure 5.33:** Transmission loss for excitation with plane wave inclined by  $\frac{\pi}{4}$  rad and structure with circular inclusions (—), rectangular inclusions (—), rhombic inclusions (—) and without inclusions (—); upper and lower limits of stop bands computed for different inclusion shapes in section 5.2.2 are marked by dashed vertical lines.

Also in the frequency ranges where stop bands were observed when studying the wave propagation along the structure in section 5.2.2, the transmission loss is lowered due the inclusions. However, no dips in the transmission loss curve (higher order resonances) occur in the stop band areas. It can be concluded that an inclusion design that effectively suppresses the propagation of structure borne sound in certain frequency ranges, can suffer from an increase in airborne sound transmission in these frequency ranges.

### 5.3.3 Dispersion characteristics of periodically structured porous metamaterials

To demonstrate the possibilities offered by the approach suggested in section 4.4.4, the dispersion characteristics of two different porous metamaterials with inclusions are studied. First, the impact of point mass inclusions on the sound absorption of a rigidly backed porous layer is evaluated. Next, it is studied whether the sound transmission through two-shell walls can be manipulated by inclusions.

### Absorption characteristics of porous absorber with mass inclusions

Subsequently, the absorption characteristics of the porous metamaterial depicted in figure 5.34 are evaluated. The unit cell is quadratic with an edge length of 0.02 m. Small mass inclusions with negligible spatial extension are located at the height  $h_m$ . The material parameters of the porous domain are given in table 3.4. The inclusions have a mass of  $m = 0.004$  kg. This corresponds to a steel rod with a radius of 0.4 mm. In the FEM model, the mass inclusions are represented by concentrated mass elements. [Zielinski 2007] proves that for small mass inclusions within porous media this representation is almost equivalent to the employment of small elastic subdomains. The structure is excited by a plane wave inclined by an angle of  $\Theta = \frac{\pi}{4}$  rad.

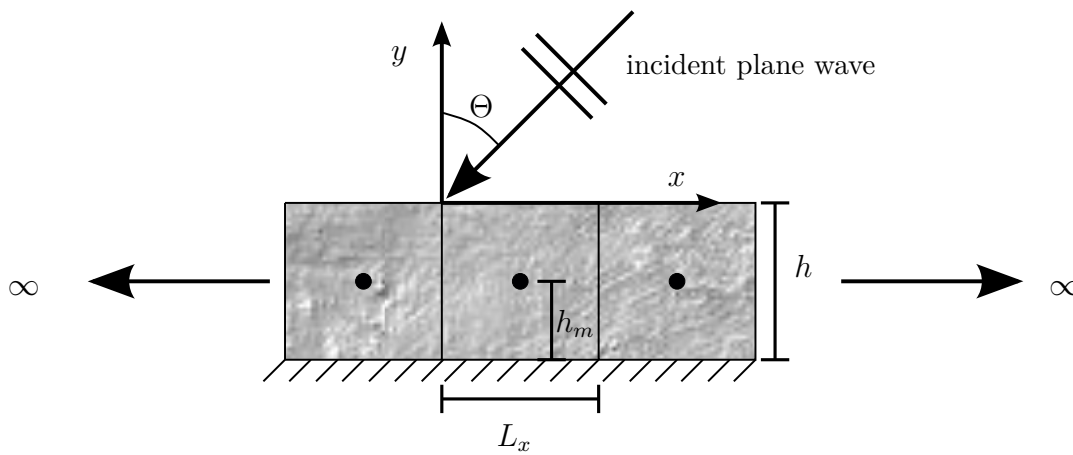


**Figure 5.34:** Porous metamaterial with concentrated mass inclusions.

Compared to [Zielinski 2007] and [Ahsani et al 2020], where a comparable structure is excited by a normal incident plane wave, in this work an oblique incident wave is modelled to be able to represent additional phenomena that may occur. Figure 5.35 compares the absorption coefficient of the rigidly backed porous layer without inclusions for the excitation with a normal incident plane wave and a plane wave inclined by  $\Theta = \frac{\pi}{4}$  rad. The frequency of the major absorption dip is the same. As the oblique incident wave excites additional wave patterns, additional absorption maxima and minima can be observed within the considered frequency range.

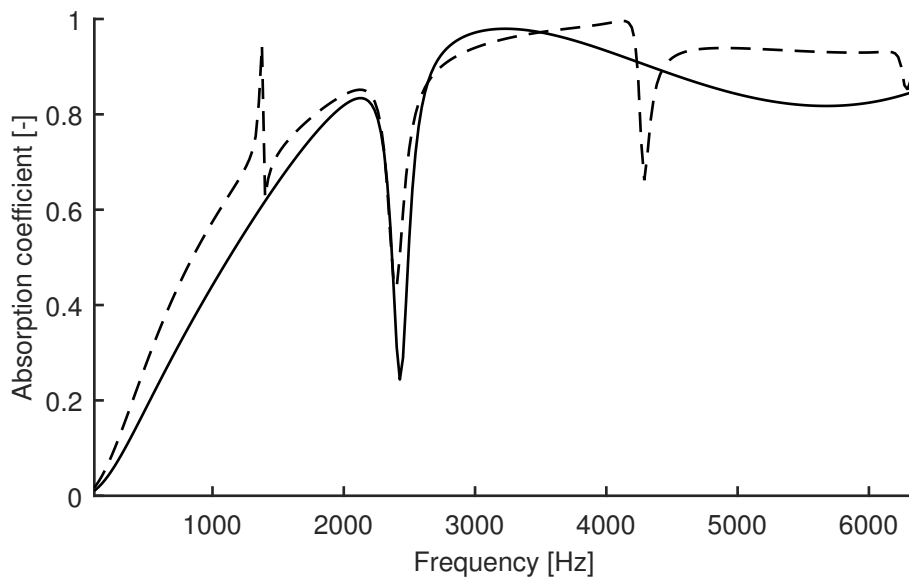


**Figure 5.35:** Absorption coefficient of porous layer without inclusions for  $\Theta = \frac{\pi}{4}$  rad (---) and  $\Theta = 0$  rad (—).

Figure 5.36 shows the absorption coefficient for the rigidly backed porous layer with mass inclusions at different heights. For comparison, the absorption coefficient of the structure without inclusions is also given. It can be seen that the absorption dip that occurs at 2380 Hz for the configuration without inclusions is replaced by two absorption dips left and right to the original one when embedding inclusions into the porous layer. The spacing of these new absorption dips depends on the location of the inclusion within the unit cell. It is observed that the greater  $h_m$ , the larger the distance of these absorption dips. The mass inclusion can be understood as an equivalent oscillator. The higher the inclusion is located within the unit cell, the lower the spring stiffness.

In figure 5.36, the frequency for which the thickness of the porous layer equals one quarter of the vertical component of the wavelength of the excitation is marked. According to [Deckers et al 2016], the excitation in an adjacent sound field is damped efficiently by a rigidly supported porous absorber above this frequency. The course of the absorption coefficient confirms this statement.

As also shown in [Zielinski 2007] and [Ahsani et al 2020], the inclusions result in both, frequency ranges with improved and deteriorated absorption. [Ahsani et al 2020] shows that by optimizing the inclusion configuration, it is possible to improve the absorption over a wide frequency range. This is not the subject of this work. The aim here only is to show the broad range of possible applications of the numerical solution method introduced in section 4.4.4.

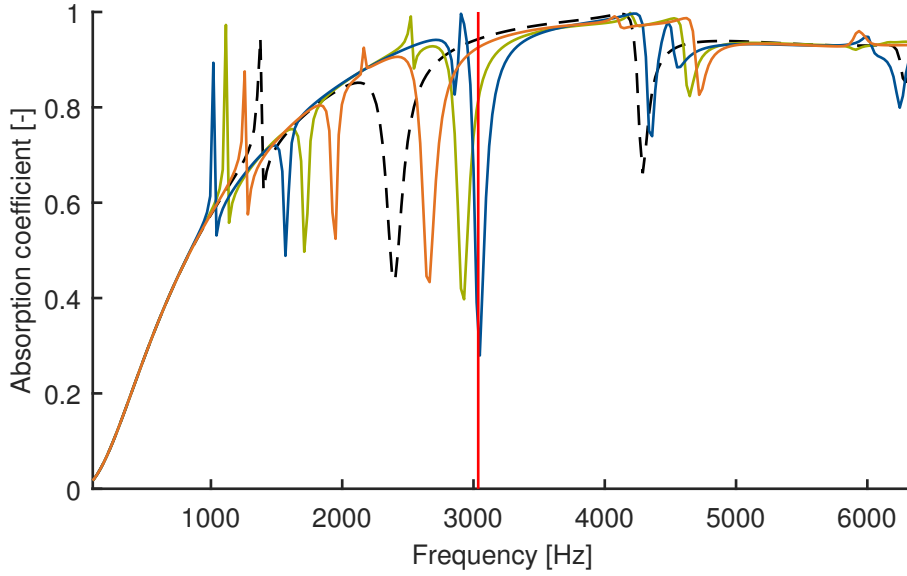


**Figure 5.36:** Absorption coefficient of porous metamaterial with concentrated mass inclusions at different heights:  $h_m = 0.015$  m (—),  $h_m = 0.010$  m (—),  $h_m = 0.005$  m (—) and without inclusions (- -); (—) marks frequency for which thickness of porous layer equals one quarter of vertical component of wavelength of excitation.

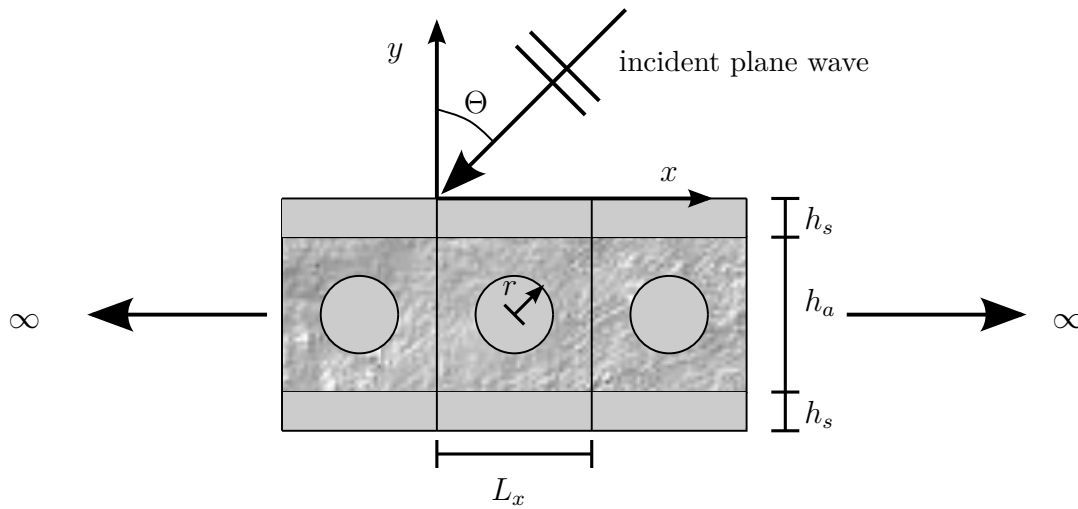
### Sound transmission through two-shell wall with inclusions

Figure 5.37 shows the geometry of a two-shell wall with circular inclusions. The inclusions are located in the centre of the unit cell. For the following computations, the dimensions specified in table 5.5 are employed. The dimensions of the two-shell wall itself correspond to a typical structure as found, for example, in [Müller and Möser 2004]. The insulation layer consists of glass wool with the material parameters for the JCAM being specified in table 5.4. The outer shells are gypsum board walls. The material properties are summarized in table 5.6 and were taken from [Späh and Lutz 2015]. The sound transmission through the structure is computed for the excitation with a plane wave inclined by an angle of  $\Theta = \frac{\pi}{4}$  rad.

Length of unit cell	$L_x = 0.05$ m
Thickness of outer shells	$h_s = 0.0125$ m
Thickness of insulation layer	$h_a = 0.05$ m
Radius of inclusion	$r = 0.01$ m

**Table 5.5:** Dimensions of two-shell wall with inclusions.





**Figure 5.37:** Two-shell wall with inclusions.

Young's modulus	$E_e = 1.7 \text{ GPa}$
Density	$\rho_e = 696 \frac{\text{kg}}{\text{m}^3}$
Poisson's ratio	$\nu_e = 0.2$

**Table 5.6:** Material parameters of gypsum board.

According to [Fasold and Veres 2003], the two-shell wall without inclusions can be interpreted as a system of two masses connected by a spring. The outer cells are the masses and the insulation layer acts as spring. The inclusions within the insulation layer can be seen as intermediate masses. The first dip in the transmission loss curve corresponds to the resonance frequency of the system. Here, the outer walls are oscillating in antiphase [Lerch et al 2009].

Figure 5.38 compares the transmission loss of three different configurations: a two-shell wall without inclusions, a two-shell wall with inclusions made of aluminium and a two-shell wall with inclusions made of gypsum board. We can see that the resonance frequency is shifted towards higher frequencies for the configurations with inclusions. Below the resonance frequency, the transmission loss is slightly higher for the configurations with inclusions, whereby the aluminium inclusions lead to a higher transmission loss than the gypsum board inclusions. Above the resonance frequency, we can find frequency ranges where the inclusions lead to an improvement of the transmission loss, but also frequency ranges where the transmission loss for the configurations with inclusions is lower than for the configuration without inclusions. On average, the transmission loss is higher for the configurations with inclusions than for the configuration without inclusions. It can be stated that the transmission loss

curve is changed as a result of the inclusions and that the filling material of the inclusions has an impact on the sound transmission.

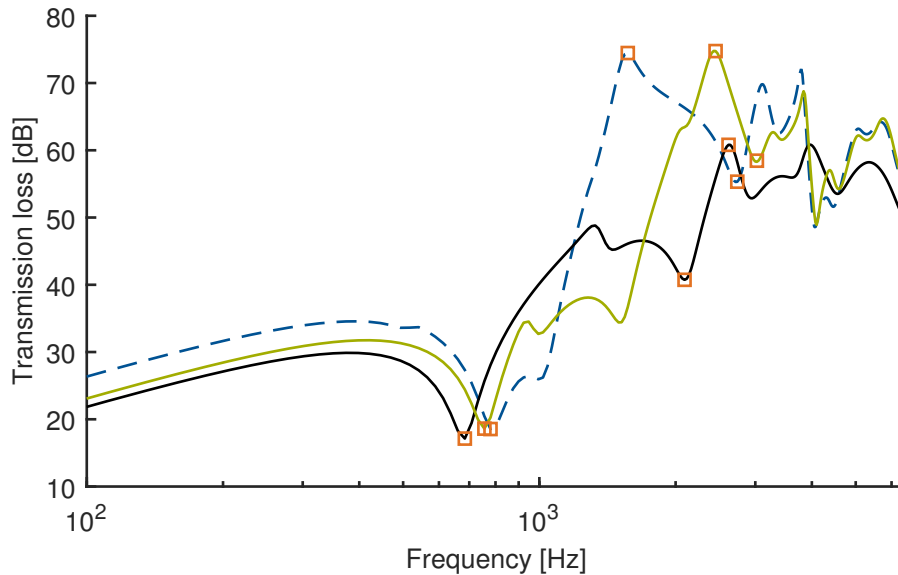


**Figure 5.38:** Transmission loss of two-shell wall: with aluminium inclusions (---), with gypsum board inclusions (—) and without inclusions (—);  $\square$  marks frequencies for which deformation pattern is plotted in figures 5.39-5.41.

Figures 5.39-5.41 show the deformed periodic structure for the frequencies marked in figure 5.38. In accordance to [Lerch et al 2009], we can see the antiphase oscillation of the two outer shells at the resonance frequencies of the systems in figures 5.39-5.41 a). The marked maxima of the transmission loss can be explained by low deformations of the systems (deformation patterns b)). While the upper part of the systems is slightly deformed, the lower part undergoes almost no deformation. In [Fasold and Veres 2003] it is indicated that the transmission loss dips in the higher frequency range correspond to cavity resonances within the insulation layer. This is confirmed by the deformation patterns c) in figures 5.39-5.41.

The influence of the filling of the inclusions on the transmission curve and also the deformation patterns of the studied metamaterial designs show that it is important to consider the elastic deformations of the inclusion itself and of the solid phase of the porous layer in the model. In comparison to most approaches from the literature, this is possible in the solution procedure shown in the context of this thesis.

The research results presented here indicate the potential for detailed follow-up parameter studies investigating the correlation between the sound transmission and the inclusion shape, size, location, spacing and filling material. Based on these results, it would be possible

to design inclusions tailored to specific applications in order to optimize the vibroacoustic properties of two-shell walls.

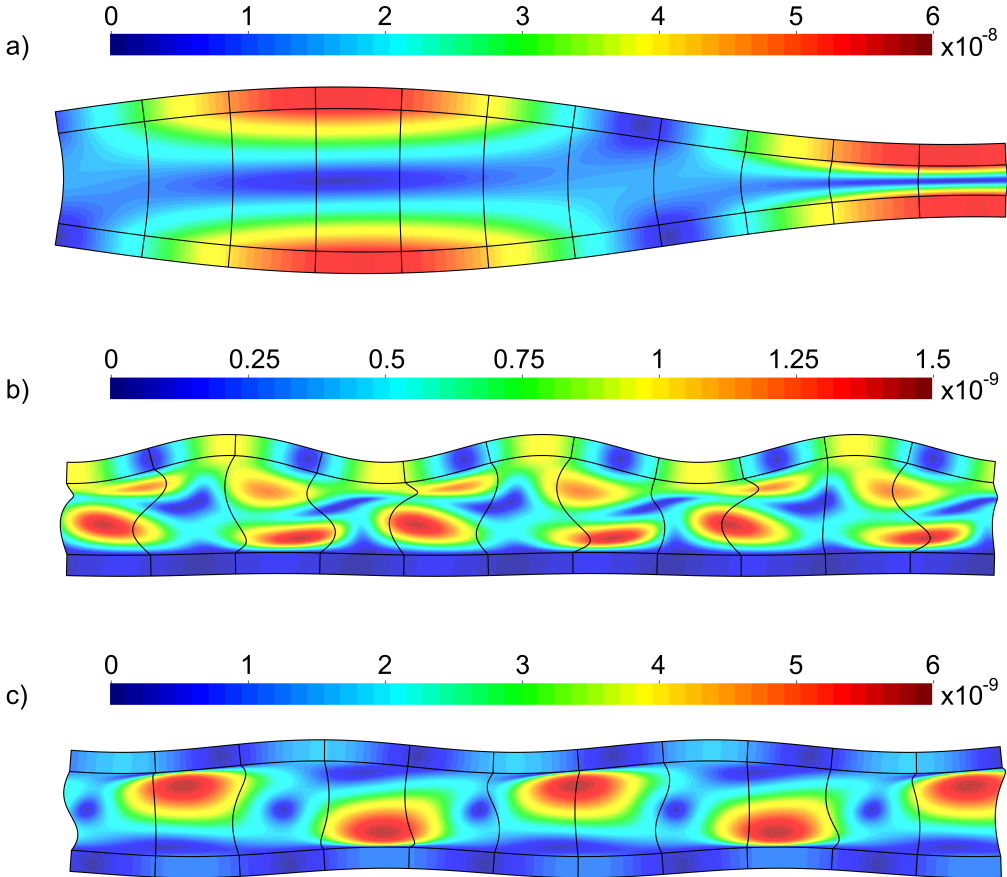


**Figure 5.39:** Deformation pattern of two-shell wall without inclusions for different frequencies: a) 684 Hz, b) 2618 Hz and c) 2093 Hz; for porous domain solid phase displacements are depicted.

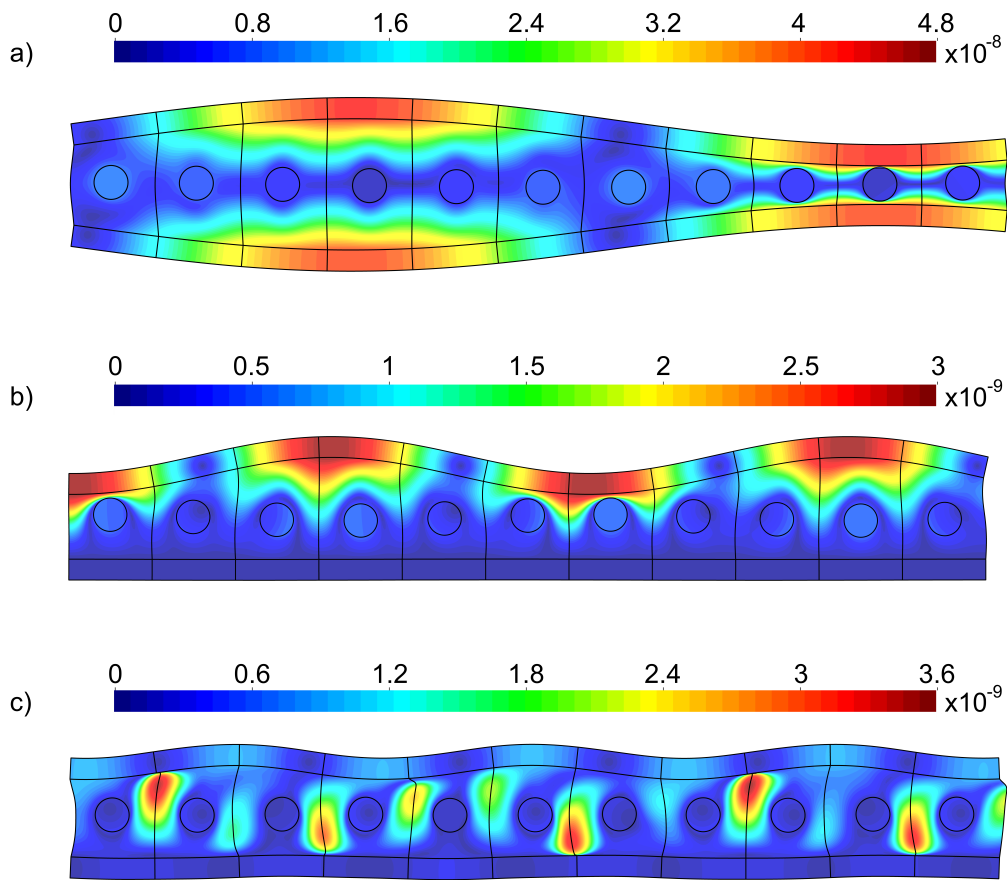


**Figure 5.40:** Deformation pattern of two-shell wall with aluminium inclusions for different frequencies: a) 780 Hz, b) 1568 Hz and c) 2737 Hz; for porous domain solid phase displacements are depicted.

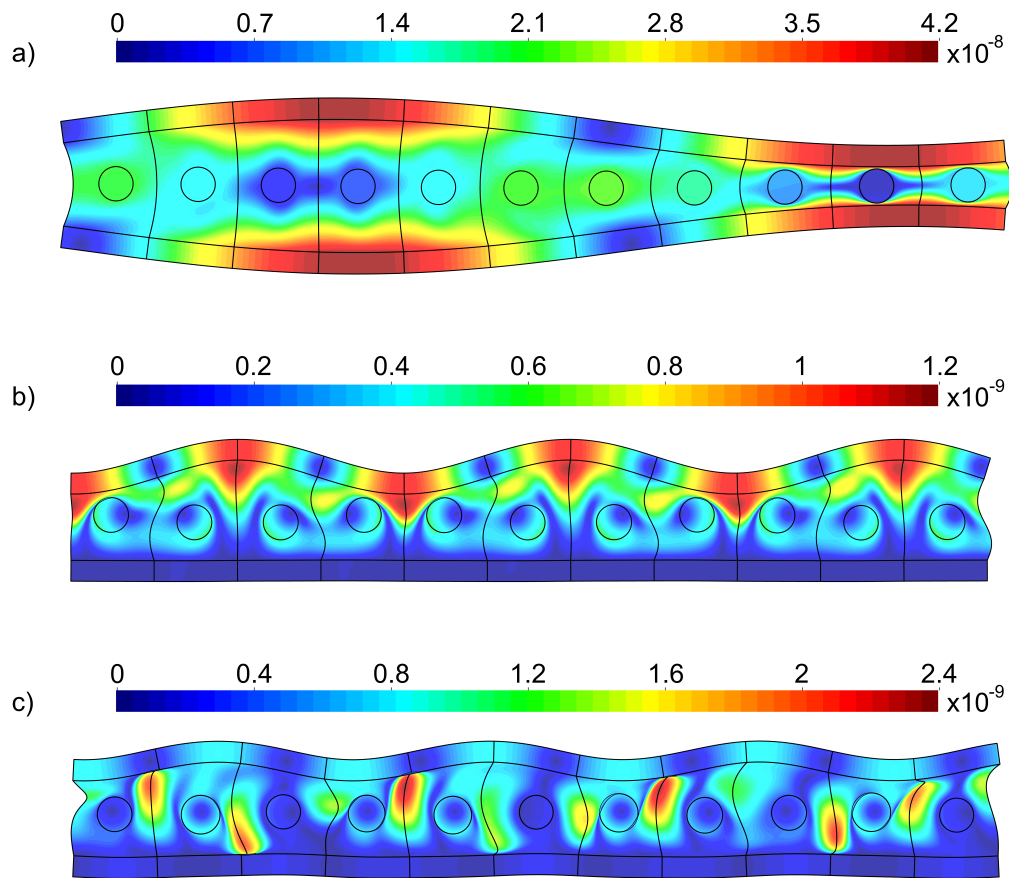


**Figure 5.41:** Deformation pattern of two-shell wall with gypsum board inclusions for different frequencies: a) 756 Hz, b) 2451 Hz and c) 3024 Hz; for porous domain solid phase displacements are depicted.

## 5.4 Conclusion

This chapter verifies the solution strategies proposed in chapter 4 (and their numerical implementation) by comparing the results for reference configurations from the literature. The potential of inclusions and local resonators to improve the vibroacoustic properties of dynamic systems is demonstrated using several example designs. It is noticeable that the optimization of airborne sound transmission and structure-borne sound propagation can often be interests that are difficult to combine and a metamaterial design may not be able to meet both requirements optimally at the same time.

## 6 Conclusion

### 6.1 Summary of the presented modelling strategies for acoustic metamaterials

This thesis starts with explaining how vibroacoustic systems consisting of acoustic cavities, linear elastic solids and porous absorbers can be modelled numerically using the FEM. Special attention was paid to the mapping of boundary and coupling conditions. In the context of this thesis, the JCAM serves as material model for the porous domain. Existing formulations of the JCAM are presented and compared along with a novel simplified formulation. It is shown that while involving significantly less computational effort than a full model, this simplified version provides sufficiently accurate results for many applications. Subsequently, it is explained how the wave propagation along a periodic structure and the sound transmission through a periodic structure can be computed on the basis of a FEM model of a unit cell and periodic boundary conditions using the WFEM. Thereby this thesis introduces a novel approach to compute the sound transmission through and absorption of periodic structures with elastic frame porous boundary layers. Using the approach shown, it is possible to analyse the dispersion properties of acoustic metamaterials with complex geometries and porous components. In comparison to the approaches existing in the literature, the proposed method meets all of the following requirements at the same time: the elastic solid displacements of the absorber are mapped, the system can not only be excited by normal incident but also by inclined plane waves and the reflection of the incident wave at the top of the structure is represented.

## 6.2 Main findings of the numerical studies on exemplary structures

This sections summarizes the main findings obtained in the numerical studies carried out in the context of this thesis.

### Wave propagation along periodic structures with inclusions

- A correlation between the variance in mass distribution along the unit cell and the stop band width can be found.
- For configurations with the same variance in mass distribution, the stop band location and width is influenced by the inclusion shape.
- Resonators within the inclusions can be used to deflect the waves propagating within the structures. Here, the relationship between the direction of oscillation of the resonator and the direction of wave motion of the respective wave type is decisive.

### Sound transmission through periodic structures with inclusions

- Not only the wave propagation along the structure but also the sound transmission through the structure is influenced by the inclusions.
- For the studied configurations, the coincidence frequency was slightly shifted for the configurations with inclusions in comparison to the structure without inclusions.
- For all studied configurations with inclusions, the sound transmission loss in the frequency range of the stop bands was smaller than for the configuration without inclusions. Thus, we can conclude that an inclusion design that impedes structure borne noise propagation in a certain frequency range may suffer from unfavourable sound transmission characteristics in this frequency range compared to a structure without inclusions.

### Dispersion characteristics of porous absorbers with inclusions

- Mass inclusions can be used to manipulate the low frequency absorption of porous absorbers. The mass inclusion acts like a single-mass oscillator, with the spring stiffness given by the material thickness below the mass. The higher the inclusion within the porous layer, the lower the spring stiffness of the oscillator and the lower its resonance frequency. Thus, the height of the inclusion within the porous layer is decisive for the course of the absorption coefficient.
- The sound transmission through two-shell walls can be altered by embedding inclusions into the insulation layer. With the same shape and position of the inclusion, the filling material of the inclusion has an influence on the course of the transmission loss. This indicates that it is necessary to take into account the elastic deformations of the inclusion itself and of the solid phase of the porous layer in the model.

## 6.3 Outlook

Building on this work, a variety of interesting research topics emerge. The following is a summary of the most promising topics from the author's point of view.

- The solution strategies shown can be used to perform more detailed parameter studies to investigate p.e. the influence of resonant inclusions in porous absorbers. Among others, it could be studied to what extent the coincidence frequency of two-shell walls can be manipulated by enclosed vibrating systems. Thereby it should be examined which characteristics of the inclusion (e.g. mass, position, shape, spacing) affect the sound transmission of the structure and how. For the special application case of a two-shell wall, it should also be investigated whether it is necessary to represent the interior absorbing layer via the JCAM or whether, in this case, a consideration via simple spring elements represents the dynamic behaviour sufficiently accurately. Here, the additional question on how to determine the equivalent spring constant for the porous absorber arises.
- Model order reduction could be integrated into the strategies proposed in chapter 4.4 for the calculation of the sound transmission using the WFEM. As shown in [Zhou et al 2015] and [Van Belle et al 2020] for the conventional WFEM, this could considerably reduce the computational effort and it would be possible to analyse significantly more designs in a shorter time.



- 
- If only the secondary system, e.g. the inclusion, is to be varied for a constant basic structure, substructuring approaches could be used. In this case, only the element matrices for the secondary system would have to be set up again if a new design is to be investigated.
  - After improving the efficiency of the solution strategies shown by suitable approaches, optimization methods could be used with the aid of which an optimum geometry and material distribution can be found for the respective application under the specification of a certain design space.
  - Following [Duhamel et al 2006], it could be investigated how the proposed solution strategies have to be adapted so that spatially bounded systems can be represented in addition to infinitely periodic structures. Thereby special attention has to be paid to how boundary effects can be mapped.
  - Having increased the efficiency of the solution approach, it would be reasonable to transfer the two-dimensional observations made so far to more realistic, but also more costly, three-dimensional models. Here, it should be investigated whether the same dynamic characteristics appear and whether additional phenomena occur.

## Bibliography

- [Adhikari 2001] ADHIKARI, Sondipon: *Damping models for structural vibration*, University of Cambridge, Ph.D. thesis, 2001
- [Ahsani et al 2020] AHSANI, Sepide ; BOUKADIA, R. ; DROZ, C. ; ZIELIŃSKI, T. ; CLAEYS, Claus ; DESMET, Wim ; DECKERS, Elke et al: On the potential of meta-poro-elastic systems with mass inclusions to achieve broadband near-perfect absorption coefficient. In: *ISMA2020 International Conference on Noise and Vibration Engineering, September 07-09, 2020, Leuven, Belgium*, 2020
- [Allard and Atalla 2009] ALLARD, Jean F. ; ATALLA, Noureddine: *Propagation of Sound in Porous Media: Modelling Sound Absorbing Materials*. John Wiley & Sons, Ltd, 2009
- [Atak 2014] ATAĞ, Onur: *Wave Based Modeling Methods for Acoustic Inclusion and Multiple Scattering Problems in the Mid-Frequency Range*, KU Leuven, Ph.D. thesis, 2014
- [Atalla et al 2001] ATALLA, Noureddine ; HAMDI, Mohamed A. ; PANNETON, Raymond: Enhanced weak integral formulation for the mixed ( $u$ ,  $p$ ) poroelastic equations. In: *The Journal of the Acoustical Society of America* 109 (2001), Nr. 6, p. 3065–3068
- [Atalla et al 1998] ATALLA, Noureddine ; PANNETON, Raymond ; DEBERGUE, Patricia: A mixed displacement-pressure formulation for poroelastic materials. In: *The Journal of the Acoustical Society of America* 104 (1998), Nr. 3, p. 1444–1452
- [Bathe 2002] BATHE, Klaus-Jürgen: *Finite-Elemente-Methoden*. Springer, 2002
- [Biot 1955] BIOT, Maurice A.: Theory of elasticity and consolidation for a porous anisotropic solid. In: *Journal of Applied Physics* 26 (1955), Nr. 2, p. 182–185
- [Biot 1956a] BIOT, Maurice A.: Theory of Propagation of Elastic Waves in a Fluid-Saturated Porous Solid. I. Low-Frequency Range. In: *The Journal of the Acoustical Society of America* 28 (1956), Nr. 2, p. 168–178. – ISSN 0001-4966
- [Biot 1956b] BIOT, Maurice A.: Theory of propagation of elastic waves in a fluid-saturated porous solid. II. Higher frequency range. In: *The Journal of the Acoustical Society of America* 28 (1956), Nr. 2, p. 179–191
- [Bloch 1929] BLOCH, Felix: Über die Quantenmechanik der Elektronen in Kristallgittern. In: *Zeitschrift für Physik* 52 (1929), Nr. 7-8, p. 555–600
- [de Boer 2000] BOER, Reint de: *Theory of Porous Media: Highlights in the Historical Development and Current State*. Springer-Verlag Berlin Heidelberg, 2000

- [Boutin and Becot 2015] BOUTIN, Claude ; BECOT, François Xavier: Theory and experiments on poro-acoustics with inner resonators. In: *Wave Motion* 54 (2015), p. 76–99
- [Brillouin 1946] BRILLOUIN, Leon: *Wave propagation in periodic structures*. McGraw-Hill Book Company, 1946
- [Buchschnid 2011] BUCHSCHMID, Martin: *ITM-based FSI-models for rooms with absorptive boundaries*, Technische Universität München, Ph.D. thesis, 2011
- [Champoux and Allard 1991] CHAMPOUX, Yvan ; ALLARD, Jean F.: Dynamic tortuosity and bulk modulus in air-saturated porous media. In: *Journal of Applied Physics* 70 (1991), Nr. 4, p. 1975–1979
- [Chronopoulos et al 2015] CHRONOPOULOS, Dimitrios ; ANTONIADIS, I. ; COLLET, M. ; ICHCHOU, M.: Enhancement of wave damping within metamaterials having embedded negative stiffness inclusions. In: *Wave Motion* 58 (2015), p. 165–179
- [Claeys et al 2017] CLAEYS, Claus ; MELO FILHO, Noé Geraldo R. de ; VAN BELLE, Lucas ; DECKERS, Elke ; DESMET, Wim: Design and validation of metamaterials for multiple structural stop bands in waveguides. In: *Extreme Mechanics Letters* 12 (2017), p. 7–22
- [Claeys et al 2013] CLAEYS, Claus ; VERGOTE, Karel ; SAS, Paul ; DESMET, Wim: On the potential of tuned resonators to obtain low-frequency vibrational stop bands in periodic panels. In: *Journal of Sound and Vibration* 332 (2013), Nr. 6, p. 1418–1436
- [Collet et al 2011] COLLET, Manuel ; OUISSE, Morvan ; RUZZENE, Massimo ; ICHCHOU, M.: Floquet–Bloch decomposition for the computation of dispersion of two-dimensional periodic, damped mechanical systems. In: *International Journal of Solids and Structures* 48 (2011), Nr. 20, p. 2837–2848
- [Craig Jr and Bampton 1968] CRAIG JR, Roy R. ; BAMPYTON, Mervyn C.: Coupling of substructures for dynamic analyses. In: *AIAA Journal* 6 (1968), Nr. 7, p. 1313–1319
- [Cremer and Heckl 2013] CREMER, Lothar ; HECKL, Manfred: *Körperschall: physikalische Grundlagen und technische Anwendungen*. Springer-Verlag, 2013
- [Cremer and Müller 1982] CREMER, Lothar ; MÜLLER, Helmut A.: *Principles and Applications of Room Acoustics*. Applied Science, 1982
- [Dauchez et al 2001] DAUCHEZ, Nicolas ; SAHRAOUI, Sohbi ; ATALLA, Noureddine: Convergence of poroelastic finite elements based on Biot displacement formulation. In: *The Journal of the Acoustical Society of America* 109 (2001), Nr. 1, p. 33–40
- [Dazel et al 2009] DAZEL, Olivier ; BROUARD, Bruno ; DAUCHEZ, Nicolas ; GESLAIN, Alan: Enhanced Biot’s finite element displacement formulation for porous materials and original resolution methods based on normal modes. In: *Acta Acustica united with Acustica* 95 (2009), Nr. 3, p. 527–538
- [Dazel et al 2007] DAZEL, Olivier ; BROUARD, Bruno ; DEPOLLIER, Claude ; GRIFFITHS, Stéphane: An alternative Biot’s displacement formulation for porous materials. In: *The Journal of the Acoustical Society of America* 121 (2007), Nr. 6, p. 3509–3516

- [Debergue et al 1999] DEBERGUE, Patricia ; PANNETON, Raymond ; ATALLA, Nouredine: Boundary conditions for the weak formulation of the mixed (u, p) poroelasticity problem. In: *The Journal of the Acoustical Society of America* 106 (1999), Nr. 5, p. 2383–2390
- [Deckers et al 2014] DECKERS, Elke ; ATAK, Onur ; COOX, Laurens ; D'AMICO, Roberto ; DEVRIENDT, Hendrik ; JONCKHEERE, Stijn ; KOO, Kunmo ; PLUYMERS, Bert ; VANDEPITTE, Dirk ; DESMET, Wim: The wave based method: An overview of 15 years of research. In: *Wave Motion* 51 (2014), Nr. 4, p. 550–565
- [Deckers et al 2016] DECKERS, Elke ; CLAEYS, Claus ; ATAK, Onur ; GROBY, Jean-Philippe ; DAZEL, Olivier ; DESMET, Wim: A wave based method to predict the absorption, reflection and transmission coefficient of two-dimensional rigid frame porous structures with periodic inclusions. In: *Journal of Computational Physics* 312 (2016), p. 115–138
- [Deckers et al 2012] DECKERS, Elke ; HÖRLIN, Nils-Erik ; VANDEPITTE, Dirk ; DESMET, Wim: A Wave Based Method for the efficient solution of the 2D poroelastic Biot equations. In: *Computer Methods in Applied Mechanics and Engineering* 201 (2012), p. 245–262
- [Deckers et al 2017] DECKERS, Elke ; JONCKHEERE, Stijn ; VAN BELLE, Lucas ; CLAEYS, Claus ; DESMET, Wim: Hybrid Wave Based-Finite Element unit cell model to predict reflection, transmission and absorption coefficients of periodic material systems. In: *Proceedings of MEDYNA 2017: 2nd Euro-Mediterranean Conference on Structural Dynamics and vibroacoustics*, 2017
- [Deckers et al 2015] DECKERS, Elke ; JONCKHEERE, Stijn ; VANDEPITTE, Dirk ; DESMET, Wim: Modelling techniques for vibro-acoustic dynamics of poroelastic materials. In: *Archives of Computational Methods in Engineering* 22 (2015), Nr. 2, p. 183–236
- [Duhamel et al 2006] DUHAMEL, Denis ; MACE, Brian R. ; BRENNAN, Michael J.: Finite element analysis of the vibrations of waveguides and periodic structures. In: *Journal of Sound and Vibration* 294 (2006), Nr. 1-2, p. 205–220
- [Ehlers 1996] EHLERS, W.: Grundlegende Konzepte in der Theorie Poröser Medien. In: *Technische Mechanik* 16 16 (1996), Nr. 16, p. 63–76
- [Errico et al 2019] ERRICO, F. ; TUFANO, G. ; ROBIN, O. ; GUENFOUD, N. ; ICHCHOU, M. ; ATALLA, N.: Simulating the sound transmission loss of complex curved panels with attached noise control materials using periodic cell wavemodes. In: *Applied Acoustics* 156 (2019), p. 21–28
- [Fahy and Gardonio 2007] FAHY, Frank J. ; GARDONIO, Paolo: *Sound and structural vibration: radiation, transmission and response*. Elsevier, 2007
- [Fasold and Veres 2003] FASOLD, Wolfgang ; VERES, Eva: *Schallschutz und Raumakustik in der Praxis: Planungsbeispiele und konstruktive Lösungen*. Huss-Medien, Verlag Bauwesen, 2003
- [Fillunger 1913] FILLUNGER, Paul: Der Auftrieb von Talsperren. In: *Österreichische Wochenschrift für den öffentlichen Baudienst* 19 (1913), p. 532–570

- [Franck 2009] FRANCK, Andreas: *Finite-Elemente-Methoden, Lösungsalgorithmen und Werkzeuge für die akustische Simulationstechnik*, RWTH Aachen, Ph.D. thesis, 2009
- [Fuchs 2010] FUCHS, Helmut V.: *Schallabsorber und Schalldämpfer: Innovative akustische Konzepte und Bauteile mit praktischen Anwendungen in konkreten Beispielen*. Springer-Verlag, 2010
- [Groby et al 2011] GROBY, J.-P. ; DAZEL, O. ; DUCLOS, A. ; BOECKX, L. ; KELDERS, Luc: Enhancing the absorption coefficient of a backed rigid frame porous layer by embedding circular periodic inclusions. In: *The Journal of the Acoustical Society of America* 130 (2011), Nr. 6, p. 3771–3780
- [Groby et al 2014] GROBY, J.-P. ; LAGARRIGUE, C. ; BROUARD, B. ; DAZEL, Olivier ; TOURNAT, V. ; NENNIG, Benoit: Using simple shape three-dimensional rigid inclusions to enhance porous layer absorption. In: *The Journal of the Acoustical Society of America* 136 (2014), Nr. 3, p. 1139–1148
- [Groby et al 2008] GROBY, Jean-Philippe ; WIRGIN, Armand ; OGAM, Erick: Acoustic response of a periodic distribution of macroscopic inclusions within a rigid frame porous plate. In: *Waves in Random and Complex Media* 18 (2008), Nr. 3, p. 409–433
- [Hackenberg 2016] HACKENBERG, Manuela: *A Coupled Integral Transform Method-Finite Element Method Approach to Model the Soil-Structure-Interaction*, Technische Universität München, Ph.D. thesis, 2016
- [Harari et al 2000] HARARI, Isaac ; SLAVUTIN, Michael ; TURKEL, Eli: Analytical and numerical studies of a finite element PML for the Helmholtz equation. In: *Journal of Computational Acoustics* 8 (2000), Nr. 01, p. 121–137
- [Hörlin 2004] HÖRLIN, Nils-Erik: *Hierarchical finite element modelling of Biot's equations for vibro-acoustic modelling of layered poroelastic media*, KTH, Ph.D. thesis, 2004
- [Hurty 1960] HURTY, Walter C.: Vibrations of structural systems by component mode synthesis. In: *Journal of the Engineering Mechanics Division* 86 (1960), Nr. 4, p. 51–69
- [Johnson et al 1987] JOHNSON, David L. ; KOPLIK, Joel ; DASHEN, Roger: Theory of dynamic permeability and tortuosity in fluid-saturated porous media. In: *Journal of Fluid Mechanics* 176 (1987), p. 379–402
- [Johnson et al 1986] JOHNSON, David L. ; KOPLIK, Joel ; SCHWARTZ, Lawrence M.: New pore-size parameter characterizing transport in porous media. In: *Physical Review Letters* 57 (1986), Nr. 20, p. 2564
- [Jonckheere et al 2013] JONCKHEERE, Stijn ; DECKERS, Elke ; VAN GENECHTEN, Bert ; VANDEPITTE, Dirk ; DESMET, Wim: A direct hybrid Finite Element–Wave Based Method for the steady-state analysis of acoustic cavities with poro-elastic damping layers using the coupled Helmholtz–Biot equations. In: *Computer Methods in Applied Mechanics and Engineering* 263 (2013), p. 144–157

- [Kang and Bolton 1995] KANG, Yeon J. ; BOLTON, J. S.: Finite element modeling of isotropic elastic porous materials coupled with acoustical finite elements. In: *The Journal of the Acoustical Society of America* 98 (1995), Nr. 1, p. 635–643
- [Kidner et al 2006] KIDNER, M. R. F. ; FULLER, C. R. ; GARDNER, B.: Increase in transmission loss of single panels by addition of mass inclusions to a poro-elastic layer: Experimental investigation. In: *Journal of Sound and Vibration* 294 (2006), Nr. 3, p. 466–472
- [Lagarrigue et al 2013] LAGARRIGUE, C. ; GROBY, J.-P. ; TOURNAT, V. ; DAZEL, O. ; UMNova, O.: Absorption of sound by porous layers with embedded periodic arrays of resonant inclusions. In: *The Journal of the Acoustical Society of America* 134 (2013), Nr. 6, p. 4670–4680
- [Langley 1993] LANGLEY, R. S.: A note on the force boundary conditions for two-dimensional periodic structures with corner freedoms. In: *Journal of Sound and Vibration* 167 (1993), p. 377–381
- [Lee et al 2016] LEE, Joong S. ; DECKERS, Elke ; JONCKHEERE, Stijn ; DESMET, Wim ; KIM, Yoon Y.: A direct hybrid finite element–wave based modelling technique for efficient analysis of poroelastic materials in steady-state acoustic problems. In: *Computer Methods in Applied Mechanics and Engineering* 304 (2016), p. 55–80
- [Lee and Wright 2016] LEE, Sam H. ; WRIGHT, Oliver B.: Origin of negative density and modulus in acoustic metamaterials. In: *Physical Review B* 93 (2016), Nr. 2, p. 024302
- [Lerch et al 2009] LERCH, Reinhard ; SESSLER, Gerhard ; WOLF, Dietrich: *Technische Akustik: Grundlagen und Anwendungen*. Springer-Verlag, 2009
- [Lyon and DeJong 1995] LYON, Richard H. ; DEJONG, Richard G.: *Theory and application of statistical energy analysis*. Butterworth-Heinemann, 1995
- [Mace et al 2005] MACE, Brian R. ; DUHAMEL, Denis ; BRENNAN, Michael J. ; HINKE, Lars: Finite element prediction of wave motion in structural waveguides. In: *The Journal of the Acoustical Society of America* 117 (2005), Nr. 5, p. 2835–2843
- [Mace and Manconi 2008] MACE, Brian R. ; MANCONI, Elisabetta: Modelling wave propagation in two-dimensional structures using finite element analysis. In: *Journal of Sound and Vibration* 318 (2008), Nr. 4-5, p. 884–902
- [Magliacano et al 2020] MAGLIACANO, Dario ; OUISSE, Morvan ; KHELIF, Abdelkrim ; DE ROSA, Sergio ; FRANCO, Francesco ; ATALLA, Noureddine ; COLLET, Manuel: Computation of dispersion diagrams for periodic porous materials modeled as equivalent fluids. In: *Mechanical Systems and Signal Processing* 142 (2020), p. 106749
- [Mead 1973] MEAD, D. J.: A general theory of harmonic wave propagation in linear periodic systems with multiple coupling. In: *Journal of Sound and Vibration* 27 (1973), Nr. 2, p. 235–260
- [Mechel 2008] MECHEL, Fridolin P. (Editor.): *Formulas of Acoustics*. Springer-Verlag Berlin Heidelberg, 2008

- [Miksch et al 2019] MIKSCH, M. ; PEREZ RAMIREZ, J. D. ; MÜLLER, G.: Numerical computation of the spatial decaying wave characteristics for the design of locally resonant acoustic metamaterials. In: *Journal of Physics: Conference Series* 1264 (2019), p. 012015
- [Möser 2005] MÖSER, Michael: *Technische Akustik*. Volume 8. Springer, 2005
- [Müller and Möser 2004] MÜLLER, Gerhard ; MÖSER, Michael: *Taschenbuch der Technischen Akustik*. Springer, Berlin, Heidelberg, 2004
- [Nennig et al 2012] NENNIG, Benoit ; RENOU, Ygaël ; GROBY, Jean-Philippe ; AURÉGAN, Yves: A mode matching approach for modeling two dimensional porous grating with infinitely rigid or soft inclusions. In: *The Journal of the Acoustical Society of America* 131 (2012), Nr. 5, p. 3841–3852
- [Ochmann et al 2017] OCHMANN, Martin ; LIPPERT, Stephan ; ESTORFF, Otto v.: Numerische Methoden der Technischen Akustik. In: *Taschenbuch der Technischen Akustik*. Springer, 2017, p. 1–36
- [Orris and Petyt 1974] ORRIS, Ruth M. ; PETYT, M.: A finite element study of harmonic wave propagation in periodic structures. In: *Journal of Sound and Vibration* 33 (1974), Nr. 2, p. 223–236
- [Panneton 2007] PANNETON, Raymond: Comments on the limp frame equivalent fluid model for porous media. In: *The Journal of the Acoustical Society of America* 122 (2007), Nr. 6, p. EL217–EL222
- [Panneton and Atalla 1997] PANNETON, Raymond ; ATALLA, Nouredine: An efficient finite element scheme for solving the three-dimensional poroelasticity problem in acoustics. In: *The Journal of the Acoustical Society of America* 101 (1997), Nr. 6, p. 3287–3298
- [Paolini et al 2018] PAOLINI, Alexander ; WINTER, Christoph ; MÜLLER, Gerhard ; KOLLMANNBERGER, Stefan ; RANK, Ernst: Vergleich der h- und p-Version der FEM zur Prognose des Körperschalls in Massivholzkonstruktionen. In: *Fortschritte der Akustik, DAGA 2018*, 2018
- [Rumpler 2012] RUMPLER, Romain: *Efficient finite element approach for structural-acoustic applications including 3D modelling of sound absorbing porous materials*, Paris, CNAM, Ph.D. thesis, 2012
- [Rumpler et al 2012] RUMPLER, Romain ; DEÜ, Jean-François ; GÖRANSSON, Peter: A modal-based reduction method for sound absorbing porous materials in poro-acoustic finite element models. In: *The Journal of the Acoustical Society of America* 132 (2012), Nr. 5, p. 3162–3179
- [Rumpler et al 2013] RUMPLER, Romain ; GÖRANSSON, Peter ; DEÜ, Jean-François: A residue-based mode selection and sorting procedure for efficient poroelastic modeling in acoustic finite element applications. In: *The Journal of the Acoustical Society of America* 134 (2013), Nr. 6, p. 4730–4741
- [Schanz 2001] SCHANZ, Martin: *Wave propagation in viscoelastic and poroelastic continua: a boundary element approach*. Volume 2. Springer Science & Business Media, 2001

- [Schanz 2003] SCHANZ, Martin: On the equivalence of the linear Biot's theory and the linear theory of porous media. In: *16th ASCE Engineering Mechanics Conference*, 2003
- [Serra et al 2015] SERRA, Quentin ; ICHCHOU, M. ; DEÛ, J.-F.: Wave properties in poroelastic media using a Wave Finite Element Method. In: *Journal of Sound and Vibration* 335 (2015), p. 125–146
- [Sheng and Chan 2005] SHENG, Ping ; CHAN, Che T.: Classical wave localization and spectral gap materials. In: *Zeitschrift für Kristallographie-Crystalline Materials* 220 (2005), Nr. 9-10, p. 757–764
- [Shirron and Giddings 2006] SHIRRON, Joseph J. ; GIDDINGS, Thomas E.: A finite element model for acoustic scattering from objects near a fluid–fluid interface. In: *Computer Methods in Applied Mechanics and Engineering* 196 (2006), Nr. 1-3, p. 279–288
- [Späh and Lutz 2015] SPÄH, Moritz ; LUTZ, Weber: *Schall-Längsdämmung von Gipskarton-Ständerwänden*. Fraunhofer IRB Verlag, 2015
- [Spura 2019] SPURA, Christian: *Einführung in die Balkentheorie nach Timoshenko und Euler-Bernoulli*. Springer, 2019
- [Tanneau et al 2006] TANNEAU, O. ; CASIMIR, J. B. ; LAMARY, P.: Optimization of multilayered panels with poroelastic components for an acoustical transmission objective. In: *The Journal of the Acoustical Society of America* 120 (2006), Nr. 3, p. 1227–1238
- [von Terzaghi 1923] TERZAGHI, Karl von: Die Berechnung der Durchlässigkeitsziffer des Tones aus dem Verlauf der hydrodynamischen Spannungerscheinungen. In: *Sitzungsbericht der Akademie der Wissenschaften in Wien, mathematisch–naturwissenschaftlichen Klasse, Abteilung IIa* 132 (1923), p. 125–138
- [Van Belle et al 2020] VAN BELLE, Lucas et al: Fast metamaterial design optimization using reduced order unit cell modeling. In: *ISMA2020 International Conference on Noise and Vibration Engineering, September 07-09, 2020, Leuven, Belgium, 2020*
- [Waki et al 2009] WAKI, Y. ; MACE, B. R. ; BRENNAN, M. J.: Numerical issues concerning the wave and finite element method for free and forced vibrations of waveguides. In: *Journal of Sound and Vibration* 327 (2009), Nr. 1-2, p. 92–108
- [Weber et al 2019] WEBER(Mittermeier), F. ; SCHAUER, J. ; MIKSCH, M. ; MÜLLER, G.: Numerical investigation of the potential of tailored inclusions as noise reduction measures. In: *Journal of Physics: Conference Series* 1264 (2019), p. 012013
- [Weber et al 2020] WEBER, Franziska ; HICKS, Tom ; MIKSCH, Matthias ; RUMPLER, Romain ; MÜLLER, Gerhard: Numerical investigation of periodic metamaterials. In: *ISMA2020 International Conference on Noise and Vibration Engineering, September 07-09, 2020, Leuven, Belgium, 2020*
- [Weisser et al 2016] WEISSER, Thomas ; GROBY, Jean-Philippe ; DAZEL, Olivier ; GAULTIER, François ; DECKERS, Elke ; FUTATSUGI, Sideto ; MONTEIRO, Luciana: Acoustic behavior of a rigidly backed poroelastic layer with periodic resonant inclusions by a



- multiple scattering approach. In: *The Journal of the Acoustical Society of America* 139 (2016), Nr. 2, p. 617–629
- [Winter 2018] WINTER, Christoph: *Frequency Dependent Modeling for the Prediction of the Sound Transmission in Timber Constructions*, Technische Universität München, Ph.D. thesis, 2018
- [Wohlmuth 2000] WOHLMUTH, Barbara I.: A mortar finite element method using dual spaces for the Lagrange multiplier. In: *SIAM journal on numerical analysis* 38 (2000), Nr. 3, p. 989–1012
- [Yang 2018] YANG, Yi: *Vibroacoustic analysis of panels using a wave and finite element method*, University of Auckland, Ph.D. thesis, 2018
- [Yang et al 2017] YANG, Yi ; MACE, Brian R. ; KINGAN, Michael J.: Prediction of sound transmission through, and radiation from, panels using a wave and finite element method. In: *The Journal of the Acoustical Society of America* 141 (2017), Nr. 4, p. 2452–2460
- [Zhong and Williams 1995] ZHONG, W. X. ; WILLIAMS, F. W.: On the direct solution of wave propagation for repetitive structures. In: *Journal of Sound and Vibration* 181 (1995), Nr. 3, p. 485–501
- [Zhou et al 2015] ZHOU, C. W. ; LAINÉ, J. P. ; ICHCHOU, M. ; ZINE, A. M.: Wave finite element method based on reduced model for one-dimensional periodic structures. In: *International Journal of Applied Mechanics* 7 (2015), Nr. 02, p. 1550018
- [Zielinski 2007] ZIELINSKI, T. G.: Modelling of poroelastic layers with mass implants improving acoustic absorption. In: *Proceedings of the 19th International Congress on Acoustics*, 2007
- [Zienkiewicz et al 2005] ZIENKIEWICZ, O.C. ; TAYLOR, R.L. ; ZHU, J.Z.: *The Finite Element Method: Its Basis and Fundamentals*. Butterworth-Heinemann, 2005